Diss. ETH No. 28876

TRIPLET UNRAVELING: A STOCHASTIC ALGORITHM FOR LATTICE QUANTUM SYSTEMS

A thesis submitted to attain the degree of

Doctor of Sciences
(Dr. sc. ETH Zurich)

presented by

Romain Chessex
M. sc. in Physics, ETH Zurich
born on 01 September 1993

accepted on the recommendation of

Prof. Dr. Hans Christian Öttinger
Prof. Dr. Francesco Petruccione
Prof. Dr. Alexei Bazavov
Dr. Massimo Borrelli

2022

Front cover by: Amandine Ischer
Artistic representation of a controlled exploration
of the Hilbert space with triplet unraveling.

For you, who dream of never-ending winters.

"Who wants to climb a mountain starts at the bottom."
— Chinese proverb

Acknowledgements

This project would not have been possible without my advisor Hans Christian Öttinger, who trusted and supported me with his great guidance. Hans Christian, thank you for the liberty I was given in choosing the topic and direction of my work. I believe your precious advice and suggestions were essential. The many discussions we had on quantum physics and beyond pushed me to understand in a deeper and more intuitive way the insights of this work. Besides physics, I have broadened my knowledge in many fields such as statistics and computer science. More importantly, your idealistic approach of science gives me hope that new intuitive numerical tools can still be developed, especially for quantum physics.

I would like to recognize the invaluable assistance of Massimo Borrelli for his immense technical support and the huge amount of discussions we had. Massimo, your bulletproof morale, permanent good mood, and continuous flow of ideas for new project were very stimulating. You really helped me realize the versatility this approach and put it in a broader context. Thank you for the huge amount of time you invested in the detailed comments about this dissertation.

In addition, I wish to thank Francesco Petruccione and Alexei Bazavov who agreed to be members of my doctoral examination committee and took the time to review my research critically.

I would also like to thank my coworkers Alexander, Ioanna, Elia, Meisam, and all the others for the moments we shared during these years spent together. Although our different scientific backgrounds were not always exactly overlapping, it engendered nice refreshing discussions during lunch breaks, lectures, and teaching assignments. Many thanks to Martin for the IT support and coding tips, and to Patricia for helping me find my way through the administrative maze.

To my family, especially my parents, I am very grateful for your dedication to my education and for teaching me to never give up. Dad, you have always reminded me to stay true to myself. Mom, thank you for the curiosity you have passed on to me.

Finally, to Amandine, I thank you with all my heart for your love and sincerity. You have always believed in me and encouraged me to give the best of myself with your unconditional support.

Contents

Abstract

Numerical stochastic methods are celebrated for their ability to provide reliable solutions and accurate approximations of quantum problems. This success originates from the use of random sampling to handle the evaluation of multi-dimensional integrals, represent large matrices, or reproduce the intrinsic randomness of certain processes. However, the sign problem plagues most of these stochastic methods due to an attempt to replicate quantum features via classical algorithms. A near-cancellation of positive and negative contributions to the quantum averages engenders instabilities and prevents the numerical simulations from estimating values of physical observables.

In this thesis, we introduce a stochastic method to compute dynamical properties of multi-dimensional lattice quantum systems, which relies on an intuitive importance sampling procedure to partially overcome the sign problem. The theoretical foundations rely on dissipative quantum field theory, which is characterized by a Hamiltonian framework, together with a master equation approach and a natural regularization mechanism realized through quantum dissipation. Our stochastic trajectories are implemented by piecewise deterministic processes where continuous dynamics is interspersed with two-process quantum jumps, providing better control over the number of trajectories. The Hamiltonian formulation coupled with the quantum jump approach defines a natural framework for essential importance sampling procedures, whose interplay with efficient approximations reduces the severity of the sign problem as well as the number of independent trajectories needed to obtain convergent results.

Our algorithm is called *triplet unraveling* for its fundamental similarities with stochastic unraveling. We associate continuous dynamics and random jumps with a free-interacting splitting rather than the usual reversible-irreversible splitting. This trade enables the study of reversible quantum systems out of equilibrium and steady-state properties, which is realized through small variations of a more general algorithm. We present both variations with benchmarking models to test the ability of the algorithms to handle critical issues, including the sign problem via importance sampling. The introduction of the *deadweight* approximation provides access to the long-time dynamics of multi-dimensional reversible systems as opposed to most similar methods. We foresee promising applications in multi-dimensional reversible many-body physics with quantum quenches and critical phenomena. Independently, this technique also offers an alternative approach to lattice quantum chromodynamics, which has the benefit to compute quark dynamics on d- instead of a $(d+1)$-dimensional lattice.

Résumé

Les méthodes stochastiques numériques sont réputées pour leur aptitude à fournir des solutions fiables et des approximations fidèles de problèmes quantiques. Ce succès est dû à l'utilisation de l'échantillonnage aléatoire pour traiter l'évaluation d'intégrales multidimensionnelles, représenter des matrices complexes ou reproduire des processus aléatoires intrinsèques. Cependant, en raison d'une tentative de répliquer des caractéristiques quantiques via des algorithmes classiques, le problème du signe afflige la plupart de ces méthodes stochastiques. Une quasi-annulation des contributions positives et négatives aux espérances quantiques engendre des instabilités qui empêchent l'estimation d'observables physiques par des simulations numériques.

Dans cette thèse, nous proposons une méthode stochastique permettant de calculer les propriétés dynamiques de systèmes quantiques multidimensionnels sur réseau grâce à un échantillonnage préférentiel intuitif qui a pour effet de surmonter partiellement le problème du signe. Les fondements théoriques s'appuient sur la théorie dissipative des champs quantiques, qui est caractérisée par un cadre hamiltonien assorti d'une approche d'équation maîtresse et d'un mécanisme de régularisation naturel réalisé par dissipation quantique. Nos trajectoires stochastiques sont implémentées au moyen de processus déterministes par morceaux dont la dynamique continue est entrecoupée de sauts quantiques à deux processus, ce qui offre un meilleur contrôle du nombre de trajectoires. La formulation hamiltonienne associée à l'approche par sauts quantiques définit un cadre naturel pour les procédures d'échantillonnage préférentiel essentielles. De plus, l'action réciproque avec des approximations performantes réduit la complexité du problème du signe ainsi que le nombre de trajectoires indépendantes nécessaires pour obtenir des résultats convergents.

Notre technique est appelée dévoilement par triplets par sa similitude fondamentale avec le dévoilement stochastique. Elle associe la dynamique continue et les sauts aléatoires à une partition libre–interactive plutôt qu'à la partition habituelle réversible–irréversible. Ce changement permet d'étudier, grâce à des petites variations d'un algorithme plus général, les systèmes quantiques réversibles hors équilibre et les propriétés d'états stationnaires. Nous présentons ces deux variantes à l'aide de modèles de référence afin de tester la capacité des algorithmes à gérer des problématiques critiques, notamment le problème du signe via l'échantillonnage préférentiel. L'introduction d'une approximation, appelée poids mort, donne accès à la dynamique de systèmes réversibles multidimensionnels pour des temps longs, contrairement à la plupart des méthodes similaires. Nous anticipons des applications prometteuses en physique réversible multidimensionnelle à N corps en simulant des quenchs quantiques et des phénomènes critiques. Indépendamment, cette technique offre également une approche alternative à la chromodynamique quantique sur réseau, qui présente l'avantage de calculer la dynamique des quarks sur un réseau en d dimensions au lieu de $d + 1$.

1 Introduction

Computer simulations are extremely powerful tools allowing scientists to solve problems that are too complex to be solved analytically. The key to developing sophisticated new numerical methods is to construct efficient and versatile computer simulation techniques with innovative ideas to overcome common problems. This statement is particularly true for simulations of complex systems where the accuracy is limited by memory access or the raw number of operations performed per unit of time. The focus should be on methods where intuition can be used to massively reduce the computation effort with revolutionary and ingenious algorithmic ideas. Simulations of quantum systems are known to be a challenging topic, especially when dealing with large systems. The number of allowed configurations grows exponentially with increasing system size and makes it impossible to store all these configurations in a computer. A successful solution is to consider stochastic methods to represent and compute the properties of such quantum models. These numerical techniques denote a family of computational methods for calculating approximate numerical estimations using random processes. The general strategy is to simulate the quantum systems stochastically and average over multiple independent simulations. The intrinsic statistical noise provides an estimate of the error of the quantum averages and is computed via these independent simulations. This technique is intensively used for high-precision studies from low- to high-energy physics, notably, in condensed matter systems [1–4] and fundamental interactions between quarks [5–7].

A particularly useful approach to simulate those quantum systems stochastically is to formulate them on a lattice, as opposed to the space-time continuum. Lattice models were originally introduced in the context of condensed matter physics, where the atoms of a crystal naturally form a lattice. These discretized models are ideally studied by computational means due to the natural lattice representation in the computer data. Some models are exactly solvable, and thus, offer insight into the physics beyond what can be learned from perturbation theory. In condensed matter physics, more specifically in the field of strongly-correlated particles, many models exist, describing a large variety of physical effects. The most common models are the Ising model, its generalization the Heisenberg model [8], the more complex Bose- and Fermi-Hubbard models [9], and many variations of impurity models [10]. These lattice models together with diverse stochastic methods [11, 12] have provided invaluable insights into phase transitions, magnetization, and zero-temperature behavior of strongly-correlated many-body systems. Additionally, the recent introduction of real-time stochastic simulation techniques [13–17] revealed many dynamical phenomena, such as dynamics of quantum correlations, quenched many-body dynamics, and dynamical phase transitions. In high-energy physics, a particularly interesting yet

challenging topic concerns numerical methods for quantum chromodynamics (QCD) on a lattice [18]. Lattice QCD is a formulation of the interaction between quarks and gluons on discretized points of the space-time lattice, which provides an ideal nonperturbative framework to study quark confinement [19–21]. Because confinement has never been proven analytically, lattice simulations are crucial to explore the details of the confinement mechanism [5]. In practice, lattice QCD calculations stochastically produce samples of path integrals in Euclidean time, where sequences of field configurations are generated randomly. The quantities of interest are evaluated using the ensemble of generated configurations, whose statistical averages are computed. The accuracy of these computations is highly dependent on computational resources and accounts for a significant portion of the supercomputer-time consumed around the world [22–25]. The main limitation is dictated by the number of lattice points and through solving huge systems of linear equations encoding the quark-gluon interactions [26–28]. [1] On current typical supercomputers, it is the memory bandwidth needed to solve these linear systems that limits the size of the systems.

A prominent issue common to a vast majority of stochastic simulations in low- to high-energy physics is the sign problem, a numerical artifact that prevents simulations from evaluating quantum averages. Essentially, it produces instabilities in measurements that increase exponentially with simulation length and system size. It is due to the inability of a classical algorithm to reproduce quantum features of the system under study. Its origin is not clearly defined by a single quantum effect but it usually manifests itself as a divergent signal. The sign problem plagues many models and situations in computational physics [29, 30], for instance, in nuclear physics [31] or lattice QCD at low energies where the nonperturbative effects are important [32]. Other examples of sign problems occur in bosonic nonrelativistic systems [33], or in condensed matter physics [34, 35], in particular in the Hubbard model away from half-filling or the Heisenberg model on a triangular lattice. Thus, the main challenge for any new stochastic method is to construct an efficient scheme to circumvent, overcome, or at least weaken the sign problem during the time scales explored by the simulations.

As a natural setting for efficient numerical methods to overcome the sign problem, the theory of dissipative quantum fields [36–39] not only provides a substitute to lattice quantum chromodynamics but also a possible solution to the memory bottleneck. Dissipative quantum field theory (DQFT) was developed as an alternative effective description of fundamental particles and their interactions where dissipation introduces a natural regularization mechanism for ultraviolet divergences. The coupling with the environment acts as a regularization parameter for divergent ultraviolet contributions, where only the vanishing dissipation limit is interpreted as a physical result. Additionally, its formulation on the momentum lattice provides an infrared cutoff. The regularization parameters, namely the lattice spacing and the friction, are only auxiliary parameters providing convergent results, and the physically relevant results are provided by the vanishing limit. This dissipative method is nonperturbative in nature, which avoids the infamous problems of perturbation theory. It is based on a quantum master equation whose solution is a density matrix

[1] The linear systems that have to be solved originate from the differential Dirac operator. As in most partial differential equations solvers, the derivatives are replaced by finite difference methods. Hence, the Dirac operator corresponds to a huge sparse matrix, whose inversion is the most expensive part of the lattice quantum chromodynamics calculations. This inversion is performed using numerical methods involving many multiplications of the Dirac operator with vectors of the Hilbert space. The lattice calculations are essentially reduced to solving many systems of linear equations involving the Dirac matrix.

in a suitable second-quantization form. Its Hamiltonian approach implies that the particles dynamics is computed on a d-dimensional grid as opposed to $d+1$ in lattice QCD. Given the current lattice sizes [40, 41], it would roughly reduce the memory requirement by two orders of magnitudes. Albeit originally formulated in the context of high-energy physics, the simulation ideas for DQFT are completely general and can be applied to condensed matter systems as well. Hence, we also expect DQFT to reproduce the physics described by reversible strongly-correlated many-body models on the lattice.

In the context of stochastic simulations of open quantum systems, unraveling provides a numerical tool to solve quantum master equations, when the coupling to the environment is small. Stochastic unraveling consists in constructing piecewise deterministic processes whose realizations, or trajectories, experience continuous deterministic evolution interspersed with instantaneous random jumps. The statistical average over a large number of independent realizations of these stochastic processes reproduces the solution of a quantum master equation. Dissipative quantum field theory sets a natural framework for stochastic unraveling due to its coupling to a dissipative environment and its formulation in terms of a quantum master equation. Besides the common quantum master equation approach, the link between DQFT and unraveling lies in the fact that the weak coupling regime in which unraveling is valid corresponds to the limit required by the dissipative quantum fields to reproduce physical results.

From this combination, we develop a method called *triplet unraveling* to reproduce the solution of the quantum master equation for many-particles systems. To address the common difficulties mentioned earlier, we design a stochastic method that (i) weakens the sign problem, (ii) includes importance sampling to reduce the computational cost and allow for algorithmic improvements, and (iii) is suited for computational clusters by an efficient parallel implementation that optimizes the spatial and time computational efforts. Classical analogies to this quantum-jump approach would be molecular dynamics in the reversible case and Brownian dynamics for dissipative systems. The use of a preferred simulation basis reduces the diverging fluctuations. The sign problem can be further diminished by an intuitive importance sampling procedure, whose introduction is natural in the Hamiltonian framework combined with a stochastic jump approach. Additionally, the expressions of the time-evolution operators are formulated in the Laplace domain, which greatly simplifies the implementation of the stochastic jumps and enables the use of further approximations to reduce the statistical noise. From an implementation point of view, our method is highly parallelizable for computational clusters, that is a parallel execution on independent logical processes with a minimal number of synchronization between these processes. In the triplet unraveling algorithm, the data is structured in such a way that the communication between processes is optimized, and the interacting effects are implemented by this minimal information exchange.

The main practical challenges in developing this new method are the efficiency of the procedure to overcome the sign problem, precise control over the trajectories in the Hilbert space, and the effect of importance sampling. To address these main difficulties, we consider prominent models in condensed matter without dissipation. Unlike most investigations that are usually restricted to one-dimensional systems or short times, a feature of our algorithm enables access to long-time properties of multi-dimensional reversible quantum systems, which has been so far realized only by a handful of numerical methods. Although real-time simulations are typically affected by both a severe sign problem and poor control of the exploration of the Hilbert

space, the use of importance sampling and specific approximations provide a feasible way to limit the impact of these issues. These simulations are possible with the introduction of the so-called *deadweight approximation* that limits the exploration of the Hilbert space to statistically important quantum state-jumps only. An additional feature that highlights the versatility of the formulation in the Laplace domain is the use of the evolution operators to compute also ground states of unknown Hamiltonians. The ground-state properties are calculated via a fixed point equation in the Laplace domain, which provides an iterative method to obtain an estimation of the ground state. As we will see, these ground states also serve as initial conditions for high-energy physics simulations. This work provides a proof-of-feasibility for calculations of quantum systems using a quantum type of molecular dynamics method, triplet unraveling. Besides exploring the capabilities of this novel approach for multidimensional reversible quantum systems and ground states of unknown Hamiltonians, we use this study as a starting point for exciting future applications in lattice quantum chromodynamics.

This work is structured as follows. Chapter 2 introduces the concepts of dissipative quantum field theory and the key ingredients behind its development. Independently, this chapter also describes stochastic unraveling and indicates how it can be used in the framework of dissipative quantum field theory. An alternative splitting of the deterministic and stochastic contributions is reviewed and forms the basis for the methods described in the following chapters for ground-state calculations and reversible dynamics. Chapter 3 concentrates on the link between unraveling and dissipative quantum field theory to develop our fundamental numerical framework using the alternate splitting introduced earlier and the properties of the Laplace domain. Chapter 4 describes an algorithm based on this framework to compute ground states of unknown Hamiltonians, and provides insights into the algorithmic details. Chapter 5 introduces a real-time algorithm to compute reversible dynamics of quantum many-body systems. It is again based on a special case of the general technique exposed in Chapter 3. This chapter should be seen as (i) the introduction of an efficient method to compute dynamical properties of reversible multidimensional quantum systems, and (ii) a milestone for the possible future applications in quantum chromodynamics. Chapter 6 concentrates on the future work and development of the method by discussing the efficiency of the technique for reversible dynamics and presenting the major challenges in fundamental particle simulations.

2 Stochastic unraveling of quantum master equations

The algorithm presented in this dissertation combines the theory of dissipative quantum fields [36] with the numerical tools of stochastic unraveling [42]. As mentioned in the introduction, we want to use the framework of DQFT to construct a stochastic unraveling that allows us to simulate (i) steady-state, (ii) reversible, and potentially (iii) high-energy properties of quantum systems using small variations of a common general method. Because of similarities between the formulation of DQFT and open quantum systems [43], unraveling is a natural approach to simulations of fundamental particles coupled to a dissipative environment.

This chapter is separated into three sections. First, we briefly introduce the necessary mathematical and statistical notation for simulating quantum systems using a stochastic approach. Since our numerical approach consists of a quantum field theoretical background combined with open quantum systems and stochastic methods, we want to have proper definitions of the basic concepts. To finish with this introductory part, we give an intuitive overview of the sign problem [44] and the related issues due to its permanent involvement in stochastic simulations. In a second stage, we introduce a thermodynamic approach to open quantum systems from which the development of DQFT originates. This serves as a starting point for a concise derivation of the fundamental equations on which our numerical scheme relies. In the last section, we describe in details how to unravel a master equation and generalize the standard single process unraveling to two-process unraveling in order to compute nonsymmetrical correlation functions. By the end of the chapter, we will have all the necessary theoretical and numerical tools to build our main algorithm.

2.1 Stochastic numerical methods

Stochastic numerical methods have been used with great success to calculate properties of quantum systems ranging from condensed matter [2, 45], to quantum chemistry [3, 46], to lattice QCD [5–7]. A stochastic method is not a specific technique but a general strategy for solving problems that are too complex for an analytical solution to be found. These methods define a stochastic procedure that is applied iteratively to construct a large number of samples that reproduce physical observations on average. Intuitively, stochastic numerical methods use properties of random numbers to represent the solutions of complex problems through statistical averages.

2.1.1 Stochastic processes

Stochastic techniques are often constructed to reproduce specific *stochastic processes*. A stochastic process is a family of random variables $\{X(t),\ t \in \mathcal{T}\}$, where the set

$\mathcal{T}$ is interpreted as time axis. For discrete-time processes, it holds $\mathcal{T} = \mathbb{N}$ and for continuous time, $\mathcal{T} = [t_0, t_{\max}]$. To lighten the notation throughout this work, we adopt the convention $X(t) = X_t$ for time-dependent variables. The ensemble of values $\{x_t,\ t \in \mathcal{T}\}$, called a *trajectory*, denotes a single realization x_t of a process X_t and represents one possible evolution of this process. The *mean* of a process X_t with distribution function $P(X_t)$ is defined as

$$\mathbb{E}[X_t] = \sum_{x_t} x_t P(X_t = x_t), \tag{2.1}$$

where the sum $\sum_{x_t}$ denotes the sum over the set of possible values of the random variable X_t at t fixed. Accordingly, the *variance* is defined as

$$\mathrm{Var}[X_t] = \mathbb{E}[(X_t - \mathbb{E}[X_t])^2]. \tag{2.2}$$

In this work, we consider a special type of stochastic process called *piecewise deterministic process*. The evolution of the piecewise deterministic process combines random events, together with deterministic evolution. The deterministic part, which is dictated by the solution of some differential equation is interrupted by instantaneous random jumps. With a slight abuse of notation, let us denote the piecewise deterministic process with $\{X_t, t \in \mathcal{T}\}$. The time evolution is defined through specifying the following characteristics.

1. *The deterministic dynamics* is dictated by the solution of the general differential equation
$$\frac{dx_t}{dt} = \mathcal{G}(x_t), \tag{2.3}$$
where in this work, we assume the function $\mathcal{G}(x)$ to be linear in x_t. The solution leads to a deterministic evolution between two random events.

2. *The event rate.* Events occur instantaneously at rate $r(x_t)$ in a Poisson-like fashion. We assume that the rate depends only on the current state of the process.

3. *The transition distribution at events.* At each event, the state of the process changes according to some transition rules. If at time t an event occurs, we denote with x_{t_-} the state just prior to the event. After the event the state will be taken from a transition distribution $P_{\mathrm{tran}}(X|X_t = x_{t_-})$.

2.1.2 ESTIMATORS

For a general stochastic process X_t, a numerical stochastic method is an algorithm that generates a set of N_R independent trajectories $x_t^{(n)}$, with $n = 1, 2, \ldots, N_R$. Generally, we wish to estimate the expectation value $\mathbb{E}[f(X_t)] = \ell$, where $f(X_t)$ is a function that may depend explicitly on time. We construct an estimator for the expectation value from independent trajectories as

$$\ell \approx \bar{f}_t = \frac{1}{N_R} \sum_{n=1}^{N_R} f(x_t^{(n)}), \tag{2.4}$$

where the estimator is exact for $N_R \to \infty$. Assuming a finite variance σ^2 and N_R large, we define an estimator for the variance

$$\mathrm{Var}[f(X_t)] \approx V^2 = \frac{1}{N_R - 1} \sum_{n=1}^{N_R} \left(f(x_t^{(n)}) - \bar{f}_t \right)^2, \tag{2.5}$$

which is also exact for $N_R \to \infty$. The *standard error* is defined as $V/\sqrt{N_R}$.

One of the most useful variance reduction methods is *importance sampling*. Instead of generating realizations according to the probability density function $P(X_t)$ to estimate $\mathbb{E}[f(X_t)]$, it might be more efficient to generate independent realizations $y_t^{(n)}$ from a density probability $Q(Y_t)$, with the original expectation value being recovered as

$$\ell = \sum_{y_t} f(y_t) \frac{P(Y_t = y_t)}{Q(Y_t = y_t)} Q(Y_t = y_t). \tag{2.6}$$

The estimator of the expectation value hence yields

$$\bar{f}_t = \frac{1}{N_R} \sum_{n=1}^{N_R} f(y_t^{(n)}) \frac{P(Y_t = y_t^{(n)})}{Q(Y_t = y_t^{(n)})}. \tag{2.7}$$

The main difficulty lies in choosing the distribution $Q(\cdot)$, since a poor choice may seriously affect the accuracy of the estimate. The theoretical optimal choice for Q is the one minimizing the variance, that is $Q^*(\cdot) = f(\cdot)P(\cdot)/\ell$. This optimal probability density function is generally very challenging to obtain *a priori* because the expectation value ℓ is unknown. However, a deeper understanding of the underlying stochastic process may provide new ideas to approximate the distribution $Q(\cdot)$, possibly leading to a drastic reduction of the variance.

2.1.3 STOCHASTIC METHODS FOR QUANTUM SYSTEMS

Quantum systems are generally described by state vectors in a complex Hilbert space $\mathcal{H}$. Assuming a system of many identical particles, let us label the number of particles in state $\nu = 1, 2, \dots$ with n_ν, and define the state vector of the whole system with the braket notation

$$|n_1, n_2, \dots\rangle. \tag{2.8}$$

The vacuum, or zero vector, is denoted by $|0\rangle$ and represents the absence of particles. For bosons, n_ν can take any positive value whereas for fermions either 0 or 1. To describe the time evolution of these state vectors, we need to specify a basis. We introduce the *Fock space* as the complex vector space formed by any linear combination of vectors of the form of (2.8), which are called Fock states. We associated the standard inner product

$$\langle n_1, n_2, \dots | n_1', n_2', \dots \rangle = \prod_{\nu=1}^{\infty} \delta_{n_\nu, n_\nu'}, \tag{2.9}$$

with this basis in the Dirac bra-ket notation. We also define the creation and annihilation operators and their representation in the Fock basis. For bosons, the creation operator $a_\nu^\dagger$ increases the number of particles in state ν by one, that is

$$a_\nu^\dagger |n_1, \dots, n_\nu, \dots\rangle = \sqrt{n_\nu + 1} |n_1, \dots, n_\nu + 1, \dots\rangle. \tag{2.10}$$

The annihilation operator a_ν lowers the number of particles by one or set it to 0 following the rule

$$a_\nu|n_1,\dots,n_\nu+1,\dots\rangle = \sqrt{n_\nu}|n_1,\dots,n_\nu,\dots\rangle. \tag{2.11}$$

These operators fulfill the usual bosonic commutation algebra

$$[a_\nu, a_\mu^\dagger] = \delta_{\nu,\mu}, \tag{2.12}$$

where all other combinations of operators vanish. For the fermions, due to the Pauli principle, the creation $b_\nu^\dagger$ and annihilation b_ν operators anticommute

$$\{b_\nu, b_\mu^\dagger\} = \delta_{\nu,\mu}, \qquad \{b_\nu, b_\mu\} = \{b_\nu^\dagger, b_\mu^\dagger\} = 0, \tag{2.13}$$

and they act on fermionic Fock states as follows,

$$b_\nu^\dagger|n_1,\dots,n_\nu,\dots\rangle = \delta_{n_\nu,0}(-1)^{s_\nu}|n_1,\dots,n_\nu+1,\dots\rangle, \tag{2.14}$$
$$b_\nu|n_1,\dots,n_\nu,\dots\rangle = \delta_{n_\nu,1}(-1)^{s_\nu}|n_1,\dots,n_\nu-1,\dots\rangle, \tag{2.15}$$

with $s_\nu = n_1 + n_2 + \cdots + n_{\nu-1}$.

What differentiates a classical stochastic method from a quantum one is the effort that must be provided to formulate a suitable stochastic algorithm representing physical quantum processes. The challenge in conceiving these algorithms is to reproduce quantum features such as noncommutativity of observables or quantum particle statistics (fermions and bosons) via classical processes. We express with $|\psi_t\rangle \in \mathcal{H}$ a general state vector in the Hilbert whose dynamics is entirely determined by the Hamiltonian H. We denote vector-valued quantum stochastic processes $|\Psi_t\rangle$ with upper case Greek letters and realizations with lower case letters $|\psi_t^{(n)}\rangle$.

Since a quantum system of dimension d can be mapped to a classical system of dimension $d+1$, classical stochastic methods are used to estimate properties of quantum systems. Hence, the quantum observables are computed by multi-dimensional integrals that involve classical weights, Boltzmann factors (see App. A.1 for more details). However, there exist systems for which the sign of these statistical weights is negative. In practical simulations, the contribution from two weights of opposite signs may nearly cancel due to numerical reasons and fluctuate between positive and negative values. These systems are said to suffer from a *sign problem* when the severity of the fluctuations grows with the size of the system and plagues the stochastic evaluation of the integrals with an exponentially increasing cost of the sampling. The sign problem may naturally occur in bosonic systems or spin Hamiltonians but is particularly severe for fermionic models as the anticommutation rules force a sign change for particle exchanges. Appendix A.1 illustrates how a diverging signal is equivalent to the presence of sign problem.

It has been shown that a generic solution is nondeterministic polynomial (NP) hard [47]. However, the severity of the sign problem strongly depends on the basis and the algorithm. Obviously, there would be no sign problem if we were able to diagonalize the Hamiltonian and estimate the mean of an observable O with the eigenbasis $\{|E_i\rangle\}_i$,

$$\langle O\rangle = \frac{\sum_i \langle E_i|O|E_i\rangle e^{-\beta E_i}}{\sum_i e^{-\beta E_i}}. \tag{2.16}$$

Unfortunately, it is nearly impossible to compute the eigenstates of any system in the first place. However, the existence of the sign problem does not automatically rule out

the possibility of simulating quantum systems stochastically as there exist strategies to cope with it. In some basis, the sign problem is mild enough for the desired properties to be computed. In others, the exponential increase in computational cost needed to overcome the sign problem can be slowed down until the observables are computed. In addition to the basis, there are algorithmic features that reduce significantly sign fluctuations. The approach described in this work uses a discrete simulation basis with an efficient cancellation of statistical weights and includes further approximations to reduce the severity of fluctuations, resulting in delaying the appearance of divergences. Moreover, the use of importance sampling massively reduces the number of independent trajectories involved in the evaluation of observables.

For the real-time evolution of a quantum system, as opposed to imaginary-time evolution $t \mapsto \beta \equiv it$, the weights in a stochastic simulation become complex due to the form of the time-evolution operator, e^{-iHt}, and the corresponding Boltzmann factors acquire a complex phase. When statistical weights are complex, fast oscillating phases appear due to the noncancellation effect described above. The difficulty to suppress this complex phase increases exponentially with time and eventually leads to numerical instabilities in the estimation of observables. We refer to the increasing cost of sampling for complex weights as the *dynamical sign problem.*

2.2 Dissipative quantum field theory

The thermodynamic quantum master equation developed in [39] characterizes the dynamics of dissipative quantum field theory. Quantum master equations are first-order differential equations describing the time evolution of a density matrix representing the statistical state of a quantum system. We start by making some general remarks about open quantum systems and introduce the quantum master equations describing these systems' dynamics. Then, we follow the structure of [36] to present the main theoretical concepts of dissipative quantum field theory. From the general thermodynamic master equation, we derive a linear quantum master equation approximating the dynamics and compute an expression for evolution superoperators. Finally, we introduce a very useful approximation to further simplify our linear quantum master equation to a more tractable version.

2.2.1 Open quantum systems

The theory of open quantum systems describes quantum mechanical systems coupled to an external environment [43, 48]. The interactions between the system and the environment depend on the microscopic details of the model and they typically introduce decoherence and/or dissipation in the system's reduced density matrix. In order to ensure irreversible behavior, it is necessary that the environment contains an infinite number of degrees of freedom. In practice, the exact treatment of such systems is unfeasible due to the complexity of resolving the time evolution of the environment. Hence, the standard strategy is to focus on the evolution of the system's reduced density matrix and to model the details of the interactions between the system and the environment as an averaged effect, while assuming that the state of the reservoir does not change significantly. The lack of memory of the environment and a weak coupling between the system and the environment are frequently employed assumptions. They lead to more tractable equations describing the dynamics in the form of quantum master equations for the reduced density matrix.

Following this general strategy, we describe the state of a quantum system at time t coupled to an environment in terms of its reduced density matrix ρ_t. In this

work, we are only interested in Markovian systems, i.e. dynamical systems where the evolution from time t to $t+\delta t$ depends only on the state of the system at time t. In these systems, the weak coupling regime allows us to write a linear equation for the dynamics of the system, the *Lindblad equation*,

$$\frac{d\rho_t}{dt} = -i[H,\rho_t] + \sum_\alpha \gamma_\alpha \left(L_\alpha \rho_t L_\alpha^\dagger - \frac{1}{2}\{L_\alpha^\dagger L_\alpha, \rho_t\} \right), \tag{2.17}$$

where H is the Hamiltonian of the system, L_α, $L_\alpha^\dagger$ are the Lindblad operators modeling transitions among the system's energy eigenstates induced by the reservoir, and γ_α are the decay rates associated to such transitions. These rates depend upon certain details of the environment. The reversible dynamics is described by the commutator between the Hamiltonian and the density matrix whereas the irreversible part is modeled by the second term. The validity of this equation depends on the separation between the different time scales of the model. In order to neglect the memory effects of the environment, one must assume a clear difference between the typical correlation time of the environment fluctuations and the relaxation time of the system. Moreover, as mentioned above, it is necessary to assume a weak coupling in order to suppress correlations between the system and the environment.

The Lindblad master equation is widely used and known to describe open quantum systems in the weak coupling regime accurately. Yet, the approximations and assumptions made in its derivation [1, 45] indicate that there are quantum systems needing to be described by a more complete quantum master equation. In particular, the linearity of the Lindblad equation is usually motivated by practical arguments because of the difficulty to solve a nonlinear quantum master equation but not by strong physical and thermodynamics motivations. In this work, we consider a different quantum master equation whose structure is based on thermodynamics arguments

$$\frac{d\rho_t}{dt} = -i[H,\rho_t] - \sum_\alpha \int_0^1 f_\alpha(u) \left([Q_\alpha, \rho_t^{1-u}[Q_\alpha^\dagger, \mu_t]\rho_t^u] + [Q_\alpha^\dagger, \rho_t^u[Q_\alpha, \mu_t]\rho_t^{1-u}] \right) du, \tag{2.18}$$

where the operators Q_α represent the coupling of the system to the environment and the $f_\alpha(u)$ are real non-negative rate factors that have to be chosen *a priori* very carefully. This master equation was first postulated in [39] to account for a separate evolution of reversible and irreversible effects, where the authors showed that under specific assumptions, a Lindblad-type master equation can be derived from the general Eq. (2.18). The reversible dynamics is generated by the Hamiltonian of the system H via the standard commutator. Conversely, the double commutators inside the integral account for the irreversible effects via the free energy contribution $\mu_t = H + k_B T \ln \rho_t$. A classical analogy for this equation would be the Fokker–Planck equation in which the diffusion terms associated with second-order derivatives are represented by the double commutators. The thermodynamic arguments used to postulate this equation as well as its geometrical structure ensure that the steady state always converges to the correct solution. The integral over du accounts for the correct entropy production and proper equilibrium state. The irreversible term is also of Markovian-type because the geometrical structure of this equation is inspired by classical nonequilibrium thermodynamics [49] for which memory effects are not taken into account.

2.2.2 LINEAR QUANTUM MASTER EQUATION

To describe the dynamics of particles in contact with an external environment, DQFT follows the general approach of open quantum systems by considering master equations. Here, we discuss how to obtain a tractable linear quantum master equation in the case of a ϕ^4 theory. Note that the same reasoning can be followed for more elaborate interaction models. It is preferable to use a discrete and finite set of momentum states to weaken the sign problem and to have an efficient weight cancellation. Hence, we discretize the momenta into a d-dimensional lattice as

$$K^d = \{\boldsymbol{k} = (z_1, \dots, z_d)\Delta k \text{ such that } z_i \in \mathbb{Z}, |z_i| \leq z_{\max}\ \forall i\}\,, \tag{2.19}$$

where Δk is the lattice spacing, and $z_{\max}\Delta k$ is a momentum cutoff. Eventually, we are interested in the limits $z_{\max} \to \infty$, $\Delta k \to 0$, which correspond to an infinitely large and dense lattice. As we saw earlier, the sign problem is base-dependent and because we are using the Fock basis rather than the eigenbasis, we should expect instabilities. However, the number of quantum states is finite due to the finite momentum lattice, hence we can hope for an efficient cancellation of weights to weaken the sign problem. As we will see, the finite set of basis vectors is sufficient to overcome the sign problem only with an additional control mechanism for the exploration of the Hilbert space.

To be complete, we still need to specify the Hamiltonian H. In the Fock basis, independently of the model, the Hamiltonian can be separated in the following form

$$H = H^{\text{free}} + H^{\text{coll}}, \tag{2.20}$$

where the free part corresponds to the kinetic contribution. In a ϕ^4-type of theory with particle mass m, the free Hamiltonian is

$$H^{\text{free}} = \sum_{\boldsymbol{k}\in K^d} \epsilon_k a^\dagger_{\boldsymbol{k}} a_{\boldsymbol{k}}, \tag{2.21}$$

where $\epsilon_k = \sqrt{m^2 + k^2}$. According to our splitting of the Hamiltonian, we would also have to specify the interactions between the particles, which are contained in the collision Hamiltonian. However, for the purpose of introducing the general concepts of DQFT and its connection to stochastic unraveling, we do not need an analytical form of the collision Hamiltonian. For interested readers, the collision Hamiltonian is given in App. C.1 in the case of the ϕ^4 theory. The quantum electrodynamics (QED) version in one spatial dimension is given in App. C.3. We encourage the reader to inspect Chaps. 1 and 3 of [36] for the construction of these Hamiltonians.

The general thermodynamic master equation (2.18) serves as a starting point, where the coupling operators Q_α are chosen as annihilation operators $a_{\boldsymbol{k}}$ so that the control over high energy contributions has the wanted effect. Section 3.2.6 of [36] gives examples of similar coupling operators for quantum electrodynamics. The rate factors are chosen to be

$$f_\alpha(u) = \beta\gamma_k e^{-u\beta\omega_k}, \tag{2.22}$$

where γ_k is the decay rate that increases with higher momenta. In analogy with our general thermodynamics approach, this choice is motivated by a Boltzmann-factor type of detailed balance with a heat bath. The exponential factor is chosen such that the master equation is linear for the free theory, in absence of collisions. For the concrete form of the decay rate, we have to realize that a commutator corresponds in real space to a double derivative associated with a diffusion process. For instance, the double derivative of the Schrödinger equation in position space corresponds to

a commutator in the von Neumann equation. Hence, each commutator should be associated with at least a k^2 contribution to the decay rate, and we propose the following expression

$$\gamma_k = \gamma_0 + \gamma k^4, \tag{2.23}$$

where γ_0 should be small since we are interested in the limit of small dissipation. One can show that within perturbation theory, this choice provides sufficient regularization for the propagator in 3 spatial dimensions to be convergent. The γ_0 is set to a nonzero value because the contributions from $k = 0$ might still need regularization.

A linearization of Eq. (2.18) around the equilibrium in the limit of zero-temperature yields for the deviation from equilibrium,

$$\Delta\rho_t = \rho_t - \rho_{\text{eq}}, \tag{2.24}$$

the following linearized quantum master equation

$$\begin{aligned}\frac{d}{dt}\Delta\rho_t = &- i[H, \Delta\rho_t] + \sum_{\boldsymbol{k}\in K^d} \gamma_k \left(2a_{\boldsymbol{k}}\Delta\rho_t a_{\boldsymbol{k}}^\dagger - \{a_{\boldsymbol{k}}^\dagger a_{\boldsymbol{k}}, \Delta\rho_t\}\right) \\ &- \sum_{\boldsymbol{k}\in K^d} \frac{\gamma_k}{\omega_k} \left(\left[a_{\boldsymbol{k}}, \Delta\rho_t [a_{\boldsymbol{k}}^\dagger, H^{\text{coll}}]\right] + \left[a_{\boldsymbol{k}}^\dagger, [a_{\boldsymbol{k}}, H^{\text{coll}}]\Delta\rho_t\right]\right).\end{aligned} \tag{2.25}$$

The benefit of this master equation as opposed to a master equation for the density matrix ρ_t is for practical reasons. Its solution for large times is guaranteed to be the equilibrium state ρ_{eq}. Additionally, fast convergence to the solution with a perturbative expansion is to be expected in the case of a weak interaction. As for the full thermodynamics quantum master equation, the trace conserving properties are preserved but however, the dynamics is computed for the traceless $\Delta\rho_t$. Because it is part of the initial condition, the equilibrium state ρ_{eq} has to be computed with an independent method. This will be the main goal of Chap. 4.

2.2.3 Evolution operator

Given a general linear master equation of the type

$$\frac{d}{dt}\rho_t = \mathcal{L}\rho_t, \tag{2.26}$$

its solution is given by

$$\rho_t = e^{\mathcal{L}t}\rho_0 \equiv \mathcal{E}_t\rho_0, \tag{2.27}$$

for some initial density matrix ρ_0. To solve the master equation (2.25), we want to construct an expansion of the superoperator $\mathcal{E}_t$. For that purpose, we separate the linear generator $\mathcal{L}$ into a free and a collision part, according to

$$\mathcal{L}^{\text{free}}\rho = -i[H^{\text{free}}, \rho] + \sum_{\boldsymbol{k}\in K^d} \gamma_k \left(2a_{\boldsymbol{k}}\rho a_{\boldsymbol{k}}^\dagger - \{a_{\boldsymbol{k}}^\dagger a_{\boldsymbol{k}}, \rho\}\right), \tag{2.28}$$

$$\mathcal{L}^{\text{coll}}\rho = -i[H^{\text{coll}}, \rho] - \sum_{\boldsymbol{k}\in K^d} \frac{\gamma_k}{\omega_k} \left([a_{\boldsymbol{k}}, \rho[a_{\boldsymbol{k}}^\dagger, H^{\text{coll}}]] + [a_{\boldsymbol{k}}^\dagger, [a_{\boldsymbol{k}}, H^{\text{coll}}]\rho]\right). \tag{2.29}$$

Inspired by the derivation of a piecewise deterministic process in [50], we start from the expression

$$\mathcal{E}_t = \mathcal{E}_t^{\text{free}} e^{-rt} - \left[\mathcal{E}_{t-t'}\mathcal{E}_{t'}^{\text{free}} e^{-rt'}\right]_0^t, \tag{2.30}$$

where we introduced a rate parameter r. We can reformulate this expression using $\frac{d}{dt}\mathcal{E}_t = \mathcal{L}\mathcal{E}_t$ (see App. A.2 for more details),

$$\mathcal{E}_t = \mathcal{E}_t^{\text{free}} e^{-rt} + \int_0^t dt' \mathcal{E}_{t-t'} \left(1 + \frac{\mathcal{L}^{\text{coll}}}{r}\right) \mathcal{E}_{t'}^{\text{free}} r e^{-rt'}. \tag{2.31}$$

The exponential term in the integral can be identified with an exponential time-step distribution with mean $1/r$

$$P_r(t) = re^{-rt}. \tag{2.32}$$

From this identification, we can interpret the above formula in a stochastic fashion. The collisions, denoted by the term in brackets, occur stochastically at random time-steps t' taken from the probability distribution (2.32). Each collision is preceded by a free continuous evolution. This procedure is repeated until the sum of the random time-steps is larger than t. In practice, this scheme is not optimal because we have to synchronize the sampling trajectories in order to perform measurements. These measurements have to be estimated by configurations at a fixed time t, where the time-steps are randomly chosen for each trajectory. It implies that the trajectories with large random time-steps have to wait until the slower ones reach the synchronization barrier. Hence, the evolution operator for a time $t = N_t \Delta t$ has to be split into small time-steps Δt using the Trotter formula $\mathcal{E}_t \approx \prod_{i=1}^{N_t} \mathcal{E}_{\Delta t}$. Small time-steps Δt are necessary to avoid too large deviations. For computational reasons, we want to have on average a single random time-step per application of $\mathcal{E}_{\Delta t}$, which implies $\Delta t \sim 1/r$. This choice indicates that r should be chosen large which makes the scheme inefficient for small interactions, where we would generally expect convergence with only a few time-steps. Another issue with the expression (2.31) is the nested application of the superoperator $\mathcal{E}_t$. One could further develop this equation by inserting this expression into $\mathcal{E}_{t'-t}$ which would eventually lead to a sum of convoluted terms (see Sec. 1.2.7.1 of [36]).

Alternately, we introduce the *Laplace transform* as a way to solve both of the issues mentioned above. We recognize that the exponential term in Eq. (2.31) that samples time-steps between collisions is natural in the Laplace domain, where all the jumps occur at a fixed rate r. Furthermore, the convolutions in the time domain are simple multiplications in the Laplace domain. Hence, we consider the Laplace transform of the evolution operator (2.31) defined as

$$\mathcal{R}_s \rho = \int_0^\infty dt\ e^{-st} \mathcal{E}_t \rho. \tag{2.33}$$

With the appropriate substitution, we get from (2.31) (see App. A.2 for details)

$$\mathcal{R}_s = \mathcal{R}_{s+r}^{\text{free}} + \mathcal{R}_s (r + \mathcal{L}^{\text{coll}}) \mathcal{R}_{s+r}^{\text{free}}. \tag{2.34}$$

Using the formal expansion for the inverse operator

$$\left[1 - (r + \mathcal{L}^{\text{coll}}) \mathcal{R}_{s+r}^{\text{free}}\right]^{-1}, \tag{2.35}$$

we obtain our final expression for the evolution superoperator in the Laplace domain,

$$\mathcal{R}_s = \sum_{m=0}^{\infty} r^m \left[\mathcal{R}_{s+r}^{\text{free}} \left(1 + \frac{\mathcal{L}^{\text{coll}}}{r}\right)\right]^m \mathcal{R}_{s+r}^{\text{free}}. \tag{2.36}$$

We refer to Eq. (2.36) as the *magical formula* because it unifies a perturbative expansion and a numerical scheme in a single equation. If $r = 0$, the perturbative expansion is recovered, because the m^{th} term in the sum represents the corresponding order in perturbation theory. Conversely, if $r > 0$, the sum can be interpreted as the time-evolution operator of a numerical integration scheme with time-step $1/r$. Hence, truncating the magical formula at some term $m = M_{\text{trunc}}$ sets a natural time limit for the numerical integration, which is $t_{\max} \sim 1/s_{\min} \sim \frac{M_{\text{trunc}}}{r}$. Even though the expression for the magical formula resembles perturbation theory for $r > 0$, we insist on the fact that it is nonperturbative in nature, in the sense that the perturbative expansions are recovered for the specific case $r = 0$ only. Because we mix the contributions from the whole time range, each summand in the magical formula should be understood as a rearrangement of an infinite number of perturbative terms. Conversely, perturbation theory is interpreted as an integration numerical scheme with infinitely large time-steps.

The Laplace transform constructs a superposition with positive coefficients of density matrices at all times, hence losing the trace conservation property in the s evolution, as shown by the expression

$$\operatorname{tr}(\mathcal{R}_s \rho_{\text{eq}}) = \int_0^\infty e^{-st} dt = \frac{1}{s}. \tag{2.37}$$

This loss can be compensated by defining the proper formal density matrix $\tilde{\rho}_s$ in the Laplace domain as

$$\tilde{\rho}_s = s\mathcal{R}_s \rho_0, \tag{2.38}$$

with ρ_0 a general initial state. Note however that $\tilde{\rho}_s$ has a physical interpretation only in the limit $s \to \infty$ where it represents the initial state. Every finite value of s cannot be interpreted as a density matrix describing a physical state due to the mixing of contributions over the whole time domain. Yet, the object $\tilde{\rho}_s$ has formally all the properties of a density matrix, namely, it is hermitian, positive, and its trace is equal to one.

We are interested in the s-dependent correlation functions

$$s \operatorname{tr}\left(B\mathcal{R}_s(A\rho_{\text{eq}})\right), \tag{2.39}$$

where A and B are generic self-adjoint operators. Since, our linear master equation (2.25) describes the dynamics for the deviation from equilibrium $\Delta\rho_t$, the magical formula should be applied only to the traceless matrices like $\Delta\rho_t$. For numerical simulations, we can use the following identity to simulate the magical formula with traceless objects and still recover (2.39),

$$\operatorname{tr}(B\rho_{\text{eq}})\operatorname{tr}(A\rho_{\text{eq}}) + \operatorname{tr}(B\mathcal{R}_s\Delta\tilde{\rho}_s). \tag{2.40}$$

The matrix ρ_{eq} being known *a priori*, the traceless matrix $\Delta\tilde{\rho}_s = s(A - \operatorname{tr}(A\rho_{\text{eq}}))\rho_{\text{eq}}$ can be constructed as an initial condition. We then need to evolve the quantity $\Delta\tilde{\rho}_s$ according to the magical formula.

2.2.4 WEAK COUPLING LIMIT

Because we are interested in the limit of vanishing dissipation to regularize the theory, we can further simplify the master equation and the free evolution operator by neglecting the contributions proportional to the decay rate γ_k in the correlation functions of the type (2.39). Due to the truncation in the magical formula for numerical

reasons, only a finite number of collision terms will contribute to the final averages. Furthermore, the collision part (2.29) in the magical formula contributes linearly to correlation functions. Hence, the irreversible part of the collisions does not contribute substantially to the regularization mechanism in the weak dissipation regime. Following our general approach of minimal friction in order to smear the divergences, we neglect all the linear contributions from the friction parameter. In that case, we simplify the collision superoperator $\mathcal{L}^{\text{coll}}$ with the so-called *simplified irreversible dynamics* approximation and neglect the terms proportional to γ_k in the collisions,

$$\mathcal{L}^{\text{coll}}\rho_t = -i[H^{\text{coll}}, \rho_t]. \tag{2.41}$$

The friction provided in the free contribution is sufficient to regularize the ultraviolet divergences from the high momenta. In a similar fashion, we can neglect the linear contribution from the friction parameter in the expansion of the free evolution operator $\mathcal{R}^{\text{free}}_{s+r}$ in order to avoid unwanted exploration of the Hilbert space. Appendix C.2 illustrates an example of how to treat the free evolution operator continuously in the limit of vanishing dissipation. We expect this simplification to correspond to the minimal dissipation needed to regularize the theory.

2.3 STOCHASTIC UNRAVELING

A standard approach to solving quantum master equations in the weak coupling limit is stochastic unraveling, a class of Monte-Carlo-inspired methods that has found many applications in open quantum systems [42, 51–53]. In this section, we review the standard approach to unravel a Lindblad master equation with a quantum jump approach. The choice of this equation is motivated by its simple structure but also by its similarity with our final thermodynamic master equation (2.25). We follow the description of stochastic unraveling in [42].

2.3.1 SINGLE-PROCESS UNRAVELING

The Lindblad equation for density matrices can be represented by a stochastic Schrödinger equation for state vectors. This stochastic representation introduces a piecewise deterministic process $|\Psi_t\rangle$ as the solution of the following differential equation,

$$\mathrm{d}|\Psi_t\rangle = -i\mathcal{G}|\Psi_t\rangle\mathrm{d}t + \sum_\alpha \left(\frac{L_\alpha|\Psi_t\rangle}{\|L_\alpha|\Psi_t\rangle\|} - |\Psi_t\rangle\right)\mathrm{d}N_\alpha(t). \tag{2.42}$$

The linear operator $\mathcal{G}$ dictates the deterministic evolution and has the form

$$\mathcal{G}|\psi_t\rangle = H|\psi_t\rangle - \frac{i}{2}\sum_\alpha \gamma_\alpha \left(1 - |\psi_t\rangle\langle\psi_t|\right) L_\alpha^\dagger L_\alpha|\psi_t\rangle. \tag{2.43}$$

Conversely, the random events are characterized by the independent Poisson processes $N_\alpha(t)$ satisfying

$$\mathrm{d}N_\alpha(t)\mathrm{d}N_{\alpha'}(t) = \delta_{\alpha,\alpha'}\mathrm{d}N_\alpha(t), \qquad \mathbb{E}[\mathrm{d}N_\alpha(t)] = \gamma_\alpha\|L_\alpha|\Psi_t\rangle\|^2\mathrm{d}t. \tag{2.44}$$

These relations imply that the $\mathrm{d}N_\alpha(t)$ are random numbers taking the possible values of 0 or 1. The first term on the right-hand side of Eq. (2.42) proportional to $\mathrm{d}t$ describes a continuous evolution according to the Schrödinger type of equation,

whereas the second term describes the jumps

$$|\psi_t\rangle \mapsto \frac{L_\alpha|\psi_t\rangle}{\|L_\alpha|\psi_t\rangle\|}, \tag{2.45}$$

which occur at rate $\gamma_\alpha\|L_\alpha|\psi_t\rangle\|^2$.

If the initial state is pure, i.e. $\rho_0 = |\psi_0\rangle\langle\psi_0|$, the solution of the original master equation (2.17) can be recovered at any time t from the stochastic equation for the state vector $|\Psi_t\rangle$. The solution in the form of a density matrix is recovered by taking the statistical average

$$\rho_t = \mathbb{E}[|\Psi_t\rangle\langle\Psi_t|]. \tag{2.46}$$

Since both the jumps and the continuous evolution preserve the norm, the solution's norm (2.46) remains unchanged on average. Eventually, one can show using Ito calculus that the expectation value Eq. (2.46) solves the Lindblad equation.

2.3.2 TWO-PROCESS UNRAVELING

One of the advantages of unraveling lies in the fact that it can be generalized to estimate multi-time correlation functions, that is mean values of operators taken at different times. Multi-time correlation functions are a common tool for nonequilibrium processes. The computation of these correlation functions provides information about the spectrum of the Hamiltonian at any time. Here, we generalize unraveling to two-sided state-jumps, which allow us to estimate multi-time correlation functions. To illustrate their usefulness, let us consider the two-time correlation function

$$\mathrm{tr}(B\mathcal{E}_{t_2-t_1}A\mathcal{E}_{t_1-t_0}\rho_0), \tag{2.47}$$

where A, B are general operators, and $\mathcal{E}_{t_1-t_0}$ is the superoperator evolving the density matrix from t_0 to t_1. Since the operators A and B are applied on only one side, the resulting object to evolve from t_1 to t_2 is nonsymmetric. Because the single-sided jumps produce exactly the same dynamics on both bra and ket vectors, we cannot estimate the nonsymmetric matrices in the multi-time correlation functions (2.47) with single-process unraveling. To be able to act differently on both sides of the density matrix, we need to introduce a two-process unraveling acting on the general dyadic $|\Phi_t\rangle\langle\Psi_t|$. The idea is to evolve simultaneously the bra and the ket vectors with jumps occurring at the same time. The solution of the master equation is represented by the general covariance matrix

$$\mathbb{E}[|\Psi_t\rangle\langle\Phi_t|], \tag{2.48}$$

where $|\Psi_t\rangle$, $|\Phi_t\rangle$ are coupled stochastic processes. The continuous deterministic evolution is given by the equations

$$\frac{d}{dt}|\psi_t\rangle = -iH|\psi_t\rangle - \sum_\alpha \gamma_\alpha \left[L_\alpha^\dagger L_\alpha - \frac{\|L_\alpha|\psi_t\rangle\|\|L_\alpha|\phi_t\rangle\|}{\||\phi_t\rangle\|\||\psi_t\rangle\|}\right]|\psi_t\rangle \tag{2.49}$$

and

$$\frac{d}{dt}|\phi_t\rangle = -iH|\phi_t\rangle - \sum_\alpha \gamma_\alpha \left[L_\alpha^\dagger L_\alpha - \frac{\|L_\alpha|\psi_t\rangle\|\|L_\alpha|\phi_t\rangle\|}{\||\phi_t\rangle\|\||\psi_t\rangle\|}\right]|\phi_t\rangle, \tag{2.50}$$

where the second term is added to ensure that the bra and ket vectors stay normalized. Similarly to the one-process unraveling, this term is exactly canceled by the jumps

$$\begin{aligned} |\psi_t\rangle &\mapsto \frac{\||\psi_t\rangle\|}{\|L_\alpha|\psi_t\rangle\|} L_\alpha|\psi_t\rangle, \\ |\phi_t\rangle &\mapsto \frac{\||\phi_t\rangle\|}{\|L_\alpha|\phi_t\rangle\|} L_\alpha|\phi_t\rangle, \end{aligned} \tag{2.51}$$

and occur at a rate $2\gamma_\alpha \frac{\|L_\alpha|\psi_t\rangle\|\|L_\alpha|\phi_t\rangle\|}{\||\phi_t\rangle\|\||\psi_t\rangle\|}$. It can be shown that this two-sided unraveling mimics a generalized application of the superoperator $\mathcal{E}_t$ to dyadics of the form $|\psi_t\rangle\langle\phi_t|$. The multi-time correlation function (2.47) is calculated by unraveling the initial density matrix from t_0 to t_1 using the procedure described above. The operator A is then introduced with a subsequent unraveling of the matrix represented by $A\mathcal{E}_{t_1}\rho_0$. Finally, the operator B is applied.

With a final note, we anticipate the introduction of a new type of two-process unraveling in the next chapter. Dissipation will be included in the continuous evolution and jumps will be associated with reversible interactions. Thus, simultaneous jumps will be replaced by jumps either on the $|\phi_t\rangle$ or on the $|\psi_t\rangle$ side in order to reproduce reversible dynamics.

3 Triplet unraveling

In the previous chapter, we introduced the basic concepts behind the stochastic unraveling of a quantum master equation and emphasized the two-process unraveling to estimate multi-time correlation functions. Parallel to that, we described a theoretical framework for multi-particle systems that introduces a dissipative mechanism to eliminate ultraviolet divergences. The dynamics is described by a linear quantum master equation, whose solution in the Laplace domain takes the form of an infinite resummation of a perturbative expansion. In this chapter, we construct an algorithm called *triplet unraveling*, based on two-process unraveling to solve the quantum master equation (2.25). The main advantage of the simplification 2.2.4 is the ability to construct an unraveling that overcomes the sign problem and reproduces the solution of the master equation where the dissipative part is contained in the continuous part and the jumps are associated with the collision Hamiltonian. The construction of such a numerical scheme is the topic of the following sections. The resulting numerical method has the major benefit to regularize the theory while evolving in d spatial dimensions, where the time dimension is associated to the physical execution time of the simulation. [1]

Without dissipation, the formulation in the Laplace domain allows us to formulate a fixed-point equation for the ground state of H and use the ideas of the newly introduced triplet unraveling. This study is possible due to the structural similarities between this fixed-point equation and the magical formula. We can extend the application of triplet unraveling to study steady-state properties of many-body physics if we introduce a generalized splitting of the Hamiltonian.

This chapter is separated into two sections; the development of triplet unraveling for general dissipative quantum field theoretical systems and the consequences in the case of a vanishing dissipation. We begin by formally showing how the magical formula can be translated into a stochastic unraveling reproducing the solution of the linear quantum master equation (2.25). In the second part, we introduce the fixed-point equation in the Laplace domain to study steady-state properties. This expression is unraveled with the same line of reasoning as the first part due to structural similarities with the magical formula.

3.1 Stochastic unraveling in Laplace domain

We construct an unraveling to solve the quantum master equation (2.25) based on the magical formula. The structure of this formula is naturally suited for piecewise

[1] In connection with our original motivations, this scaling has to be put in perspective with lattice QCD where the simulations evolve in $d+1$ dimensions, with d spatial and one time dimensions.

deterministic process because, in the Fock basis, the term $\mathcal{R}^{\text{free}}_{s+r}$ is solved continuously whereas $(1+\frac{\mathcal{L}^{\text{coll}}}{r})$ accounts for the random transitions. The jump term $\mathcal{L}^{\text{coll}}$ contains a Hamiltonian that acts on either side of the density matrix due to the commutating nature of the reversible dynamics. In a similar fashion to the correlation functions (2.39), the single-process unraveling cannot reproduce the commutator with the Hamiltonian. Therefore, we need the two-process unraveling for the general dyadic $|\Phi_t\rangle\langle\Psi_t|$ to mimic the action of the commutator and, of course, estimate multi-time correlation functions.

We consider the evolution of triplets $(c_m, |\Phi_m\rangle, |\Psi_m\rangle)$, where c_m is complex and $|\Phi_m\rangle$, $|\Psi_m\rangle$ are piecewise deterministic processes. Unlike usual unraveling where the processes evolve in time, here, the evolution is performed with respect to a formal iteration order $m = 0, 1, \ldots$ that corresponds to the m'th term in the sum of the magical formula. We introduce a propagator whose fundamental role is to evolve the triplets from m to $m+1$,

$$T_{r,s} = r\left[\mathcal{R}^{\text{free}}_{s+r}\left(1+\frac{\mathcal{L}^{\text{coll}}}{r}\right)\right]. \tag{3.1}$$

In such a scheme, besides the evolution step $1/r$, we define a minimum $s_{\min}$ value associated to a maximum time $t_{\max} \sim 1/s_{\min}$ that corresponds to a truncation M_{trunc} in the sum of the magical formula. If the truncation is large enough, i.e. if $M^{\text{trunc}} \geq r/s_{\min}$, we can approximate Eq. (2.36) with

$$\mathcal{R}_{s_{\min}} \approx \sum_{m=0}^{M^{\text{trunc}}} \left[T_{r,s_{\min}}\right]^m \mathcal{R}^{\text{free}}_{s_{\min}+r}. \tag{3.2}$$

From this approximation, we can construct stochastic processes that eventually lead to an estimation of the density matrix $\tilde{\rho}_s$, Eq. (2.38). The evolution of these piecewise deterministic processes alternates between continuous evolution according to the free contribution $\mathcal{L}^{\text{free}}$ (2.28) and random jumps associated with $\mathcal{L}^{\text{coll}}$ (2.41). We construct those processes such that for a very large number of iterations $M^{\text{trunc}} \to \infty$, the application of the magical formula is reproduced and the density matrix is estimated by

$$\tilde{\rho}_s = s\sum_{m=0}^{\infty} \mathbb{E}\left[c_m |\Phi_m\rangle\langle\Psi_m|\right], \tag{3.3}$$

where $\mathbb{E}[\cdot]$ represents the statistical average. The continuous evolution associated to the $\mathcal{R}^{\text{free}}_{s+r}$ superoperator can be calculated exactly due to the choice of the Fock basis to represent vectors in the Hilbert space, and it corresponds to a continuous weight update. Between two continuous evolutions, the random jumps account for the application of the superoperator $\left(1+\frac{\mathcal{L}^{\text{coll}}}{r}\right)$. This application is implemented by the two-sided jumps

$$|\phi_m\rangle\langle\psi_m| \mapsto |\phi_m\rangle\langle\psi_m| - \frac{i}{r}\left(H^{\text{coll}}|\phi_m\rangle\langle\psi_m| - |\phi_m\rangle\langle\psi_m|H^{\text{coll}}\right), \tag{3.4}$$

which naturally occur for two-process unraveling. Preventing superposition of quantum states ensures an efficient cancellation of weights and a controlled exploration of the Hilbert space. To apply this superselection rule to the jumps, we decompose the

collision Hamiltonian into the Fock basis $\{|e_i\rangle\}_i$,

$$H^{\text{coll}} = \sum_{i,j} h_{ij}^{\text{coll}} |e_i\rangle\langle e_j|, \tag{3.5}$$

with $h_{ij}^{\text{coll}} = \langle e_i|H^{\text{coll}}|e_j\rangle$. With this decomposition, the collision Hamiltonian is interpreted as an operator producing transitions between Fock states, e.g. from $|e_j\rangle$ to $|e_i\rangle$ with

$$|e_i\rangle\langle e_j|h_{ij}^{\text{coll}}\ |e_k\rangle \propto \delta_{k,j}|e_i\rangle, \tag{3.6}$$

with $\delta_{k,j}$ the Dirac delta function. Since the events occur at a fixed rate r in the Laplace domain, the jumps (3.4) translate into the following rule: at each transition event, we select stochastically a single Fock state from the set generated by $H^{\text{coll}}|\phi_m\rangle\langle\psi_m| - |\phi_m\rangle\langle\psi_m|H^{\text{coll}}$ according to the amplitude of the matrix elements $|h_{ij}^{\text{coll}}/2r|$. Note that the $1/2$ factor accounts for the random selection between $|\phi_m\rangle$ and $|\psi_m\rangle$. We refer to this general procedure as triplet unraveling. On a more philosophical note, the consequences of this superselection rule are in line with the particle ontology of dissipative quantum field theory. At any time, the system has a well-defined particle content because superpositions are not allowed. The philosophical implications of such restrictions have been explored in [38].

3.2 VANISHING DISSIPATION

Without dissipation, the triplet unraveling procedure described above allows us to compute steady-state properties and reversible dynamics for Hamiltonians that are not exactly solvable. Even though it might seem as a step backward, because we introduced dissipation to regularize the theory, this scenario has multiple advantages. It is still sensitive to the critical dynamical sign problem, hence, this simplification allows us to test the ability of our algorithm to overcome this major issue. Additionally, it serves as a simplified situation to illustrate the efficiency of importance sampling. As we will see now, it also provides a numerical framework to simulate the ground state of an unknown Hamiltonian, which can be used as a method to obtain the initial state ρ_{eq} in Eq. (2.39), for example.

We want to generalize the construction of an unraveling for Hamiltonians with the form

$$H = H^{\text{free}} + H^{\text{int}}, \tag{3.7}$$

where the free part is exactly solvable and the interacting part contains the rest of the Hamiltonian. Note that the Hamiltonian does not necessarily describe fundamental particles and their collision rules. Therefore, we now refer to the collisions between those fundamental particles as interactions with H^{int}. With this splitting, the preferred basis is given by the free eigenbasis whereas the interacting part of the Hamiltonian, if considered as a perturbation to the free part, can be seen as inducing transitions between free eigenstates. The superselection rule can be justified purely for computational reasons where efficient cancellation of weights is necessary. The other arguments used to justify the various simplifications to construct the unraveling, e.g. simplified irreversible dynamics are obviously still valid in the case of zero dissipation. Hence, we can naively apply our approach to reversible systems, that is when $\gamma_k = 0$. In that case, the general master equation reduces to the *von Neumann* equation

$$\frac{d\rho_t}{dt} = -i[H, \rho_t], \tag{3.8}$$

whose triplet unraveling is the topic of Chap. 5.

3.2.1 A FIXED-POINT ITERATION SCHEME

Another very useful application of triplet unraveling concerns the symmetrized imaginary-time version of the von Neumann equation, i.e. the equation obtained from the transformation $t \mapsto it \equiv \beta$. This transformation yields the *Bloch equation*

$$\frac{d\rho_\beta}{d\beta} = -\frac{1}{2}\{H, \rho_\beta\}, \qquad \beta = 1/k_B T, \tag{3.9}$$

describing the temperature dependence of a system. The similarities between the von Neumann equation and the Bloch equation motivate us to develop an unraveling procedure to recover the solution of the latter. The formal solution of the Bloch equation is given by

$$\rho_\beta = e^{-\frac{\beta}{2}H}\rho_0 e^{-\frac{\beta}{2}H}, \tag{3.10}$$

with ρ_0 the initial condition. For a vanishing and nondegenerate ground state energy, if we write the general solution as a sum over the eigenstates $\{|E_i\rangle\}_i$,

$$\rho_\beta = \sum_{ij} c_{ij}(\beta = 0) e^{-\frac{\beta}{2}(E_i+E_j)} |E_i\rangle\langle E_j|, \tag{3.11}$$

we can recover the ground state for $\beta \to \infty$, with

$$\lim_{\beta\to\infty} \rho_\beta \propto |E_0\rangle\langle E_0|. \tag{3.12}$$

This interest in the Bloch case is twofold. First, triplet unraveling is associated with an effective numerical method to compute the ground state of an unknown Hamiltonian without any prior knowledge of its structure. It is worth noting that this feature is rarely found in the literature. With the decomposition (3.7), this ground state method can be applied to various systems and models, ranging from spin chains to higher dimensional many-body quantum models. Second, the solution provides the initial condition for the quantum field theoretical computations (see ρ_{eq} in Eq. (2.24)).

Here, we develop a fixed-point iteration scheme, based on the triplet unraveling to compute the ground state density matrix of a general Hamiltonian of the form (3.7). We start by noting that the Bloch equation is not a proper master equation, in the sense that it does not preserve the trace. To recover a legitimate equation with trace conserving properties, we add an energy shift

$$H \to H - S_\rho, \tag{3.13}$$

where $S_\rho = \text{tr}(H\rho)/\text{tr}(\rho)$. Unfortunately, the trace conserving property was introduced at the expense of a nonlinearity, which renders the computation of properties over the whole β range difficult. Hence, we concentrate on the estimation of the ground state only. We wish to construct a fixed-point equation for the ground state

$$\lim_{\beta\to\infty} \rho_\beta = \rho_\infty, \tag{3.14}$$

on which we iterate. From the steady-state equation

$$\mathcal{L}\rho_\infty \equiv -\frac{1}{2}\{H, \rho_\infty\} = 0, \tag{3.15}$$

we multiply both sides by an inverse temperature scale, $1/r$, and recast this equation in the following dimensionless form

$$\left(1+\frac{\mathcal{L}}{r}\right)\rho_\infty = \rho_\infty. \tag{3.16}$$

The superoperator $\mathcal{L} = \mathcal{L}^{\text{free}} + \mathcal{L}^{\text{int}}$ is further decomposed into its free and interaction part, $\mathcal{L}^{\text{free}}$ and $\mathcal{L}^{\text{int}}$, respectively. The above equation can eventually be rewritten as

$$r\left(1+\frac{\mathcal{L}^{\text{int}}}{r}\right)\rho_\infty = \left(r-\mathcal{L}^{\text{free}}\right)\rho_\infty. \tag{3.17}$$

The right-hand side of the above equation is the inverse of the Laplace transform of $e^{\beta\mathcal{L}^{\text{free}}}$, i.e.

$$\mathcal{R}_r^{\text{free}} = \int_0^\infty e^{\beta\mathcal{L}^{\text{free}}} e^{-r\beta} d\beta = \frac{1}{r-\mathcal{L}^{\text{free}}}. \tag{3.18}$$

Once replaced in Eq. (3.17), it leads to

$$r\mathcal{R}_r^{\text{free}}\left(1+\frac{\mathcal{L}^{\text{int}}}{r}\right)\rho_\infty = \rho_\infty, \tag{3.19}$$

which is the fundamental equation for all our ground-state calculations. The strong interest in this equation lies in its formal similarities with the structure of the magical formula and the possibility to apply the ideas of triplet unraveling. In the next section, we construct a similar unraveling for the fixed point ρ_∞.

3.2.2 STEADY-STATE STOCHASTIC UNRAVELING

For systems with a large number of particles, the density matrix cannot be naively stored on a computer. A solution is to represent the ground state ρ_∞ stochastically via an iterative version of the fixed-point equation (3.19),

$$r\mathcal{R}_r^{\text{free}}\left(1+\frac{\mathcal{L}^{\text{free}}}{r}\right)\rho_m = \rho_{m+1}, \tag{3.20}$$

where $1/r$ is the evolution step and $m = 0, 1, \ldots$ is a formal iteration order. If the initial state ρ_0 is chosen close enough to the ground state, in the limit of large $m = m^*$, we recover the ground state with

$$\rho_{m^*} = \rho_{m^*+1} \approx \rho_\infty. \tag{3.21}$$

Due to the similar structure to the magical formula, we use the ideas from triplet unraveling to estimate ρ_∞. We consider the evolution of triplets $(c_m, |\Phi_m\rangle, |\Psi_m\rangle)$, where c_m is real due to the imaginary-time evolution and $|\Phi_m\rangle, |\Psi_m\rangle$ are coupled piecewise deterministic processes. This stochastic unraveling is based on the evolution of trajectories that are represented by triplets $(c_m, |\phi_m\rangle, |\psi_m\rangle)$. These triplets alternate between exact continuous evolution according to the free part and stochastic jumps governed by H^{int}. We construct these processes in such a way that it reproduces the application of Eq. (3.20) on average. This construction guarantees to converge to the solution of Eq. (3.19) for a large number of iterations $m \to \infty$, where the fixed point is recovered as the statistical average

$$\rho_\infty = \mathbb{E}[c_\infty |\Phi_\infty\rangle\langle\Psi_\infty|]. \tag{3.22}$$

As earlier, we choose to represent the realizations of stochastic processes $|\phi_m\rangle$, $|\psi_m\rangle$ in the basis of the free Hamiltonian H^{free}. This choice provides an exact solution to the free evolution $\mathcal{R}_r^{\text{free}}$ and consists in a deterministic weight update. The basis also provides a natural interpretation for the stochastic contribution of the interacting Hamiltonian H^{int} in terms of state-jumps. Because we want to minimize the correlation between the processes $|\phi_m\rangle$ and $|\psi_m\rangle$, we consider the two-sided jumps

$$|\phi_m\rangle\langle\psi_m| \to |\phi_m\rangle\langle\psi_m| - \frac{1}{2r}\left(H^{\text{int}}|\phi_m\rangle\langle\psi_m| + |\phi_m\rangle\langle\psi_m|H^{\text{int}}\right), \tag{3.23}$$

which reproduces on average the application of the superoperator $(1 + \frac{\mathcal{L}^{\text{int}}}{r})$. In order to slow down the exploration of the Hilbert space, we assume the same superselection rule for the jumps and select randomly a single term in the Hamiltonian acting either on $|\phi_m\rangle$ or $|\psi_m\rangle$. The application and numerical analysis of this fixed-point method will be carried out in Chap. 4.

4 Ground-state calculations

In this chapter, we introduce an algorithm based on the unraveling of the fixed-point iteration scheme developed in Sec. 3.2 which allows us to compute the ground state of a quantum system in the form of a density matrix. The reason for developing a method to compute the steady state of a system is twofold. The first is to underline the efficiency of these ground-state calculations compared to other usual methods. The second reason is to provide an initial condition for the dissipative quantum field theoretical calculations (see Sec. 2.2). This technique is comparable in performance to the recent density matrix quantum Monte Carlo technique (DMQMC) [35, 54–58]. As opposed to the DMQMC technique whose time-step $\Delta t \sim 1/r$ is bound by an upper limit, our unraveling does not have a clear bound on the evolution step. Our upper bound for $1/r$ depends on the prior knowledge about the structure of the ground state, the better the insights, the lower the rate r. This freedom increases the convergence speed and reduces the statistical error for an equivalent simulation time.

In what follows, we first recall the fixed-point iterative scheme presented previously as the basis for our stochastic unraveling. After specifying the paradigmatic models, we decompose the algorithm into its main components and explain them in details. Then follows a discussion on the possibility to improve the performance of the algorithm with importance sampling and further approximations. We consider the control over the number of trajectories and analyze the efficiency and accuracy of the method. Finally, we show some concrete examples of ground-state calculations for large systems.

4.1 The fixed-point iterative scheme

Let us start by recalling the main ideas behind the unraveling of the fixed-point iteration scheme introduced in Sec. 3.2. This technique can be implemented as a numerical solver to compute the zero-temperature ground state of a model described by the Hamiltonian

$$H = H^{\text{free}} + H^{\text{int}}, \tag{4.1}$$

where the term free corresponds to the solvable part of the Hamiltonian. With this notation, the iterative fixed-point equation reads

$$r\mathcal{R}_r^{\text{free}} \left(1 + \frac{\mathcal{L}^{\text{int}}}{r}\right) \rho_m = \rho_{m+1}, \tag{4.2}$$

with $\mathcal{L} = -\frac{1}{2}\{H, \cdot\}$, $\mathcal{R}_r = \frac{1}{r-\mathcal{L}}$ and where ρ_m is the density matrix estimated at iteration m. To unravel this equation, we consider triplets of the form $(c_m, |\Phi_m\rangle, |\Psi_m\rangle)$,

where c_m is real and $|\Phi_m\rangle$, $|\Psi_m\rangle$ are piecewise deterministic stochastic processes. The triplets undergo alternately continuous evolution and random jump events reproducing the iterative application of Eq. (4.2). For a large number of iterations m, we expect to retrieve the fixed point via

$$\rho_\infty = \lim_{m\to\infty} \mathbb{E}\left[c_m |\Phi_m\rangle\langle\Psi_m|\right], \tag{4.3}$$

with $\mathbb{E}[\cdot]$ the statistical average. Once the density matrix is estimated and the ground state has been reached, relevant properties can be calculated. For a general observable A the quantum average $\langle A\rangle$ is obtained via

$$\langle A\rangle = \mathrm{tr}(A\rho_\infty). \tag{4.4}$$

4.1.1 STEADY-STATE CALCULATIONS: A SHORT OVERVIEW

With current parallel computers, Monte Carlo (MC) methods allow us to study with high accuracy steady-state properties of systems in many-body physics, quantum chemistry, or nuclear physics [1, 2, 59].

For zero-temperature systems, the best method is probably variational Monte Carlo [60, 61], which stochastically samples configurations to evaluate the expectation values of a trial function. The main issue with this method is that the accuracy of the results highly depends on the initial ansatz for the trial function and requires prior knowledge of the structure of the ground state to obtain a precise result. This issue is partly solved with projector Monte Carlo methods [62–67], such as diffusion Monte Carlo and Green function Monte Carlo. These methods use a projector to enhance the ground-state contribution from an initial trial function. To further improve the quality of the results, the fixed-node approximation [68, 69] takes advantage of a prior knowledge of the nodal structure of the ground state to reproduce the antisymmetry of the wave function. The efficiency of this approximation obviously depends on how precise the knowledge of the ground state is. While for bosons, these methods have proven extremely successful and have provided nearly exact results [70–72], fermionic simulations are seriously handicapped by the sign-problem [44, 73, 74]. Independently, full configuration interaction quantum Monte Carlo was introduced in [56, 57] to investigate the zero-temperature properties of correlated electrons, without any prior knowledge of the ground state. This projector method simulates stochastic trajectories in the space of Slater determinants. This technique is based on an efficient annihilation of undesired Monte Carlo walkers [46, 58] and overcomes the sign problem without requiring any prior knowledge about the nodal structure of the many-body wave-function.

For finite temperature systems, auxiliary field Monte Carlo [11, 12, 75, 76] and path integral Monte Carlo [77–79] are both capable of simulating strongly interacting particles. They express the partition function as a sum of paths in the Hilbert space, with appropriate probabilities for sampling the paths. Even though the systems they consider are not realistic, they helped understand the structure of neutron stars [80], for example. Inspired by full configuration interaction quantum Monte Carlo, density matrix quantum Monte Carlo has been developed in [35] to study finite temperature models of correlated fermions [54, 55]. Similarly to full configuration interaction quantum Monte Carlo, this algorithm simulates stochastic trajectories in the space of operators and estimates temperature-dependent density matrices. It offers independent estimations for the density matrix elements, hence minimizing the correlations. Moreover, this method offers the possibility to obtain estimates of the entanglement

between different degrees of freedom of the system. Recently, DMQMC has been generalized to open quantum systems described by a Lindblad-type master equation and applied to dissipative quantum magnetism [81].

4.1.2 PARADIGMATIC MODELS

Certain paradigmatic models are often used as a benchmark for novel approaches to ground state simulations. These systems generally consider lattice models which give enough freedom in the size of the system to perform exact diagonalization and to test the performances on larger lattices. Furthermore, it is common that specific configurations of these models are sensitive to the sign problem, allowing us to test the efficiency in dealing with it. First, we consider the two-dimensional Heisenberg model displaying magnetic behavior [82]. Despite the appeal of its simple formulation, no rigorous general solution has been provided and it is still studied extensively by Monte Carlo simulations [83, 84]. As an example of ground state computations in field theoretical models, we also consider the more challenging Fermi-Hubbard model on an $L \times L$ square lattice with periodic boundary conditions [9]. This model is of major importance because it describes several important phenomena in solid state physics, such as high-temperature superconductivity [85]. An exact general solution has never been found although decades of study that have been spent on the Fermi-Hubbard model [86].

Note that the basis choice is usually not unique in lattice models, because the Hamiltonian is composed of multiple independent solvable parts. We selected a single basis per model, but the simulations could have been performed in another basis, corresponding to another splitting between the free and interacting parts.

Square Heisenberg model We consider a $L \times L$ square lattice with periodic boundary conditions on which a spin-1/2 particle sits on each site. The Hamiltonian takes the form

$$H = \sum_{\langle \nu,\mu \rangle} J^x \sigma^x_\nu \sigma^x_\mu + J^y \sigma^y_\nu \sigma^y_\mu + J^z \sigma^z_\nu \sigma^z_\mu, \tag{4.5}$$

where $\sigma^x, \sigma^y, \sigma^z$ are the standard Pauli matrices and $\langle \nu, \mu \rangle$ denotes nearest neighbors on the lattice. The Hamiltonian of the XXZ model is obtained by setting $J^x = J^y = 2J^z = J$,

$$H = \frac{J}{2} \sum_{\langle a,b \rangle} \sigma^+_a \sigma^-_b + \sigma^-_a \sigma^+_b + \sigma^z_a \sigma^z_b, \tag{4.6}$$

where $\sigma^\pm = \sigma^x \pm i\sigma^y$. The splitting into a free and interacting part is chosen such that

$$H^{\text{free}} = \frac{J}{2} \sum_{\langle a,b \rangle} \sigma^z_a \sigma^z_b, \qquad H^{\text{int}} = \frac{J}{2} \sum_{\langle a,b \rangle} \sigma^+_a \sigma^-_b + \sigma^-_a \sigma^+_b. \tag{4.7}$$

We introduce the free eigenbasis as a tensor product of local eigenvectors of the single-particle operator σ^z

$$|e_{s_1,\ldots,s_{L\times L}}\rangle = |s_1\rangle \otimes |s_2\rangle \otimes \cdots \otimes |s_{L\times L}\rangle, \tag{4.8}$$

where $s_\nu = s^z_\nu = \pm 1$. A free eigenstate describes a precise spin configuration of the lattice, where each site is either in a state with spin up or down. The single-particle operators σ^z and $\sigma^\pm$ act on the basis states according to the standard algebra of Pauli

matrices

$$\sigma^z|\pm 1\rangle = \pm|\pm 1\rangle, \qquad \sigma^\pm|\mp 1\rangle = |\pm 1\rangle, \qquad \sigma^\pm|\pm 1\rangle = 0. \tag{4.9}$$

Because the total spin operator is a conserved quantity, we can restrict ourselves to subspaces of the Hilbert space with constant total spin. For the antiferromagnetic case, the ground state has total spin zero, and we can therefore only consider states with the same number of spins up and down. The number of allowed configurations for a $L \times L$ lattice is given by the binomial

$$\binom{L^2}{L^2/2}, \tag{4.10}$$

and the number of elements in the density matrix is

$$\binom{L^2}{L^2/2}^2. \tag{4.11}$$

Besides the ground state energy, a common observable is the staggered magnetization per site defined as

$$\mathbf{M} = \frac{1}{L^2}\sum_{\mu=1}^{L^2}(-1)^{x_\mu+y_\mu}\mathbf{S}_\mu, \tag{4.12}$$

where $\mathbf{S}_\mu$ is the 3-dimensional spin operator on site μ and (x_μ, y_μ) are the coordinates of the site μ on a square lattice. The squared staggered magnetization is defined as

$$\langle M^2\rangle = \langle \mathbf{M}\cdot\mathbf{M}\rangle, \tag{4.13}$$

where $\langle\cdot\rangle$ denotes the quantum average.

Triangular Heisenberg model The triangular Heisenberg model is based on the square Heisenberg model with next-nearest neighbors interactions. Calculations with this model usually display the effects of the sign problem. Its Hamiltonian reads

$$H = \sum_{\langle\langle\nu,\mu\rangle\rangle} J^x\sigma_\nu^x\sigma_\mu^x + J^y\sigma_\nu^y\sigma_\mu^y + J^z\sigma_\nu^z\sigma_\mu^z, \tag{4.14}$$

where $\langle\langle\nu,\mu\rangle\rangle$ denotes the next-nearest neighbors on the lattice, meaning that each point in the lattice has six neighbors. Such a lattice is displayed in Figure 4.1.

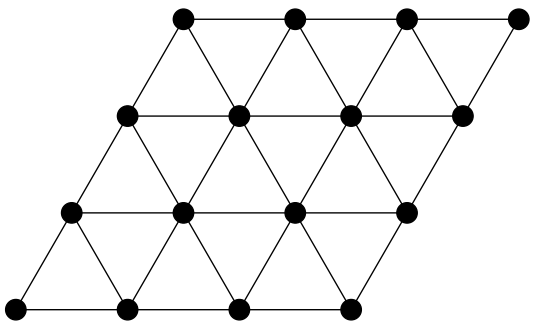

FIGURE 4.1: Illustration of a triangular 4×4 lattice. Each black dot represents a spin on the lattice and has 6 neighbors.

The total spin is conserved and the number of allowed configurations is given by Eq. (4.10). However, since the lattice is triangular, the sign problem occurs. Its presence can be explained by the fact that in three jumps, a triplet can be back to its original position, which was not the case with the square lattice. With each minus sign accompanying a jump, the triplets contribute to the averages with weights from opposite signs. The consequence of these opposite contributions is a typical scenario where the signal diverges because weights cannot cancel each other exactly. Due to the rotation symmetry of the Hamiltonian, choosing the eigenbasis of σ^x or σ^z for the free basis does not solve the sign problem. For both the triangular and the square Heisenberg model, we assume $J = 1$ unless stated otherwise.

Hubbard model The $L \times L$ square Fermi-Hubbard Hamiltonian with periodic boundary conditions is

$$H = -t \sum_{\sigma=\{\uparrow,\downarrow\}} \sum_{\langle \nu,\mu \rangle} b_\nu^{\sigma\dagger} b_\mu^\sigma + U \sum_\nu n_\nu^\uparrow n_\nu^\downarrow, \tag{4.15}$$

where $\nu = 1, \ldots, L^2$ are the lattice sites, $\langle \nu, \mu \rangle$ denotes nearest neighbours on the lattice, and $n_\nu^\sigma = b_\nu^{\sigma\dagger} b_\nu^\sigma$ counts the number of particles with spin σ at site ν. The fermionic ladder operators $b_\nu^{\sigma\dagger}$, b_ν^σ follow the standard anti-commutation rules (2.13). The splitting into a free and an interaction part is performed according to

$$H^{\text{free}} = U \sum_\nu n_\nu^\uparrow n_\nu^\downarrow, \qquad H^{\text{int}} = -t \sum_{\sigma=\{\uparrow,\downarrow\}} \sum_{\langle \nu,\mu \rangle} b_\nu^{\sigma\dagger} b_\mu^\sigma. \tag{4.16}$$

Note that, unlike most approaches, we treat the kinetic hopping term as the interaction and the Coulomb on-site potential as the free part of the Hamiltonian. This is due to the Fock basis, however, we could perform a Bethe ansatz to write the Hamiltonian in a form where the role of the free and interacting parts are interchanged. The Fock basis is spanned by the vectors

$$|n_1^\uparrow, n_1^\downarrow, n_2^\uparrow, \ldots, n_{L^2}^\downarrow\rangle = {b_1^\uparrow}^{\dagger n_1^\uparrow} {b_1^\downarrow}^{\dagger n_1^\downarrow} {b_2^\uparrow}^{\dagger n_2^\uparrow} \ldots {b_{L^2}^\downarrow}^{\dagger n_{L^2}^\downarrow} |0\rangle, \tag{4.17}$$

with $|0\rangle$ the vacuum and where n_ν^σ can either take the value 0 or 1. We say that the grid is half-filled when the number of electrons on the grid is L^2. In that case, the ground state consists in a linear combination of states where the number of spin up electrons is exactly equal to the number of spin down. This reflects the fact that the Coulomb energy is minimized when electrons are not on the same site. Noticing that the Hamiltonian conserves the total spin, we can restrict ourselves to

$$\#\text{ lattice config.} \sim \binom{L^2}{L^2/2}^2, \tag{4.18}$$

due to the fact that the spins up and down are completely decoupled in the jumps. This results in two $L \times L$ independent lattices, with $L^2/2$ electrons on each.

4.2 The algorithm

We now present the details of the algorithm to unravel Eq. (4.2). We introduce the general structure and describe how to obtain a ground state estimation with these basic structural components. Then, we have a closer look at the main loop, the key

component of the algorithm. And finally, we define an importance sampling procedure and review the initiator approximation introduced in [57] that has a strong impact on the severity of the sign problem.

4.2.1 General structure

Triplet unraveling considers the evolution of an ensemble of walkers, or trajectories, as particular realizations of the stochastic processes $(c_m, |\Phi_m\rangle, |\Psi_m\rangle)$ to statistically represent the density matrix. These walkers is the ensemble of triplets $\{(c^{(n)}, i^{(n)}, j^{(n)})\}_n$, where $c^{(n)}$ is real, and $i^{(n)} \equiv |e_i^{(n)}\rangle$ are the free Hamiltonian eigenbasis. Note that we use the superscript n to denote the n'th independent trajectory of the ensemble. We dropped the subscript m denoting the order of iteration because it did not carry any special physical meaning. The triplets $(c^{(n)}, i^{(n)}, j^{(n)})$ undergo alternately weight updates to account for the continuous free evolution and stochastic state-jumps representing the interactions. From this ensemble of trajectories, the average defined in Eq. (4.3) is estimated via

$$\rho \approx \frac{1}{\mathcal{N}} \sum_n c^{(n)} |i^{(n)}\rangle\langle j^{(n)}|, \tag{4.19}$$

where $\mathcal{N} = \sum_n c^{(n)} \delta_{i^{(n)},j^{(n)}}$ is the normalization. To keep track of the number of trajectories in our ensemble, we define the *population* P as the sum of the absolute value of all the triplets in the ensemble,

$$P = \sum_n |c^{(n)}|. \tag{4.20}$$

The general strategy to compute an estimation of the ground state $|E_0\rangle\langle E_0|$ consists in three stages; an initialization, a convergence, and a sampling. The initialization matches the initial triplet ensemble to the initial condition ρ_0 such that Eq. (4.19) holds. The only restriction on the initial condition is that it cannot be perpendicular to the ground state. However, in order to guarantee a fast convergence, it is computationally efficient to start as close as possible to the ground state. Usually, the system is initialized to the free ground state, which is by construction always known. The details about the choice of the initial condition are developed in Sec. 4.4. The convergence is made of an iterative application of the so-called *main loop* on the ensemble until the latter has reached the ground state. The main loop aims at imitating the application of the superoperators in Eq. (4.2). A single loop is decomposed into two steps, the *spawnings* or interactions and the *free evolution*. The spawnings represent the random events followed by transitions encountered by the piecewise deterministic processes, whereas the free evolution corresponds to the continuous deterministic evolution. Once the simulation has converged and the ground state has emerged, the sampling stage occurs. From the converged ensemble, each further application of the main loop produces an estimate of the mean value of an observable A via $\mathrm{tr}(A\rho)$. Using Eq. (4.19), the mean value can be estimated from the triplet ensemble $\{(c^{(n)}, i^{(n)}, j^{(n)})\}_n$ with

$$\mathrm{tr}(A\rho) \approx \frac{1}{\mathcal{N}} \sum_n c^{(n)} a_{i^{(n)} j^{(n)}}, \tag{4.21}$$

with $a_{i^{(n)} j^{(n)}} = \langle i^{(n)}|A|j^{(n)}\rangle$. Once the sampling stage is finished, one performs a block analysis to decorrelate the samples and estimate the correct statistical error.

Typically, we refer to such an estimation procedure as an independent simulation. Multiple independent simulations are usually performed to estimate the statistical error of intermediate results in a numerical analysis of the scheme.

4.2.2 MAIN LOOP

We now discuss in details the main loop, which is illustrated by a flowchart in Fig. 4.2. The implementation of the spawning and free evolution steps of the main loop is described below.

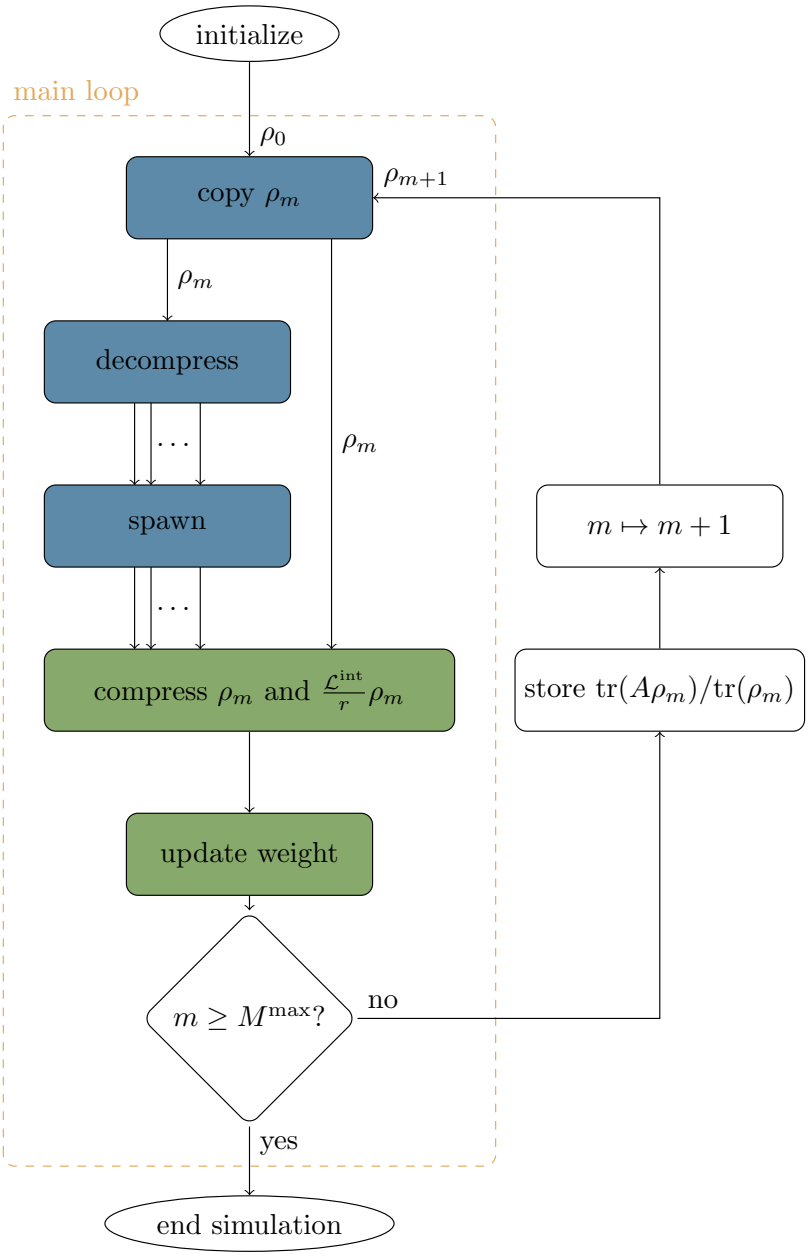

FIGURE 4.2: Flowchart of the triplet unraveling algorithm. The orange rectangle represents the main loop, the collection of blue rectangles is the superoperator $(1 + \frac{\mathcal{L}^{\text{int}}}{r})$ and the free $r\mathcal{R}_r^{\text{free}}$ is represented by the green rectangles.

Spawning

1. Prespawning decompression.

2. For each unit-weight triplet $(\mathrm{sign}(c^{(n)}), i^{(n)}, j^{(n)})$ either one of the two states is chosen randomly. For instance, if $i^{(n)}$ is chosen, a new state k is spawned from $i^{(n)}$ with uniform probability among the n_t possible transitions with $h^{\mathrm{int}}_{i^{(n)}k} = \langle k|H^{\mathrm{int}}|i^{(n)}\rangle \neq 0$. Then, the newly spawned triplet,

$$\left[-\mathrm{sign}(c^{(n)})\frac{h^{\mathrm{int}}_{i^{(n)}k}}{r}n_t, k, j^{(n)}\right], \tag{4.22}$$

   is added to the ensemble. Equivalently if $j^{(n)}$ is selected.

The spawning step numerically implements the stochastic application of the superoperator $(1 + \frac{\mathcal{L}^{\mathrm{int}}}{r})$. Prior to the execution of the spawnings, we perform a modification of the ensemble to improve the statistics without influencing the statistical averages. A prespawning *decompression* splits each triplet (c, i, j) into child triplets of weight unity in absolute value $(\mathrm{sign}(c), i, j)$ and a rest triplet with weight $c_r = \mathrm{sign}(c)(|c| - \lfloor|c|\rfloor)$, with $\lfloor\cdot\rfloor$ the floor function. The rest triplet is remove from the simulation with probability $1 - |c_r|$ or its weight is updated to $\mathrm{sign}(c)$. Once all the triplets have spawned exactly once, we can apply the free evolution step.

Free evolution

1. Triplets compression.

2. For each triplet $(c^{(n)}, i^{(n)}, j^{(n)})$ a weight update is performed according to

$$c^{(n)} \mapsto \frac{r}{r - S + (h^{\mathrm{free}}_{i^{(n)}i^{(n)}} + h^{\mathrm{free}}_{j^{(n)}j^{(n)}})/2}c^{(n)}, \tag{4.23}$$

   in order to account for the free evolution, with S the energy shift.

The free evolution step describes the continuous evolution of the piecewise stochastic processes according to $r\mathcal{R}^{\mathrm{free}}_r$. Again, we first perform a modification of the ensemble. A *compression* is applied on a decompressed ensemble and forms classes of triplets according to the pair (i, j). Class representatives are then replaced by a single triplet with weight being the sum of all the weights in the class.

Once the above steps are performed, an estimate of the average $\langle A\rangle$ can be calculated according to (4.21). Once the desired population is reached, the shift has to be updated according to the rule

$$S_m = S_{m-1} - r\xi \log\left(P_m/P_{m-1}\right), \tag{4.24}$$

where S_m denotes the shift at loop m, ξ is a damping parameter and P_m is the population. The shift update eventually helps to stabilize the population. The shift is guaranteed to converge to the true ground state energy. A thorough analysis of the shift dependence on the population dynamics is performed in Sec. 4.3.

4.2.3 IMPORTANCE SAMPLING

We introduce an importance sampling procedure to reduce the variance of our final results without modifying the averages. The idea of this procedure is to restrict the

exploration of the Hilbert space via the spawnings to only the region of interest for an observable A. In order to have a measure of distance in the Hilbert space, we define a *dynamic norm* n_{ij} between states i and j that will allow us to control how far the triplets can explore around the desired region. Because the exploration is dictated by the spawnings, this norm measures the minimum number of applications of H^{int} needed to jump from state i to state j. The efficiency of this importance sampling procedure resides in the observation that most of the observables are sampled by triplets with a dynamic norm strictly lower than two. Intuitively, one can imagine this procedure as keeping the triplets close to the diagonal.

In order to implement this idea, we associate to each triplet two weights; a *physical* weight and an *ensemble* weight. The physical weight, denoted by c, is the weight used until now for physical averages of the type (4.21). The ensemble weight w is associated to the number of spawnings performed by the triplet and represents the statistical importance of the triplet in the ensemble. The two weights are related by a norm dependent bias $b \equiv b(n_{ij})$ with the relation $c = bw$. In order to decrease the number of triplets with a large dynamic norm, we have to reduce the number of spawnings performed and hence, impose that the bias increases with an increasing norm. In that case, triplets with a large dynamic norm have a low ensemble weight and spawn less. Figure 4.3 illustrates an example of the spawning procedure for a triplet with physical weight $|c| = 6$ and $b = 2$.

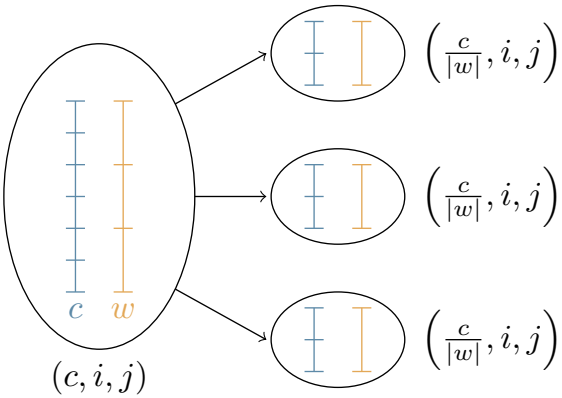

FIGURE 4.3: Example of the decompression of a triplet (c, i, j) according to the ensemble weight w. The triplet with $|c| = 6$ and bias $b = 2$ is split into $\lfloor |w| \rfloor = 3$ child triplets, with each child triplet spawning a single triplet from $(\frac{c}{|w|}, i, j)$.

To be more concrete, the decompression has to be performed according to the ensemble weights to reflect the number of spawnings. A triplet (c, i, j) is split into $\lfloor |w| \rfloor$ child triplets with physical weight $c/|w|$ and a rest triplet that survives with probability $|w| - \lfloor |w| \rfloor$. If the rest triplet survives, its weight is updated to $c/|w|$ otherwise it is removed from the simulation. Concerning the spawnings, for each child triplet, a side is randomly chosen as well as a subsequent new state among all the possible transitions. If the side i was chosen to spawn a new k, the newly spawned triplet has the form

$$\left[-\frac{c^{(n)}}{|w^{(n)}|} \frac{h^{\text{int}}_{i^{(n)}k}}{r} n_t T_b, k, j^{(n)} \right], \tag{4.25}$$

with $T_b = b_{ij}/b_{ik}$ the transition bias. This equation is the importance sampled counterpart of Eq. (4.22).

A standard choice for the bias b is inspired by a harmonic interaction with spring constant κ between the i and j. It is expressed as

$$b(n_{ij}) = \exp\left(\kappa n_{ij}^2\right), \tag{4.26}$$

such that the initial ensemble is unbiased due to $b(0) = 1$. Note that the choice of the definition of the dynamic norm is not unique. In some systems, it can be computationally expensive to compute at every spawning event both the dynamic norm of the original and the newly spawned triplets. As a solution, we can define an equivalent norm that has a similar role. The only requirements for the dynamic norm are (i) to be computationally cheap and (ii) to resemble the definition given above to reduce the number of spawnings for unimportant triplets.

4.2.4 Initiator approximation

The initiator approximation introduced in [57] reduces the number of triplets needed to have a convergent simulation when the sign problem occurs. The idea is to allow the triplets to spawn a nonexisting triplet only if the original triplet has a weight larger than a threshold c_{ini} or a dynamic norm strictly lower than n_{ini}. Those triplets are called initiators. The only exception to this rule is if two non-initiators spawn simultaneously the same pair. A non-initiator can become an initiator if its weight reaches the threshold c_{ini}. In our framework, the approximation is implemented in the compression and decompression. The initiator compression removes all the newly created triplets that originate from non-initiators. Otherwise, a usual compression is performed. Conversely, the initiator decompression upgrades to initiators all triplets with weight larger c_{ini} or dynamic norm strictly lower than n_{ini}. It is followed by a standard decompression. We assume the initiator parameter $n_{\text{ini}} = 2$ unless stated otherwise.

4.3 Population control

Introduced earlier as the sum over the absolute value of the weight of all the triplets in an ensemble, the population reflects the computational cost of each loop. Each triplet spawns a number of children proportional to its weight, hence a larger population accounts for a longer computational time. It is crucial to have good control over the population dynamics in order to have a predictable execution time and to avoid unnecessary growth of the ensemble size.

We here examine the tools to control the population dynamics. These tools include the shift update, which is parameterized by the initial shift and the damping parameter ξ, and indirectly, the importance sampling via the spring constant. We also review the population plateaus that are encountered in systems sensitive to the sign problem. Unless stated otherwise, the damping parameter is set to $\xi = 1$.

4.3.1 Shift update

Because our method has similarities with the full configuration interaction quantum Monte Carlo method, we can rely on the analysis done in [56] about the population dynamics. We recall here the most important features and properties of the evolution of the population and the main tool to control it, the shift.

For a shift larger than the ground state energy $S > E_0$, the ensemble size naturally increases exponentially as it can be understood with Eq. (3.11), for which the population would be

$$\sum_{ij} |c_{ij}(\beta = 0)| e^{\frac{\beta}{2}|E_i + E_j - 2S|}, \tag{4.27}$$

which would increase exponentially for $\beta \to \infty$. In the Laplace domain, the same conclusions can be drawn by considering the fixed-point equation and the decomposition $\rho_m = \sum_{ij} c_{ij}(m)|E_i\rangle\langle E_j|$. We find that the population at iteration m is

$$\sum_{ij} |c_{ij}(m = 0)| \left(1 + |E_i + E_j - 2S|/2r\right)^m, \tag{4.28}$$

which diverges for $m \to \infty$. The purpose of the shift update is hence to counteract this natural increase by adjusting the shift to the ground state energy, which slows down and eventually stops the growth.

In practice, the slowing down is achieved by updating the shift according to the rule Eq. (4.24) once the desired population is reached. Figure 4.4 shows three examples of population dynamics with the corresponding estimation of the ground state energy E_0 for the 4×4 square Heisenberg model with $r = 30$. The initial shifts were all set to $S_0 = -9$ and the update was enabled at $m/r = 1,\ 2,\ 4$. For sign-

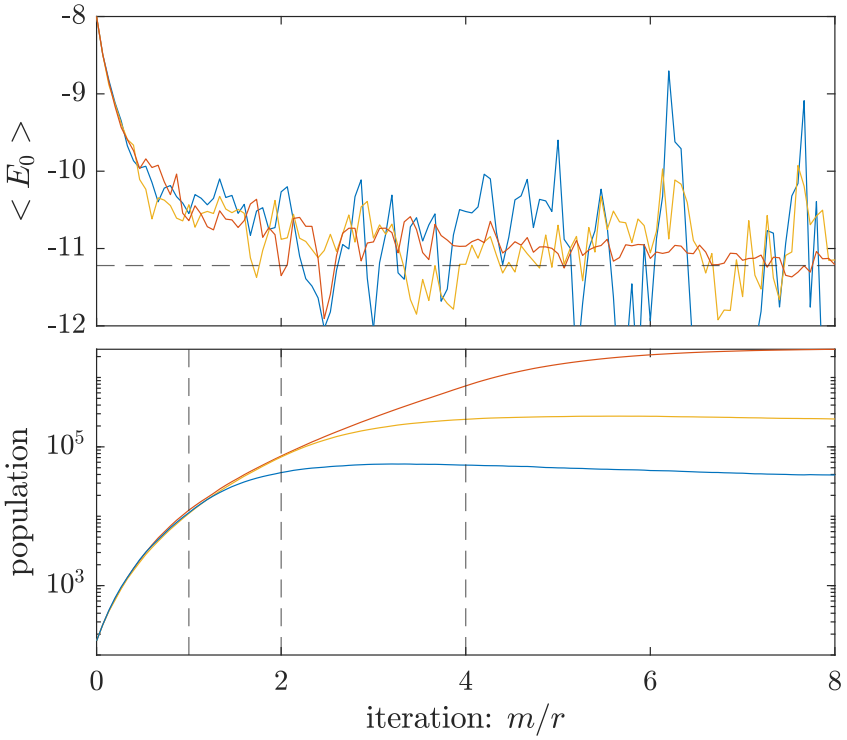

FIGURE 4.4: Upper panel: Estimation of the ground state energy $\langle E_0 \rangle$ for the 4×4 square Heisenberg model with $r = 30$. Lower panel: Corresponding population dynamics with initial shift $S_0 = -9$ and update enabled at $m/r = 1,\ 2,\ 4$. The corresponding line colors are blue, yellow, red, respectively.

free problems like the square Heisenberg, the shift can be updated anytime, and the simulations are convergent for all populations. Conversely, for systems sensitive to the sign problem, the population has to reach a typical plateau in order to provide

a convergent simulation. The shift can be updated only once the plateau is exited. These population plateaus are considered in the next subsection.

4.3.2 POPULATION PLATEAUS

As mentioned earlier, the triangular Heisenberg model is a paradigmatic model to study the sign problem. Due to the possibility of a triplet to jump back into its original state after an odd number of iterations, and to the negative sign associated to a spawning in Eq. (4.22), triplets with opposite weights cannot cancel exactly, giving rise to the sign problem. Above a critical spawning rate, the instabilities disappear because the cancellation rate is high enough to overcome the sign problem. This critical value manifests itself as a population plateau as shown in Fig. 4.5. It illustrates the population dynamics for the 4×4 triangular Heisenberg model with $r = 15$ and various constant shifts.

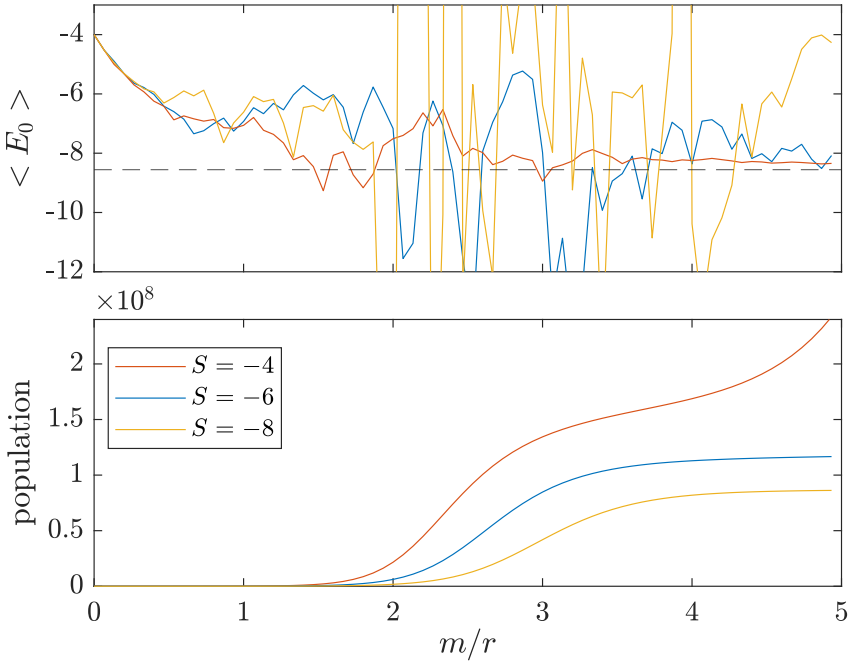

FIGURE 4.5: Upper panel: Estimation of the ground state energy $\langle E_0 \rangle$ for the 4×4 triangular Heisenberg model with $r = 15$. Lower panel: Corresponding population dynamics with various constant shifts and an initial population of 160 triplets.

First, an exponential growth in the population occurs due to the rapid spreading of the triplets in the Hilbert space. This initial spreading depends of course on the choice of the initial shift as supported by Eq. (4.28) and the above figure. Then, the triplet population stabilizes at a critical plateau height because of competing contributions from triplets with opposite weight signs. Details can be found in [56] about the dependence on the plateau height and length with respect to the initial shift. Finally, a second exponential growth originating from a nonzero ground state energy emerges, signaling that the ground state has been reached and the shift update can be enabled. The closer the initial shift is to the ground state energy, the longer the emergence of the ground state has to be during the plateau. This is due to a slow initial spreading of the triplets in the Hilbert space. Hence, the ground state has to reinforce itself before emerging from the divergent simulation. If the shift update is enabled before the end of the population plateau, the simulations are not convergent

because the ground state has not emerged, and the weight cancellation rate has not reached the critical value.

An efficient way to shorten the length of the population plateau is to use the initiator approximation. The population dynamics and the corresponding ground state energy estimate are displayed in Fig. 4.6 for a 4×4 triangular Heisenberg model with $r = 15$, $S = -4$, an initial population of 160 triplets and the initiator approximation. As it is illustrated by the converged ground state energy estimations,

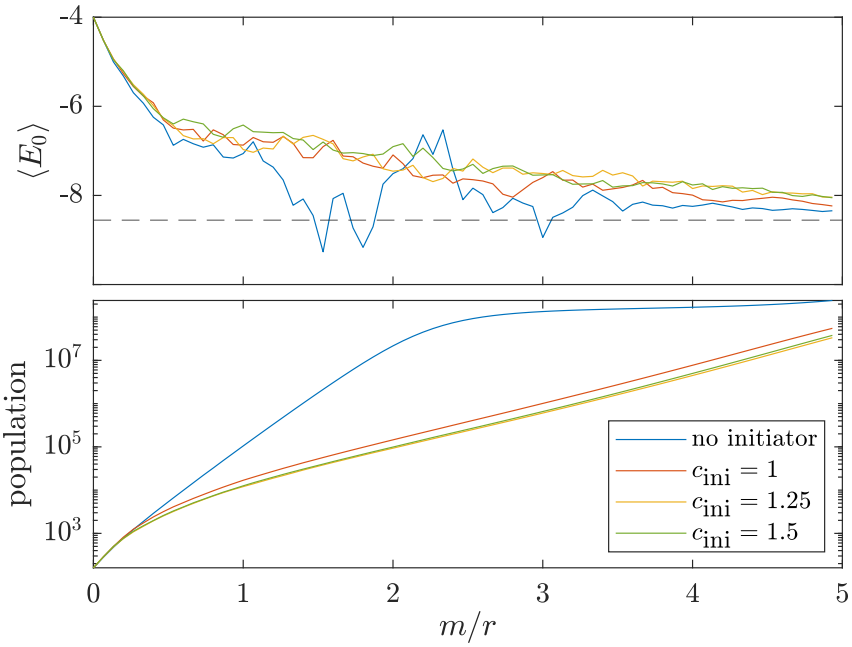

Figure 4.6: Upper panel: Estimation of the ground state energy $\langle E_0 \rangle$ for the 4×4 triangular Heisenberg model with $r = 15$, a constant shift $S = -4$ and an initial population of 160 triplets. Lower panel: Corresponding population dynamics with various initiator thresholds c_{ini}.

the severity of the sign problem is weakened with the initiator approximation. The reason is that the initiator approximation forbids the triplets contributing the most to the sign problem to spawn, which improves the weight cancellation rate.

4.3.3 Spring constant

Importance sampling is introduced to decrease the statistical variance of the final result by restricting the exploration of the Hilbert space only to regions that participate in the statistical averages. In fact, the main effect of the importance sampling is to reduce the population of triplets with a large dynamical norm, leading to a lower total population. The variance is effectively unchanged but the population is lowered, hence the execution time to produce a given statistical error is shortened.

Figure 4.7 shows the dependence of the population dynamics on the spring constant κ for the 4×4 square Heisenberg model. Since the shift is updated from $m/r = 2$ for all the curves, the spring constant has a direct impact on the initial spreading in the Hilbert space and therefore on the final population. For sign-free systems, the shift update can be enabled during the initial exploration phase of the Hilbert space, which affects the final population. Many triplets do not spread easily due to the spring constant, and the total population is effectively lowered because

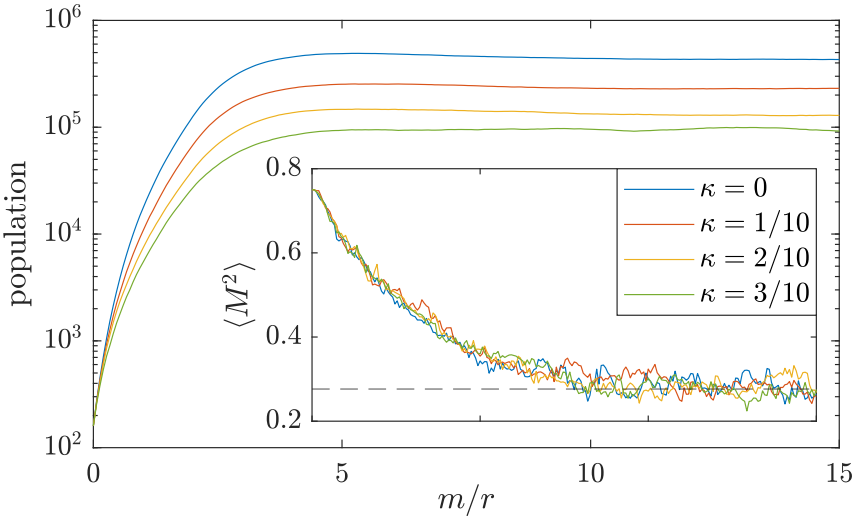

FIGURE 4.7: Population dynamics for the 4×4 square Heisenberg model with $r = 15$, an initial shift $S_0 = -9$, and various spring constants. The shift update was enabled at $m/r = 2$. Inset: Estimation of the ground state squared staggered magnetization $\langle M^2 \rangle$ for the corresponding population dynamics.

the early shift update stabilizes the number of triplets to a lower level. As already claimed, the variance of the final result is constant for all κ. The desired variance reduction occurs by increasing the population to match the execution time without importance sampling.

Conversely, for the triangular Heisenberg model, the spring constant has no direct effect on the final population but rather on the variance. This is due to the impossibility to update the shift before the plateaus are exited. Figure 4.8 illustrates the effect of the importance sampling on the population dynamics for the 4×4 triangular Heisenberg model. The same initial growth as for the square model is visible but the importance sampling does not influence the height of the population plateau. The weight cancellation rate has to be reached to overcome the sign problem leading to the same plateau height. However, the inset shows a reduction of the noise which is a consequence of the variance reduction method. Therefore, the effect of importance sampling for systems sensitive to the sign problem is a reduction of the statistical error and not a lowering of the plateau height.

It is worth noting that if the spring constant is chosen too large, some triplets that should participate in the statistical averages might be removed from the simulation. This can lead to a convergence to the wrong ground state, which is detectable by an underestimation of the ground state energy. This can be viewed as a breaking of ergodicity in the exploration of the Hilbert space by restricting the jumps to a specific region. The exact value of the spring constant at which the exploration is no longer ergodic increases with the population. Figure 4.9 illustrates the breaking of ergodicity by plotting the estimate of the ground state energy for various spring constants for the $L = 8$ Fermi-Hubbard ring. For this specific population, the breaking of ergodicity occurs for $\kappa \geq 0.3$ where the statistical errors become smaller than the systematic ones. When the ground state energy is unknown, the typical strategy to assess when the breaking of ergodicity occurs is to start with a large spring constant and decrease it until the ground state energy becomes constant within the error bars.

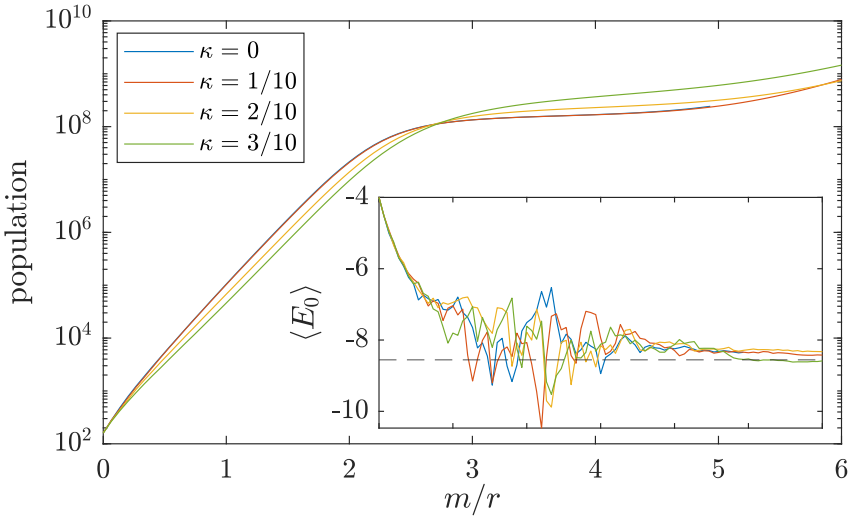

Figure 4.8: Population dynamics for the 4×4 triangular Heisenberg model with $r = 15$, a constant shift $S_0 = -4$, and with various spring constants. Inset: Estimation of the ground state energy $\langle E_0 \rangle$ for the corresponding population dynamics.

4.4 Efficiency and accuracy

The algorithmic complexity measures how the execution time scales with a given population. Indirectly, it gives a useful quantitative scaling about the additional computational time needed to reduce the statistical error. Most of the simulation effort has to be performed during the spawning step, especially when computing the allowed transitions and creating new states. Because the triplet population reflects the number of spawning attempts performed in each loop, we can expect that the algorithmic complexity scales linearly with the population, i.e. $\mathcal{O}(P)$. One could argue that the use of sorted ensembles implies the complexity $\mathcal{O}(P \ln P)$, however, within the range of population accessible with current computers, the sorting steps of the ensembles are negligible compared to the spawnings in terms of execution time. Figure 4.10 illustrates the algorithmic complexity for the $L = 8$ Fermi-Hubbard ring with $t = 1$, $U = 20$, and $r = 64$ at half-filling. As illustrated, the execution time is determined by the linear relation with the triplet population, mainly controlled by the shift update. Hence, after defining the desired population, we can tune the parameters of the algorithm to improve the accuracy of the result for a given simulation time.

In this section, we show how to tune the parameters in order to optimize the efficiency of the algorithm and perform a numerical analysis of the method. We first examine the role of the initial conditions in the convergence rate, then we compare the efficiency to other similar Monte Carlo methods. We conclude that in our Laplace framework, the freedom to choose the parameter r can be used as a way to improve the statistics of the final results and hence, the computational time. Finally, we study the high parallelism of the algorithm, the implementation of the parallel programming, and the speed-up in the simulation time.

4.4.1 Initial conditions

An ingenious choice of the initial state increases the convergence rate and hence, reduces simulation time for a given variance. We can argue with Eq. (4.2) how an initial state close to the ground state reduces the number of iterations needed to reach

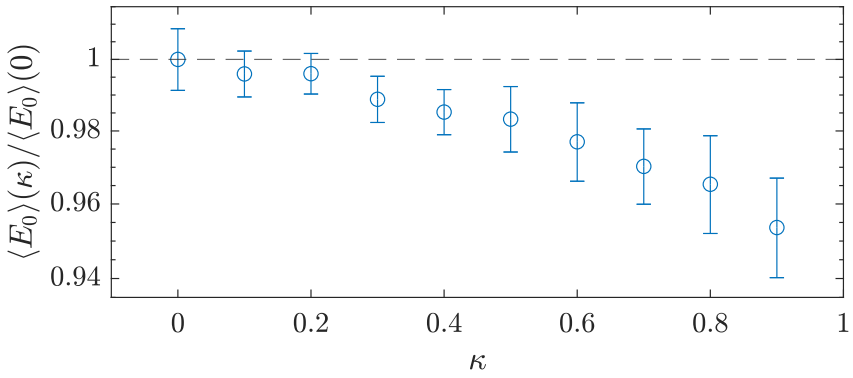

FIGURE 4.9: Estimations of the ground state energy $\langle E_0\rangle(\kappa)$ as a function of the importance sampling spring constant κ for the $L = 8$ Fermi-Hubbard ring with $t = 1$, $U = 20$, and $r = 64$. Each point was estimated over $3 \cdot 10^4$ iterations, and the population was about $1.5 \cdot 10^5$ triplets with $r = 30$. The error bars represent the statistical errors computed over 30 independent simulations.

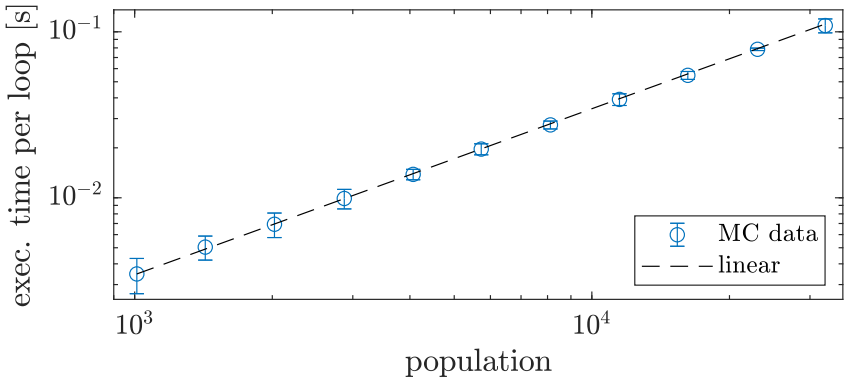

FIGURE 4.10: Example of the algorithmic complexity for the $L = 8$ Fermi-Hubbard ring with $t = 1$, $U = 20$, and $r = 64$. The complexity is linear as the main part of the simulation is spent on generating the spawnings. The errors were computed over 600 loops.

the fixed point. The standard choices include the infinite temperature density matrix

$$\rho_0 \sim 1, \tag{4.29}$$

and the N_{GS} degenerate free ground states $\{|E_0^{\text{free}(k)}\rangle\}_k$,

$$\rho_0 = \frac{1}{N_{GS}} \sum_{k=1}^{N_{GS}} |E_0^{\text{free}(k)}\rangle\langle E_0^{\text{free}(k)}|. \tag{4.30}$$

Figures 4.11 & 4.12 compare the convergence rate between the two standard initial conditions for the square 4×4 XXZ Heisenberg model. In the small interaction case $J^{xy} = 0.5$, the convergence is much faster when starting from the free ground state, whereas for medium interaction strengths $J^{xy} = 1$, the distinction is not clear. As expected in the regime $J^z \sim J^{xy}$, the interacting ground state is mainly composed of off-diagonal triplets, as opposed to the perturbative regime for which the interacting ground state is the free ground state with a small perturbation. These results illustrate the efficiency of the method in the perturbative regime.

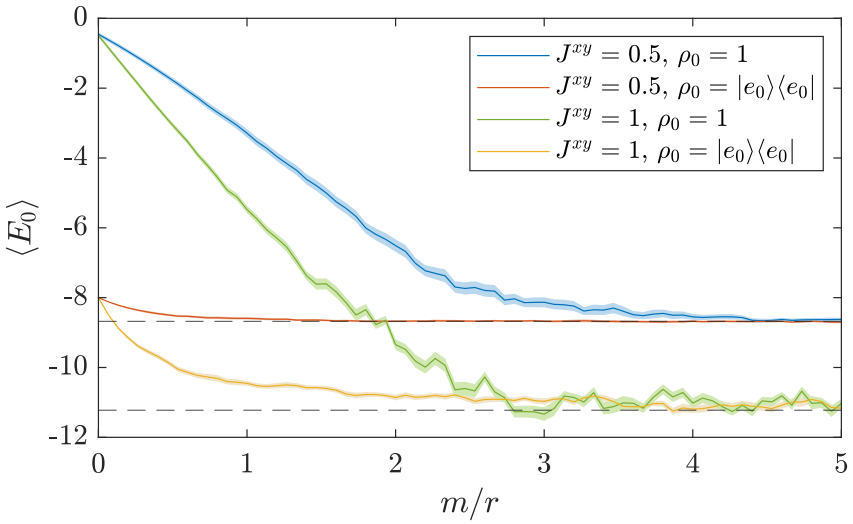

FIGURE 4.11: Estimate of the ground state energy $\langle E_0 \rangle$ for the square 4×4 XXZ Heisenberg model with $J^z = 1$, various interaction strengths J^{xy}, $r = 15$, and the two initial conditions described by Eqs. (4.29) & (4.30). The errors were computed over 30 independent simulations for a final population of $5 \cdot 10^5$.

4.4.2 ERROR ESTIMATION

The statistical errors of the measurements can be estimated by performing a block-analysis on a single long chain of correlated estimations A_m whose average value is the mean value of the observable $\langle A \rangle$. The method considers a single simulation composed of a convergence from the initial to the ground state involving N_{conv} steps and subsequent sampling by a further application of the main loop to construct a chain of N_{samp} estimates. Since the estimates are correlated, they have to be block-analyzed to extract the correct statistical error. A naive calculation of the standard deviation from the correlated data will tend to underestimate the correct statistical error. Starting from the original data series $A_m^{(0)} = A_m$, we iteratively create blocked series by averaging over two elements of the previous iteration. The elements of the iteration l are constructed via the equation

$$A_m^{(l)} = \frac{1}{2}\left(A_{2m-1}^{(l-1)} + A_{2m}^{(l-1)}\right), \tag{4.31}$$

with $m = 1, \ldots, N_{\text{samp}}/2^l$. The mean remains unchanged and the new averaged blocks are less correlated than the previous ones. The statistical error is estimated by the standard error for the uncorrelated results,

$$\sigma_A^{(l)} = \sqrt{\frac{\text{Var}(A^{(l)})}{N_b^{(l)}}}, \tag{4.32}$$

where $N_b^{(l)}$ is the number of blocks at iteration l and $\text{Var}(A^{(l)})$ is the variance of the blocked data at iteration l. This estimated error increases as a function of the block size and converges to the correct one when the blocks become uncorrelated

$$\sigma_A = \lim_{l \to \infty} \sigma_A^{(l)}. \tag{4.33}$$

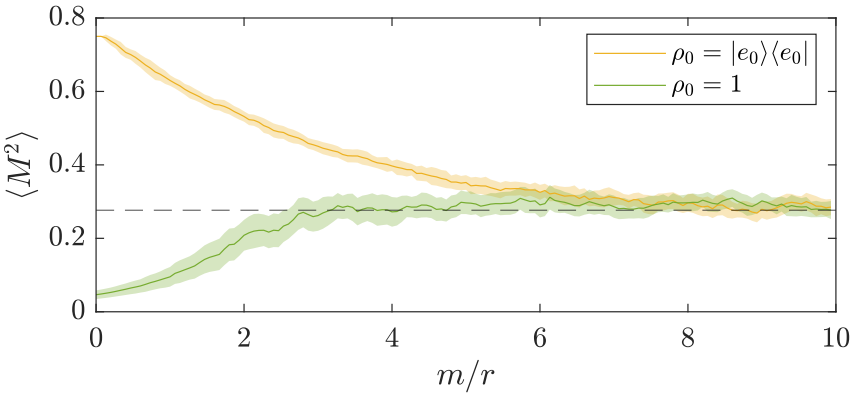

FIGURE 4.12: Estimate of the squared staggered magnetization $\langle M^2 \rangle$ for the square 4×4 XXZ Heisenberg model with $J^z = J^{xy} = 1$, $r = 15$, and the two initial conditions described by Eqs. (4.29) & (4.30). The errors were computed over 30 independent simulations for a final population of $5 \cdot 10^5$.

To ensure that the error is estimated by a large sample, we require the number of blocks to be larger than 30. Figure 4.13 displays the estimation of the square magnetization $\langle M^2 \rangle$ for the 4×4 Heisenberg model with $J = 1$, $r = 15$ and $\kappa = 1/10$ as a function of the population. The estimations were computed in each case with a

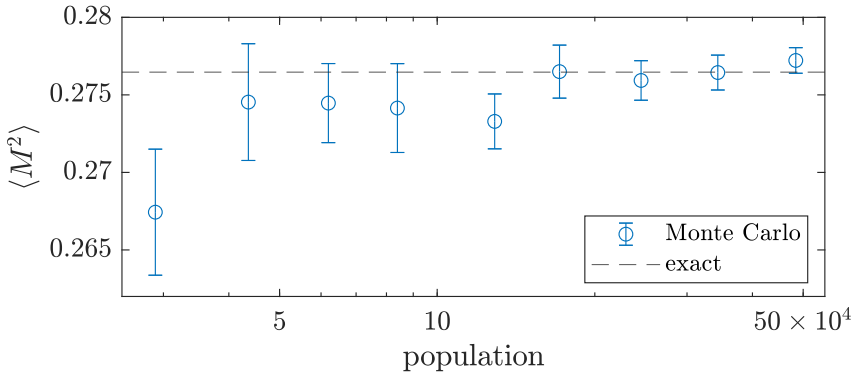

FIGURE 4.13: Estimations of the squared staggered magnetization $\langle M^2 \rangle$ for the square 4×4 Heisenberg model with $J^{xy} = J^z = 1$. The errors were estimated with a block analysis of $1.5 \cdot 10^4$ samples.

block analysis of a single chain of $1.5 \cdot 10^4$ samples.

The main competitor to our approach is the celebrated DMQMC technique [35], which calculates the solution of the Bloch equation for any inverse temperature β. The ground state corresponds to the low-temperature limit, i.e. $\beta \to \infty$, which is estimated by a long chain of correlated samples as described above. Unlike DMQMC, our technique only allows access to the ground state since the solution for the whole β range involves solving the nonlinearities introduced to preserve the norm (see Sec. 3.2). However, obtaining the ground state is faster for two reasons; the evolution step $1/r$ has no clear upper bound and the freedom in the initial state improves the convergence. For example, the choice of the initial state as the free ground state can be compared to an interaction picture, where the free part is integrated exactly and the dynamics is only in the interaction. The benefit of the interaction picture approach is illustrated in Fig. 4.11, where in the case of a perturbative regime, the simulation converges much faster. We note the efforts provided to construct an interaction

picture with DMQMC in [55]. Concerning the absence of clear an upper bound on the evolution step, an informal demonstration can be performed from the equation $\left(1+\frac{\mathcal{L}}{r}\right)^m \rho_\infty = \rho_\infty$. For an initial density matrix $\rho_0 = \sum_{ij} c_{ij}(m=0)|E_i\rangle\langle E_j|$, one can estimate that the inverse evolution step must be larger than the pair of state in the initial ensemble (i,j) that maximizes the quantity $(E_i+E_j)/2$. Concretely, we found the following bound,

$$\max\left\{\frac{|E_i+E_j|}{2}\right\}_{(i,j)\in\rho_0} \lesssim r. \tag{4.34}$$

We now argue why a large evolution step $1/r$ reduces the statistical error of the final result. Once the simulation has converged, an iterative application of the main loop produces the sequence of correlated data points. This correlated trajectory is characterized by two parameters, the decorrelation time τ, related to the number of iterations over the main loop N_{dec} between two decorrelated points via $N_{\text{dec}} = \tau r$ and the amplitude of the fluctuations around the average δA. Our simulations showed that the amplitude of those large-scale fluctuations is independent of r and can only be reduced by increasing the population. The variance can be written as a combination of the two parameters as $\sigma^2 \sim A^2 N_{\text{dec}} \sim r$, hence specifying its dependence on r. For a constant number of data points, we increase the number of independent samples by lowering the parameter r, hence decreasing the variance. Figure 4.14 illustrates this behavior with the variance of the ground state energy σ_E^2 for the 1×10 Fermi-Hubbard ring at half-filling. Various interaction strengths were considered, and importance sampling was not used, i.e. $\kappa = 0$. The error bars were estimated with 10 independent simulations, each with the same number iteration $m = 3.2\cdot 10^4$ and the same population 10^5. The corresponding DMQMC lower bound $(E_{\max}-E_{\min})/2$ is illustrated by the dotted lines. The linear unit slope

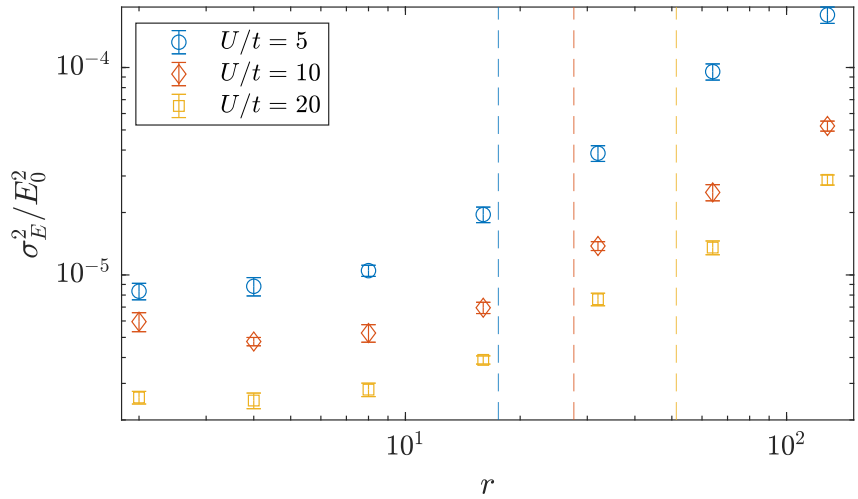

FIGURE 4.14: Decorrelated relative variance of the ground state energy for the 1×10 Fermi-Hubbard ring at half-filling as a function of the inverse evolution step r. The vertical dotted lines correspond to the lower bounds dictated by the DMQMC approach.

is visible on the right-hand side of the figure while the transition to the minimum value occurs when the decorrelation time approaches unity, i. e. when each data point is uncorrelated from the previous ones. Further reducing r only increases the jump amplitude, resulting in an increasing error on the left-hand side of the figure. This

feature highlights once more the efficiency of the algorithm in a perturbative regime where $H^{\text{free}} \gg H^{\text{int}}$ ($U \gg t$).

4.4.3 PARALLELISM

Parallel computing provides a tool to distribute the computational load of a simulation over multiple logical processors, called threads, in order to reduce the execution time. Distributing the load allows for independent calculations to be performed simultaneously by having two types of memory structure. The shared memory is common to all the threads whereas the distributed memory is associated to a single thread. The challenges of parallel computing consist in an adequate load balancing between the threads, memory synchronization, and overhead for communication between the parallel parts. Figure 4.15 sketches the parallel implementation of an arbitrary program where parallel regions are separated by serial executions of the program. The length of these serial parts, or the overhead, is responsible for an upper limit in the speedup of a program because shared memory has to be used for communication and synchronization.

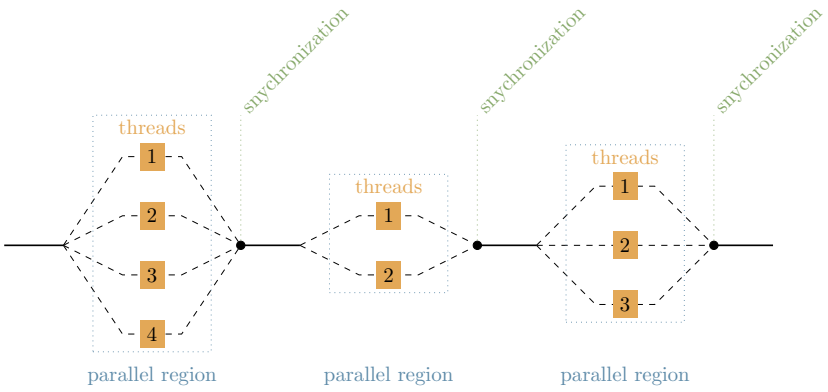

FIGURE 4.15: Sketched execution of the parallel implementation of a program. The parallel regions end with the memory synchronization and are interspersed with serial parts.

The instabilities associated to the sign problem require a typical population plateau usually characterized by a very large number of triplets. In order to evolve these very large populations, we parallelize the algorithm, which results in a significant computational speedup. The high parallelism of the triplet unraveling algorithm resides in the fact that most of the execution time is spent on the spawning step. Because these spawnings are independent of one another, they can be distributed among multiple computer processes and performed simultaneously. Only the compressions require synchronization and communication between these processes[1].

Parallel program flow The flow of this parallel program is illustrated in Fig. 4.16. Because each spawning is independent, we can distribute the total weight among the threads such that each thread has approximately the same number of spawnings to perform. The sorted triplet ensemble is separated into domains, whose

[1] We implemented the algorithm using C++ and designed it with modules to incorporate a parallel implementation easily. The results in this dissertation were performed either on multicore personal computers or on small computational clusters for the larger simulations. We developed a shared-memory multiprocessing code using an OpenMP [87] interface that is well suited for C++ and controls the load distribution efficiently.

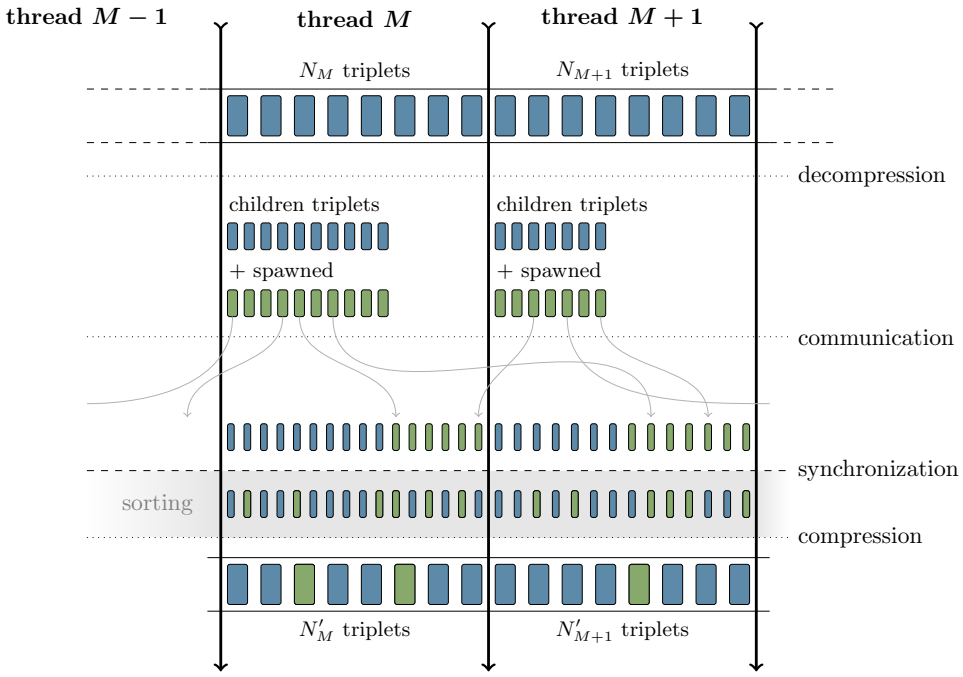

FIGURE 4.16: Flowchart of the parallel implementation of a single main loop. The triplet ensemble is distributed between the threads, where the triplets are illustrated by the blue rectangles. The decompression and the spawning are performed in the distributed memories. The synchronization ensures that all the spawned triplets have been communicated to their correct thread. The sorting, the compression, the free evolution, and the computation of observables can then be performed in parallel.

borders are stored in the shared memory. Conversely, the newly spawned triplets are stored in the distributed memory of the threads. The threads then have to communicate and synchronize their memory in order to perform the compressions. Because the borders between the thread domains are shared, each thread spawns and calculates where the new triplet has to be subsequently sent. The procedure minimizes communication because most of the triplets are spawned on the correct thread and do not need to be communicated. Before the compression, the threads have to wait until all the spawnings are performed and the triplets sent to the correct thread. Then, the compressions can be performed independently by sorting the triplets locally and merging them with the existing ones because they are all in their designated thread. The free contribution, the measurements, and the collection of the ensemble statistics do not produce any jump, implying that they are performed purely in parallel. The measurement and the computation of the population are performed in parallel once $\mathcal{R}_s^{\text{free}}$ is applied and subsequently the shift is updated.

The synchronization is the bottleneck of this parallel implementation. Because the program has to wait until all the triplets have been sent to the designated thread, it is important to have a precise load balance. If all the threads have exactly the same number of spawnings, no waiting is required and the total execution time is reduced. This load balancing is translated into a careful choice of the borders between each thread domain. Since the number of spawning events is proportional to the weight, the adequate load balancing is found for an equal distribution of the weight between the threads. In that way, all the threads arrive simultaneously at the synchronization

barrier and no time is lost waiting for slower threads.

Speed-up To measure quantitatively how the parallel implementation affects the execution time, we define the computational speed-up as a number indicating the relative performance of two processes solving the same task. Here, we introduce it as the ratio between the execution time for a given number of threads and the execution time for a single thread. The speed-up is illustrated in Fig. 4.17 for the 4×4 Heisenberg model with $J^z = J^{xy} = 1$, $r = 15$, $\kappa = 1/10$, $S_0 = -9$, and a shift update enabled at $m/r = 1$. The errors were estimated over 10 independent simulations. The increasing populations between the curves correspond to initial weights of 50, 500, and 5000, respectively. These results were performed on a small computational cluster

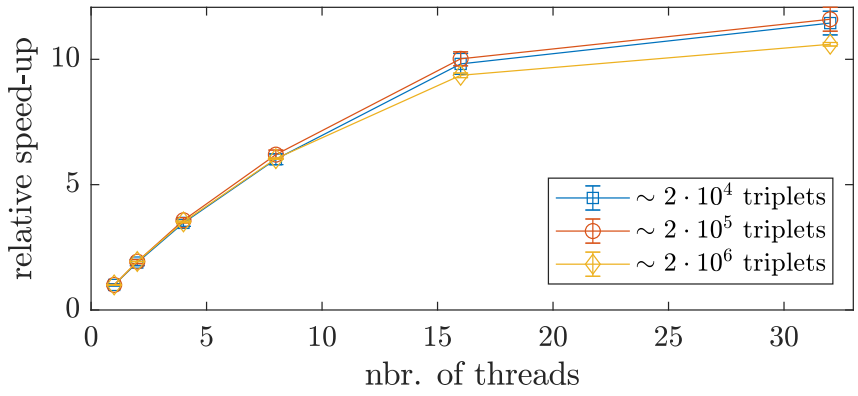

FIGURE 4.17: Computational speed-up as a function of the number of threads for the 4×4 Heisenberg model.

with only 32 threads available. The slowing down of the speed-up for a large number of threads might be influenced by the limited number of processors in the cluster causing some over-threading.

4.5 CONCRETE CALCULATIONS AND EXAMPLES

In order to demonstrate the effectiveness and the versatility of the fixed-point quantum Monte Carlo method, we illustrate some ground-state calculations for various models, observables, and interaction strengths. We consider the paradigmatic models defined earlier, namely the square Heisenberg model (4.5), the square Fermi-Hubbard model (4.15), and the Fermi-Hubbard ring. We choose lattices big enough so that the exact ground cannot be naively stored in the computer. These lattices are 6×6 for the square Heisenberg, 4×4 for the Fermi-Hubbard at half-filling, and 1×20 for the Fermi-Hubbard ring for which the density matrix has respectively $8.2 \cdot 10^{19}$, $2.7 \cdot 10^{16}$, and $1.2 \cdot 10^{21}$ elements. We simulated ground-state properties on a standard modern laptop or a small computational cluster for a population of the order 10^6-10^7 triplets.

Our first example considers the squared staggered magnetization of the ground state of the 6×6 square Heisenberg model described by the Hamiltonian (4.5). Figure 4.18 shows the convergence to the ground state squared staggered magnetization for the 6×6 Heisenberg model with $r = 30$ and $\kappa = 1/6$. The initial population is $2 \cdot 10^3$ triplets with initial shift $S_0 = -19$ and an update enabled at $m/r = 3$, which produced an end population of $5.7 \cdot 10^6$ triplets. We did not use the initiator approximation and the errors were calculated over 100 independent simulations. These

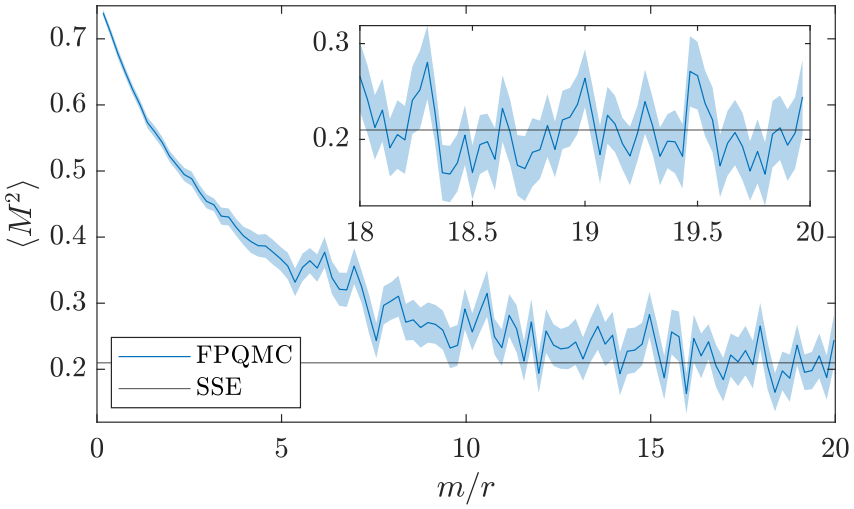

Figure 4.18: Estimate of the squared staggered magnetization $\langle M^2 \rangle$ for the 6×6 Heisenberg model with $r = 30$, $\kappa = 1/6$, and an initial population of $1.6 \cdot 10^3$ triplets. The initial shift was $S_0 = -19$ with the update enabled at $m/r = 3$, which produced an end population of $5.7 \cdot 10^6$ triplets. The reference solution was obtained in [73] via a stochastic series expansion (SSE). Note that in the main plot, one every 6 iterations is plotted.

Monte Carlo results are in agreement with the stochastic series expansion method introduced in [73].

Following the structure of [88], we study the convergence of the ground state energy in the 4×4 Fermi-Hubbard model for the regime $t = 1$, $U = 40$. Remember that within our method, the free Hamiltonian represents the Coulomb potential and the interacting Hamiltonian the kinetic energy. Depending on which representation basis we use, position or momentum, we can study the limit of weak and strong Coulomb interaction. The intermediate regime is the more challenging regime where both expressions of the Hamiltonian, in the space domain or in the momentum domain, are the hardest to solve. The number of matrix elements depends not only on the size of the system but on the number of electrons on the lattice. This number is maximized at half-filling, that is when the number of electrons is exactly equal to the number of sites. The ground state is found for a linear combination of lattice configurations with an equal number of spin up and spin down electrons. Figure 4.19 shows the convergence to the ground-state energy for the 4×4 Fermi-Hubbard model with $t = 1$, $U = 40$ at half-filling. We set $r = 4$, $\kappa = 1/40$, and $c_{\text{init}} = 1.8$ for an initial population of $3 \cdot 10^6$ triplets with constant shift $S_0 = -1.3$. The final population is about $1.1 \cdot 10^7$ triplets. The errors were calculated over 30 independent simulations. At half-filling the Hubbard model does not suffer from the sign problem, hence the initiator approximation and the importance sampling are not necessary to obtain convergent results. Though, they still drastically reduce the number of triplets needed in the simulation.

Finally, the largest system we consider is the 1×20 Fermi-Hubbard ring with various interaction strengths at half-filling. We compute the momentum distribution $n(k)$ of the ground state that is defined for a $1 \times L$ lattice by

$$n(k) = 1 - \frac{1}{2L} \sum_{\nu,\mu,\sigma} e^{ik(\mu-\nu)} \langle b_\mu^\sigma b_\nu^{\sigma\dagger} \rangle, \tag{4.35}$$

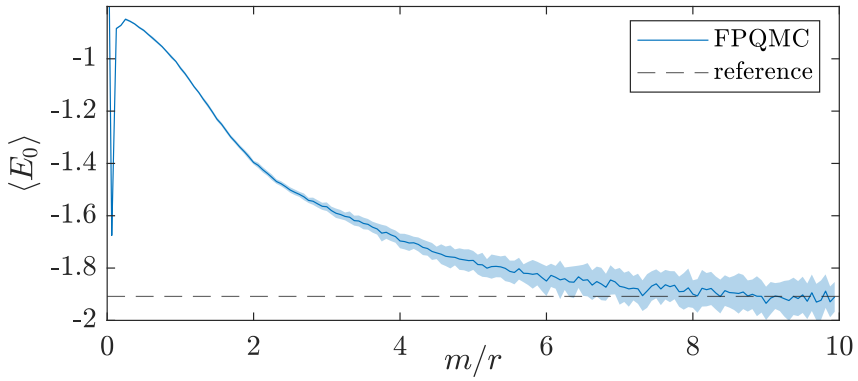

FIGURE 4.19: Estimate of the ground state energy $\langle E_0 \rangle$ for the 4×4 Fermi-Hubbard model at half-filling with $t = 1$, $U = 40$. The parameters were $r = 4$, $\kappa = 1/40$, and $c_{\text{init}} = 1.8$ for an initial population of $3 \cdot 10^6$ triplets with constant shift $S_0 = -1.3$. The final population was about $1.1 \cdot 10^7$ triplets. The reference energy was taken from Ref. [89].

where ν, μ are the lattice sites, and k is the one-dimensional momentum of the reciprocal lattice. Figure 4.20 shows the momentum distribution $n(k)$ of the ground state for the 1×20 Fermi-Hubbard ring at half-filling with $r = 30$, $\kappa = 1/6$. The initial population is 10^4 triplets with initial shift $S_0 = -14$, an update that started at $m/r = 2$. The final population is about $1.2 \cdot 10^6$ triplets. The errors were estimated over 30 independent simulations. In the limit $U/t = 0$, the distribution coincides

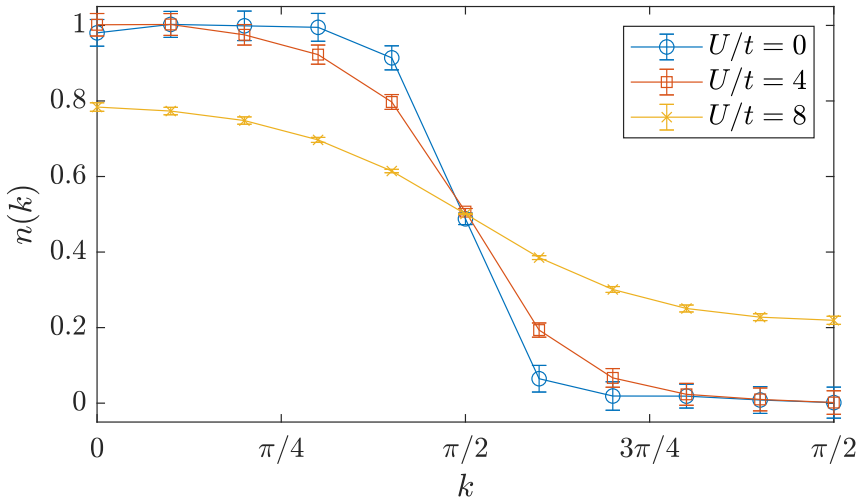

FIGURE 4.20: Momentum distribution $n(k)$ of the ground state for the $L = 20$ Fermi-Hubbard ring with various interaction strengths.

with the Fermi-Dirac distribution for a free fermionic gas. As expected, increasing the Coulomb potential smears the sharp Fermi-Dirac distribution. Even though the density matrix is larger than for the previous examples, we can simulate at smaller U. The reason lies in the fact that the Hilbert space exploration is more easily controllable via the spring constant because of the nearest-neighbor interaction.

As a concluding remark, we want to emphasize the power of unraveling in representing statistically the system, which is illustrated by the multiple orders of magnitude of difference between the population and the number of matrix elements. We

were able to simulate the largest systems in the limit of weak interaction because our method is most effective when the interaction strength is not too large.

5 Real-time dynamics

The Monte Carlo method presented in the previous chapter was developed for steady-state calculations and based on a fixed-point iteration scheme. In this chapter, we study how to extend this methodology to simulate the reversible dynamics described by the von Neumann equation. This is motivated, first, by recent experiments in quantum systems out of equilibrium [90–93] that have revealed the need to develop real-time simulation methods that reproduce these dynamical experiments. Second, concerning the original motivation about fundamental particles, this study gives access to benchmark models to test the performance of the algorithm in the challenging context of reversible dynamics. Because it is the dissipative mechanism that drives the system towards equilibrium, we expect reversible dynamics to be harder to solve for large times due to the competing fast oscillating exponentials.

Similarly to the fixed-point iteration scheme, we assume the separation of the Hamiltonian (3.7) and use the triplet unraveling framework to sample stochastic trajectories in a certain configuration space representing the Hilbert space. The triplets undergo alternately continuous deterministic evolution and random jumps. The algorithm, based on the magical formula (2.36), has the same main structure, namely a main loop which is iteratively applied to an ensemble of stochastic trajectories. In order to cope with the large size of the configuration space, we need the free eigenbasis as the discrete basis and the superselection rule. Similarly to all other stochastic techniques for reversible quantum systems, the sign problem limits the computation of long-time properties of the system. Our Laplace framework coupled with unraveling allows us to introduce the *deadweight approximation* which reduces the severity of the sign problem by damping the fast oscillating exponentials. Additionally, the importance sampling procedure introduced in the previous chapter based on the dynamic norm helps to reduce the population needed to converge massively.

This chapter is structured in the same way as the previous one. First, we recall the basic equations to describe the algorithm and provide a short overview of a few other stochastic methods that are able to solve purely reversible dynamics in multi-dimensional systems. Then, we introduce the dynamical algorithm in details and make some remarks on its efficiency. In a third section, we discuss population control and introduce the deadweight approximation. In section four, we examine the numerical methods to invert the Laplace transform and conclude that in most cases, we can simply extract the dynamical properties directly in the Laplace domain. Finally, we illustrate how to extract these dynamical properties and control the population.

5.1 THE MAGICAL FORMULA

We start by reviewing the triplet unraveling from Sec. 3.1 in order to reproduce the solution of the von Neumann equation (3.8) describing purely reversible dynamics. We use the splitting of the Hamiltonian introduced earlier,

$$H = H^{\text{free}} + H^{\text{int}}, \tag{5.1}$$

where we recall that H^{free} is the part of the Hamiltonian that can be solved exactly. Note that in a general setting, this choice is not unique. As we saw previously, the method is most effective for small interactions, hence, the choice of the basis influences the accuracy of the result (see Sec. 5.5). The unraveling reproduces the application of the magical formula (2.36), by considering the evolution of triplets $(c_m, |\Phi_m\rangle, |\Psi_m\rangle)$, where c_m is complex and $|\Phi_m\rangle$, $|\Psi_m\rangle$ are piecewise deterministic stochastic processes. This evolution occurs according to a formal iteration order $m = 0, 1, \ldots$ with the fundamental propagator

$$T_{r,s} = r\left[\mathcal{R}^{\text{free}}_{s+r}\left(1 + \frac{\mathcal{L}^{\text{int}}}{r}\right)\right]. \tag{5.2}$$

The stochastic processes undergo continuous evolution associated to $r\mathcal{R}^{\text{free}}_{s+r}$ and interspersed with random jumps accounting for $(1 + \frac{\mathcal{L}^{\text{int}}}{r})$. A large number of such iterations $M^{\text{trunc}} \to \infty$ (see Chap. 3) eventually satisfies

$$\tilde{\rho}_s = s\sum_{m=0}^{\infty} \mathbb{E}[c_m|\Phi_m\rangle\langle\Psi_m|], \tag{5.3}$$

where $\tilde{\rho}_s$ is the density matrix in the Laplace domain defined by

$$\tilde{\rho}_s = s\mathcal{R}_s\rho_0, \tag{5.4}$$

with ρ_0 an initial state. Once the density matrix has been estimated, we can calculate correlation functions C_s^{AB}, which usually take the form

$$C_s^{AB} = \text{tr}(AB\tilde{\rho}_s), \tag{5.5}$$

where A, B are self-adjoint operators.

5.1.1 REVERSIBLE DYNAMICS: A SHORT OVERVIEW

Recent experiments in quantum systems out of equilibrium [90–97] have revealed the need to develop real-time simulation methods. Due to the exponential growth of the Hilbert space with the system size, only a few simulation techniques are available, which are usually restricted to specific dimensions or use some approximations. In one-dimensional systems, the most common tool to provide dynamical results is the time-dependent density matrix renormalization group (tDMRG) method [98–100]. Due to a matrix product state representation of the ground state, this method controls the size of the Hilbert space by keeping track of only a restricted number of degrees of freedom. This method has established itself as a reliable tool for real-time simulations in one-dimensional lattice systems. For higher dimensions, some computational methods rely on simulating an approximation of the original model to effectively reduce the size of the Hilbert space [101–103]. Nonequilibrium dynamical mean-field theory [101, 104] now is the standard technique with multiple successful

applications [105–109]. Other methods have proven their reputation with notable success in quantum chemistry, such as those based on a Hartree–Fock approximation [102, 110] or density functional theory [103].

Another way to cope with the growing size of the Hilbert space is to use stochastic methods to sample stochastic trajectories in a configuration space. Although quantum Monte Carlo (QMC) methods were originally formulated to study ground state and equilibrium properties, dynamical adaptations have also been put forward. These are based on a stochastic sampling of diagrammatic expansions of many-body Green's functions defined along a Keldysh contour [4, 13, 111]. All these methods, however, have been limited in accessing long-time behavior by the well-known dynamical sign problem. Notable exceptions are the inchworm algorithm presented in [15] and real-time full configuration interaction QMC algorithm [3]. The first technique can access medium-to-long-time $t \lesssim 10$ dynamical properties, due to corrections of short-time diagrams, whereas the second can allow for simulation times up to $t \lesssim 40$, although at the expense of probability conservation.

5.1.2 PARADIGMATIC MODELS

To test the performance of our dynamical triplet unraveling, we consider three models; the one-dimensional XXZ Heisenberg model, the quantum Ising chain, and the two-dimensional transverse Ising model. A phase transition in the first model between diffusive and ballistic propagation of excitations allows us to test the ability of the method to recognize the two regimes. With the second model, we aim at measuring confinement of spins of opposite signs that can be observed under specific conditions. In this context, we will show how to extract the dynamical properties in such a confined system. The confinement mechanism is strongly motivated by the more challenging case of quark confinement in QCD. Because our method is a stochastic method, we are not bound by the system's dimension, and illustrate some examples with two-dimensional lattices of the last model.

The one-dimensional XXZ model Our first model of interest is the XXZ Heisenberg chain with open boundary conditions. Concretely, the model describes spin-1/2 particles on a lattice of length L whose Hamiltonian is given by

$$H = \sum_{\mu=1}^{L-1} J^x \sigma_\mu^x \sigma_{\mu+1}^x + J^y \sigma_\mu^y \sigma_{\mu+1}^y + J^z \sigma_\mu^z \sigma_{\mu+1}^z, \tag{5.6}$$

where σ^x, σ^z are the standard Pauli matrices and the sum runs over the spins in the chain. For this one-dimensional chain, we choose the basis of the Hilbert as a tensor product of the eigenstates of the σ^z operators, that is

$$|e_{s_1,\dots,s_L}\rangle = |s_1\rangle \otimes |s_2\rangle \otimes \cdots \otimes |s_L\rangle, \tag{5.7}$$

where $s_\mu = s_\mu^z = \pm 1$ are the eigenvalues of the operator σ_μ^z on lattice site μ. The single-particle operators σ^z and $\sigma^\pm$ act upon the basis states according to the standard algebra of Pauli matrices

$$\sigma^z|\pm 1\rangle = \pm|\pm 1\rangle, \qquad \sigma^\pm|\mp 1\rangle = |\pm 1\rangle, \qquad \sigma^\pm|\pm 1\rangle = 0. \tag{5.8}$$

The choice of the basis sets the following splitting of the Hamiltonian into a free and an interacting part, $H = H^{\text{free}} + H^{\text{int}}$, as follows

$$H^{\text{free}} = J^z \sum_{\mu=1}^{L-1} \sigma_\mu^z \sigma_{\mu+1}^z, \qquad H^{\text{int}} = J^{xy} \sum_{\mu}^{L-1} \sigma_\mu^+ \sigma_{\mu+1}^- + \sigma_\mu^- \sigma_{\mu+1}^+, \tag{5.9}$$

with $\sigma_\mu^\pm = (\sigma_\mu^x \pm i\sigma_\mu^y)/2$ and where we imposed $J^x = J^y = J^{xy}/2$. The Hamiltonian of an open one-dimensional chain conserves the total spin, thus, the number of allowed lattice configurations depends on the initial state. Unless stated otherwise, for one-dimensional systems, we consider the initial state

$$\rho_{\text{ini}} = |\text{ini}\rangle\langle\text{ini}|, \tag{5.10}$$

with

$$|\text{ini}\rangle = \bigotimes_{\mu=1}^{L/2} |+1\rangle_\mu \bigotimes_{\mu=L/2+1}^{L} |-1\rangle_\mu. \tag{5.11}$$

If the state (5.10) is considered, the number of configurations is maximized, that is

$$\#\text{ lattice config.} \sim \binom{L}{L/2}. \tag{5.12}$$

This initial state is introduced to study the dynamical behavior of spin excitations following an instantaneous quench. For $J^z < J^{xy}$, these excitations travel across the chain ballistically, whereas for $J^z > J^{xy}$, propagation is slowed down by the strong J^z field. The transition between the two regimes can be examined by considering the s-evolution of the magnetization profile given by the correlation function

$$C_s^{\sigma_\mu^z} = \text{tr}(\sigma_\mu^z \tilde{\rho}_s) \equiv \langle \sigma_\mu^z \rangle_s. \tag{5.13}$$

The quantum Ising chain A ferromagnetic quantum Ising chain of length L coupled to the transverse h^x and longitudinal h^z magnetic fields displays confinement of pairs of spin with opposite signs. Confining interactions have the peculiar property that two opposite charges are connected by a flux tube, or string, whose energy increases linearly with separation [112]. Beyond a critical separation, the string can break, creating new particle-antiparticle pairs. This breaking is energetically more favorable because the energy in the string is equal to the mass of the particle pair. This mechanism is known as string breaking and is the topic of many recent studies [113–115]. The Hamiltonian of such a system is described by

$$H = -J \sum_{\mu=1}^{L-1} \sigma_\mu^z \sigma_{\mu+1}^z - h^z \sum_{\mu=1}^{L} \sigma_\mu^z - h^x \sum_{\mu=1}^{L} \sigma_\mu^x, \tag{5.14}$$

where σ^x, σ^z are the standard Pauli matrices and the sum runs over the spins in the chain. To study the confinement, we choose the same basis as for the XXZ Heisenberg chain, that is (5.7). This implies the following splitting of the Hamiltonian into a free part H^{free} that is exactly solvable and an interacting part H^{int},

$$H^{\text{free}} = -J \sum_{\mu=1}^{L-1} \sigma_\mu^z \sigma_{\mu+1}^z - h^z \sum_{\mu=1}^{L} \sigma_\mu^z, \qquad H^{\text{int}} = -h^x \sum_{\mu=1}^{L} \sigma_\mu^+ + \sigma_\mu^-, \tag{5.15}$$

with $\sigma_\mu^x = \sigma_\mu^+ + \sigma_\mu^-$. This model has two phases with an ordered one for $J > h^x$ and the transition occurring at $J = h^x$. In the ordered phase, the ground state is degenerate due to a spin symmetry breaking. These degenerate ground states correspond to domain walls of various lengths, which are maximized for $h^x = h^z = 0$. In this limit, the ground state is twofold degenerate $|\psi_\mathrm{u} = \bigotimes_{\mu=1}^{L} |\uparrow\rangle_\mu$ and $|\psi_\mathrm{d}\rangle = \bigotimes_{\mu=1}^{L} |\downarrow\rangle_\mu$. If we enable the longitudinal magnetic field h^z, an energy gap is created between the two ground states, due to an increase of energy of the state with the spins aligned with the magnetic field.

As opposed to the Heisenberg Hamiltonian, the total spin is not conserved during the evolution, due to the spin-flip operators in the interacting Ising Hamiltonian. The allowed lattice configurations is hence not restricted to a constant number of spin up or down, which implies that the number of these configurations given by

$$\#\text{ lattice config.} = 2^L. \tag{5.16}$$

Two-dimensional Ising model In the presence of a transverse field h^x, the Hamiltonian of a two-dimensional Ising model of size $L \times L$ reads

$$H = -J \sum_{\langle \mu,\nu \rangle} \sigma_\mu^z \sigma_\nu^z - h^x \sum_{\mu=1}^{L^2} \sigma_\mu^x, \tag{5.17}$$

where $\langle \mu, \nu \rangle$ denotes the sum over the nearest neighbors. Similarly to the one-dimensional counterpart, this model displays a quantum phase transition from a ferromagnetic to a paramagnetic state with the critical field value being $h^x = h_c = 3.044J$ [116]. Here, we are mainly interested in the average transverse magnetization

$$X = \frac{1}{L^2} \sum_\mu \sigma_\mu^x. \tag{5.18}$$

As with many Hamiltonians we encountered, the choice of the basis is neither unique nor obvious. One choice would be the same as above,

$$|e_{s_1^z,\ldots,s_{L^2}^z}\rangle = |s_1^z\rangle \otimes |s_2^z\rangle \otimes \cdots \otimes |s_{L^2}^z\rangle, \tag{5.19}$$

where $s_\mu^z = \pm 1$ are the eigenvalues of the operator σ_μ^z on lattice site μ. The interacting Hamiltonian should be written then with the help of the relations $\sigma^x = \sigma^+ + \sigma^-$. The other choice is to use the σ^x eigenbasis,

$$|e_{s_1^x,\ldots,s_{L^2}^x}\rangle = |s_1^x\rangle \otimes |s_2^x\rangle \otimes \cdots \otimes |s_{L^2}^x\rangle, \tag{5.20}$$

where $s_\mu^x = \pm 1$ are the eigenvalues of the operator σ_μ^x on lattice site μ and to use $\sigma^z = \sigma^+ + \sigma^-$. Because the algorithm is the most effective in the weak coupling regime, the choice of the basis, the basis in σ^z or σ^x, makes simulations easier for the regimes $J \gg h^x$ or $J \ll h^x$, respectively. The efficiency of a basis choice depends also on the number of terms in the interacting Hamiltonian due to the stochastic application of the interaction. If the Hamiltonian has a lot of terms, more samples are needed to estimate the averages, and the simulations take longer. The first basis has L^2 terms, whereas in the second basis, contains $2L^2$ terms, however, the number of lattice configurations is twice as low, that is

$$\#\text{ lattice config.} = 2^{L-1}. \tag{5.21}$$

More about this choice of basis can be found in Sec. 5.5.

5.2 The algorithm

Now that the basic theoretical ingredients have been introduced, we examine closely the algorithm reproducing the dynamics generated by the magical formula. After introducing the general structure, we explain all the steps and algorithmic features in details. In the second part, we make some remarks on how to improve the efficiency and discuss the parallelism and complexity of the method.

5.2.1 General strategy

Our algorithm is a dynamical variation of the fixed-point method introduced in Chap. 4, of which the overall algorithmic structure is preserved. This structure consists of a core part, called the main loop, which aims at reproducing the application of the propagator (3.1) and whose application is iterated on an ensemble of triplets until a stable solution emerges. Two distinct steps form the main loop, the *interaction* and the *free evolution*, representing the application of the super-operators $(1 + \frac{\mathcal{L}^{\text{int}}}{r})$ and $r\mathcal{R}^{\text{free}}_{s+r}$ respectively. In order to implement these two steps, the algorithm considers the evolution of an ensemble of triplets trajectories in the Hilbert space $\{(w_m^{(n)}, i_m^{(n)}, j_m^{(n)})\}_n$, where $w_m^{(n)}$ is the ensemble weight at iteration m (see Sec. 4.2.3) and $i \equiv |i\rangle$, $j \equiv |j\rangle$ are the eigenstates of the free Hamiltonian. Note that here the superscript n refers to the index in the triplet ensemble. Formally, these triplets are formed by particular realizations of the stochastic processes $|\Phi_m\rangle$, $|\Psi_m\rangle$ described in Sec. 3.1. During this evolution, the triplets repeatedly experience stochastic jumps at a rate r and continuous weight updates according to the free von Neumann equation. The jumps account for the interaction step, whereas the weight update corresponds to the solution of the free von Neumann equation. Due to the choice basis with which the triplets are expressed, this free contribution is exactly solvable. At iteration m, the m^{th} summand in the magical formula, $\tilde{\rho}_{m,s} = s\mathbb{E}[c_m|\Phi_m\rangle\langle\Psi_m|]$, is recovered in average by

$$\tilde{\rho}_{m,s} \approx s \sum_n b\ w_m^{(n)} |i_m^{(n)}\rangle\langle j_m^{(n)}|, \tag{5.22}$$

with b the importance sampling bias. In order to have an accurate measure of the number of random jumps, we introduce the triplet unit of weight w_u. We use these parameters to define, at iteration m, the *triplet population* P_m roughly as the total number of triplets with unit of weight w_u, i.e.

$$P_m = \sum_n \left\lceil \frac{|w_m^{(n)}|}{w_u} \right\rceil, \tag{5.23}$$

with $\lceil\cdot\rceil$ the ceiling function. As described below, the unit of weight w_u also fixes the initial triplet population of the statistical ensemble

Typically, correlation functions of the form of Eq. (5.5) are estimated by a procedure involving an initialization, an iteration on the main loop, and a computation of correlation functions. The initialization begins by setting the triplets ensemble to the initial state ρ_0, e.g. Eq. (5.10). The normalization of the density matrix with the parameter w_u uniquely defines the initial population. The initial triplets with weight w smaller in absolute value than w_u are rounded to $\text{sign}(w)w_u$ with probability $|w|/w_u$ or removed from the simulation. The initialization is then completed by

the application of a free evolution step to the initial density matrix ρ_0. The iteration on the main loop involves M^{trunc} applications of the interaction and free evolution steps, with the cutoff M^{trunc} being chosen prior to the simulation. At the end of each loop $m \leq M^{\text{trunc}}$, the following quantity is calculated and stored,

$$\text{tr}(AB\tilde{\rho}_{m,s}) \approx s \sum_n b\, w^{(n)} (AB)_{i^{(n)} j^{(n)}} \tag{5.24}$$

with $(AB)_{i^{(n)} j^{(n)}} = \langle i^{(n)}|AB|j^{(n)}\rangle$. Once the iteration over the main loop is finished, the correlation function C_s^{AB} is calculated by summing over the contribution from all loops, that is

$$C_s^{AB} = \sum_{m=1}^{M_{\text{trunc}}} \text{tr}(AB\tilde{\rho}_{m,s}). \tag{5.25}$$

To be coherent with the terminology of the previous chapter, we call this three-stage procedure an independent simulation. We need to perform multiple independent simulations to estimate the statistical errors.

Deadweight approximation The dynamical sign problem manifests itself at intermediate times as numerical instabilities due to the fast oscillating exponentials. To cope with the dynamical sign problem, we need to prevent statistically unimportant triplets to contribute to the evolution, an idea on which the *deadweight approximation* is based. To identify statistically irrelevant triplets, we introduce a threshold $u_{\text{dw}} > 0$ under which all triplets with a weight smaller in absolute value are not allowed to spawn. However, because the free evolution is performed exactly, it does not worsen the dynamical sign problem, hence all the triplets below the threshold are still allowed to evolve freely. The triplets under this threshold are called *inactive* as opposed to *active*. We can interpret these inactive triplets as an effective environment that is needed in order to ensure the ergodicity in the exploration of the Hilbert space.

Compression and decompression Prior to the execution of both the spawning step and the free evolution, we perform a modification of the ensemble to improve the statistics without influencing the statistical averages. A prespawning *decompression* splits each single triplet (w, i, j) into child triplets of triplets with weight w_u in absolute value $(\text{sign}(w)w_u, i, j)$ and a rest triplet with weight $w_r = \text{sgn}(w)(|w/w_u| - \lfloor |w/w_u| \rfloor)$ ($\lfloor\cdot\rfloor$ is the floor function). The rest triplet is removed from the simulation with probability $1 - |w_r|$ or its weight is updated to $\text{sign}(w)w_u$. A *compression* is applied on a decompressed ensemble and forms classes of triplets according to the pair (i, j). The representative of each class is then replaced by a single triplet with weight being the sum of all the weights in the class.

5.2.2 THE MAIN LOOP

We now discuss in detail the main loop of our algorithm introduced in [53] and depicted in Fig. 5.1. It evolves the ensemble of triplets $\{w_m^{(n)}, i_m^{(n)}, j_m^{(n)}\}_n$ from iteration m to $m+1$. To lighten the notation in this subsection, we don't print the subscript m. The loop is separated into two main steps, the spawnings reproducing the application of the superoperator $(1 + \frac{\mathcal{L}^{\text{int}}}{r})$ and the free evolution reproducing the $r\mathcal{R}_{s+r}^{\text{free}}$. Note that we included the use of the importance sampling procedure described in Sec. 4.2.3.

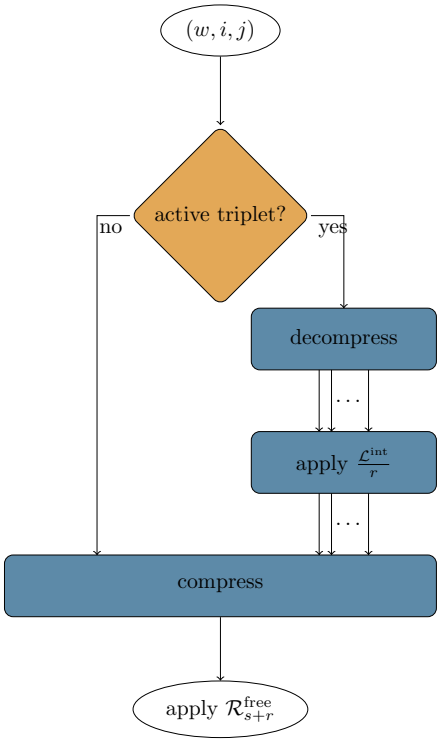

FIGURE 5.1: Flowchart of the dynamical triplet unraveling algorithm describing the application of the superoperator $\mathcal{L}^{\text{int}}/r$. The orange diamond represents the deadweight approximation.

Spawnings

1. Preparation to interaction.

   (a) Deactivation of unimportant triplets $(w^{(n)}, i^{(n)}, j^{(n)})$. If $|w^{(n)}| < u_{\text{dw}}$, the triplet becomes inactive. Inactive triplets do not experience any collision and therefore only evolve freely.

   (b) Prespawning decompression. The active triplets are split into $N_c = \lfloor |w^{(n)}|/w_u \rfloor$ child triplets with weight $w^{(n)}/N_c$.

2. Spawning. For each child triplet, a side is randomly chosen (quantum mechanically, either $i^{(n)}$ or $j^{(n)}$), and a new state k is selected with equal probability among the n_t possible spawning transitions. For instance, if $i^{(n)}$ is chosen, the following triplet is added to the ensemble

$$(i\frac{h^{\text{int}}_{i^{(n)}k}}{r}\frac{w^{(n)}}{N_c}2n_tT_b, k, j^{(n)}), \tag{5.26}$$

   where $T_b = e^{\kappa(n^2_{ij}-n^2_{kj})}$ is the transition bias, with n_{ij} the dynamic norm. If $j^{(n)}$ is selected, an equivalent triplet is spawned.

Free evolution

1. Full compression. A class containing all the triplets associated to a specific pair $(i^{(n)}, j^{(n)})$ is replaced by a single triplet whose weight is the sum of all the weights in the class.

2. Weight update. For each class $(w^{(n)}, i^{(n)}, j^{(n)})$, a weight update is performed, accounting for the free evolution

$$w^{(n)} \mapsto \frac{r}{s + r + i(h^{\text{free}}_{i^{(n)}i^{(n)}} - h^{\text{free}}_{j^{(n)}j^{(n)}})} w^{(n)}. \tag{5.27}$$

The bias introduced by the importance sampling and realized through the spring constant κ, modifies the weights of the triplets which do not correspond to the physical weights used in averages. Those physical weights can be recovered by the expression $c = bw$, which implies that for an operator A, the expectation values read

$$\text{tr}\,(A\tilde{\rho}) \approx \sum_n w^{(n)} e^{\kappa n_{ij}^2} A_{i^{(n)}j^{(n)}}, \tag{5.28}$$

with $A_{i^{(n)}j^{(n)}} = \langle i^{(n)}|A|j^{(n)}\rangle$ and where $\tilde{\rho}$ is represented by the ensemble $\{(w^{(n)}, i^{(n)}, j^{(n)})\}_n$ via Eq. (5.22). As for the steady-state case, the bias b corresponds to $b(n_{ij}) = \exp(\kappa n_{ij}^2)$.

5.2.3 Evolution in Laplace domain

Typically, in the time domain, the evolution follows a pattern where the estimate at time t serves as an input for the estimate at time $t + \Delta t$, and the time range is constructed as the simulation evolves. Conversely, in the Laplace domain, each s value is the result of an integration over the whole time domain, which means that the efficiency of the method could be massively reduced if one is interested in a dense range of s values to reconstruct $\tilde{\rho}_s$. Due to the parametric nature of the variable s in the simulations, one would naively need to perform an independent simulation for every value of s to obtain its dependence on the correlation function C_s^{AB}. However, by noting that the s value appears only in the free part of the propagator, we can build a procedure where the random spawnings are performed by a single instance of the vectors $(i^{(n)}, j^{(n)})$ and the weights for the whole s range are associated to this single instance. The major part of the execution time is spent on the spawnings, which means that most of the computational time could be spared when producing data points for the whole s range if a single instance of the triplet vectors performs the spawnings.

To be more concrete, let us consider two triplets $(c_{m,s_1}, |\phi_{m,s_1}\rangle, |\psi_{m,s_1}\rangle)$ and $(c_{m,s_2}, |\phi_{m,s_2}\rangle, |\psi_{m,s_2}\rangle)$, which have the exact same trajectory in the Hilbert space but for two different values $s_1 \neq s_2$. The only difference between the two is the application of the free evolution $\mathcal{R}^{\text{free}}_{s+r}$, but they still produce two independent values of the correlation function C_s^{AB}. The idea is to avoid this redundancy by evolving a single instance of the pair

$$(|\phi_m\rangle, |\psi_m\rangle) = (|\phi_{m,s_1}\rangle, |\psi_{m,s_1}\rangle) = (|\phi_{m,s_2}\rangle, |\psi_{m,s_2}\rangle), \qquad \forall m \tag{5.29}$$

for the quantum jumps and associating it to both c_{m,s_1} and c_{m,s_2}, which are evolved freely separately according to $\mathcal{R}^{\text{free}}_{s_1+r}$ and $\mathcal{R}^{\text{free}}_{s_2+r}$, respectively. This situation is depicted in Fig. 5.2. More generally, prior to the simulation we select a range of values $s_1 < s_2 < \cdots < s_{N_s}$ and associate all the corresponding weights $w_{0,s_1}, w_{0,s_2}, \ldots, w_{0,s_{N_s}}$ to a single pair $(|\phi_0\rangle, |\psi_0\rangle)$ on which the jumps are performed.

In practice, we evolve an ensemble of $(N_s + 2)$-tuples $\{(w^{(n)}_{m,s_1}, w^{(n)}_{m,s_2}, \ldots, w^{(n)}_{m,s_{N_s}}, i^{(n)}_m, j^{(n)}_m)\}_n$, where each $(N_s + 2)$-tuple represents N_s triplets each with a different

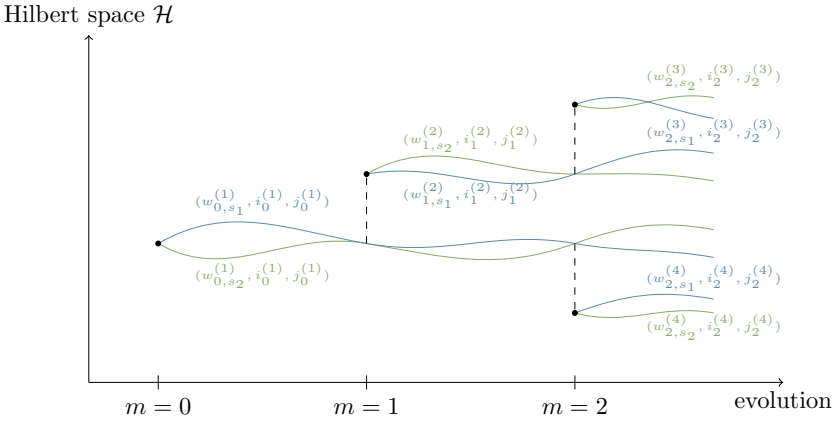

FIGURE 5.2: Example of the evolution of realizations of two triplets $(c_{m,s_1}, |\phi_{m,s_1}\rangle, |\psi_{m,s_1}\rangle)$ (blue) and $(c_{m,s_2}, |\phi_{m,s_2}\rangle, |\psi_{m,s_2}\rangle)$ (green) having the exact same trajectory in the Hilbert space $\mathcal{H}$ but for two different values $s_1 \neq s_2$. The dashed lines represent the spawnings and the solid line the free evolution. Note that only the free evolution differs between the two triplets.

value of s. In this context, the spawnings rule Eq. (5.26) can be updated to

$$(v^{(n)}_{m,s_1}, v^{(n)}_{m,s_2}, \ldots, v^{(n)}_{m,s_{N_s}}, k^{(n)}_m, j^{(n)}_m), \quad v^{(n)}_{m,s_i} = i\frac{h^{\text{int}}_{i^{(n)}k}}{r}\frac{w^{(n)}_{m,s_i}}{N_c}2n_t T_b, \tag{5.30}$$

The equivalent change for the free evolution (5.27) reads

$$w^{(n)}_{m,s_i} \mapsto \frac{r}{s + r + i(h^{\text{free}}_{i^{(n)}i^{(n)}} - h^{\text{free}}_{j^{(n)}j^{(n)}})} w^{(n)}_{m,s_i}, \qquad \forall s_i = s_1, s_2, \ldots, s_{N_s}. \tag{5.31}$$

5.2.4 EFFICIENCY AND COMPLEXITY

Because the real-time algorithm has essentially the same structure as the iterative scheme, we expect the complexity and the parallel behavior to have a similar scaling. Therefore, if the maximum triplet population is denoted with $P_{\max}$, we expect the algorithm complexity to be linear in the population, i.e. $\mathcal{O}(P_{\max}/s_{\min})$. The inverse linear dependence on the s is due to larges times $t_{\max} \sim 1/s_{\min}$ needing longer simulations. See Sec. 4.4 for a more detailed discussion about the population dependence. Concerning the parallel implementation of the algorithm, the same general parallel flow is constructed by distributing the triplets in the ensemble such that each thread has almost the same amount of weights, performing the spawnings locally and synchronizing them to send the spawned triplets to the corresponding thread to perform the annihilation locally. The speed-up is very similar to the one shown in Fig. 4.17. A notable difference in the memory requirement involves the simultaneous simulations for multiple s values. If we are interested in the range of values $s_1, s_2, \ldots, s_{N_s}$, each triplet has N_s weights, each corresponding to a single value of s.

Because the sign problem becomes more severe for large times, it is difficult to produce a chain of correlated samples and estimate the error with a block analysis. To estimate the error, we have to produce independent simulations. Because there is no sampling stage in this variation of the algorithm, the rate parameter r simply determines the convergence speed. A lower rate r implies a fast convergence.

5.3 Population control

The population was defined earlier as the total number of triplets with a weight larger than a unit of weight w_u (see Eq. (5.23)). It reflects the number of spawning attempts performed at each iteration over the main loop. Because each triplet spawns a number of child triplets corresponding to its weight, we need to find efficient ways to reduce population growth. Unlike with the steady state, the population cannot be controlled by a shift because of the nonlinearity it would introduce. The effect of the nonlinearity was not problematic in the steady-state framework because we restricted ourselves to the converged value and not the convergence stage itself. In the current context, however, every step of evolution is needed to obtain the correct final result. We describe here the various tools at our disposal to control the population.

We start by examining in which regime the population control is the most challenging and conclude that the dynamical sign problem causes the population to diverge especially for strong interactions and large times. We then study how to slow down the exponential increase of the population via the parameters r, w_u, and κ. Finally, we observe that the population control issue can be resolved with the deadweight approximation at the expense of introducing a small systematic error.

5.3.1 Dynamical sign problem

Before developing tools to control the population, we want to understand in which regime its growth is problematic and to what extent. Because the exploration of the Hilbert space is performed via the spawnings, we expect the interaction strength to be a parameter on which the population dynamics is highly dependent. Another important parameter is the $s_{\min}$ value, due to its similar role to the shift in the previous chapter from a purely numerical perspective. With the correspondence $1/s_{\min} \sim t_{\max}$, we can assume that the population is more difficult to control for small s values because the errors propagate and accumulate with increasing time.

To understand how the population dynamics depends on these physical parameters, we consider the $L = 12$ quantum Ising chain for $J = 1$, $h^z = 0.6$ with $r = 30$, $\kappa = 0$, and $w_u = 10^{-5}$. Figure 5.3 illustrates the population dynamics for various s values and various interaction strengths h^x. As expected, the population grows faster for strong interactions which comes from the fact that the exploration of the Hilbert space is more significant for spawnings with a large weight. This is reflected in the difference between the two interaction strengths; for $h^x = 0.2$, the random jumps have larger weights according to the jump rule (5.26) and thus, a higher impact on the population dynamics. The s value has a similar numerical effect to the shift, that is the smaller the s the larger the population growth. The critical value s_{cr} above which the population decreases depends of course on the interaction strength, which in turn is connected to the sign problem. Any s value above this threshold does not produce any instabilities, whereas below, for s small, the sign problem occurs and the population diverges. Similarly to the shift explanation, the cancellation rate is too small for the solution of the simulation to emerge when s is below the critical value. Some triplets erroneously remain in the simulation and dangerously spawn new triplets in the next iteration. The effect of noncancellation becomes exponentially stronger as the algorithm tries to compensate for this excess weight, eventually leading to a diverging population.

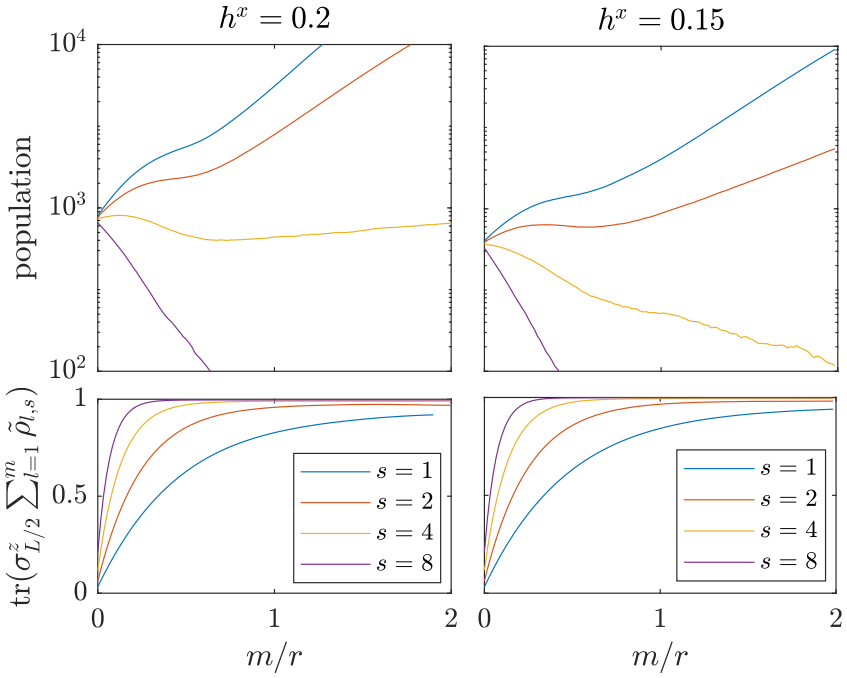

FIGURE 5.3: Upper panels: Population dynamics for the quantum Ising chain with $J = 1$, $h^z = 0.6$, and various s values. The left column shows results for $h^x = 0.2$ whereas the right column for $h^x = 0.15$. The strength of the interaction modifies the population dynamics, whose growth is heavily dependent on the interaction strength h^x. Lower panels: Corresponding convergence to the mean magnetization $C_s^{\sigma^z_{L/2}}$ at the center of the chain.

5.3.2 NUMERICAL PARAMETERS

As we just saw, the population naturally decreases for large s values, which corresponds to small-to-medium times. Below a critical s value, the dynamical sign problem is severe and causes the population to increase exponentially. Because we want to compute the dynamical effects of quantum systems at large times that is $s_{\min} \lesssim 10^{-1}$, we need to understand how we can slow down the population growth by tuning the numerical parameters r, w_u, and κ to obtain results at large times. The role of the three parameter is illustrated in Fig. 5.4, in the case of the $L = 12$ quantum Ising chain for $J = 1$, $h^z = 0.6$, $h^x = 0.2$ and $s = 1$ with various choices for the numerical parameters. As supported by the upper panel, a smaller r value is adequate to weaken the effect of the sign problem on the population growth. The parameter r affects the population dynamics exclusively during the weight update of the free evolution. Because the free evolution resolves continuous processes of a time scale $1/r$, faster oscillations are taken into account when r increases. In analogy to the above discussion about the small s values, the severity of the sign problem grows stronger with smaller time scales (larger r). Note however that a very low parameter r might induce some convergence issues because the scheme gets closer to perturbation theory and the magical formula might not be able to recast perturbative expansions into a convergent sum. As illustrated in the middle panel, the dependence between the population dynamics and the unit of weight is linear with some secondary effects later during the simulation. The unit of weight w_u measures a minimal weight for which the triplets (w, i, j) are considered as a single entity. Below this critical value $|w| < w_u$, the triplets undergo a survival test, which removes the unimportant

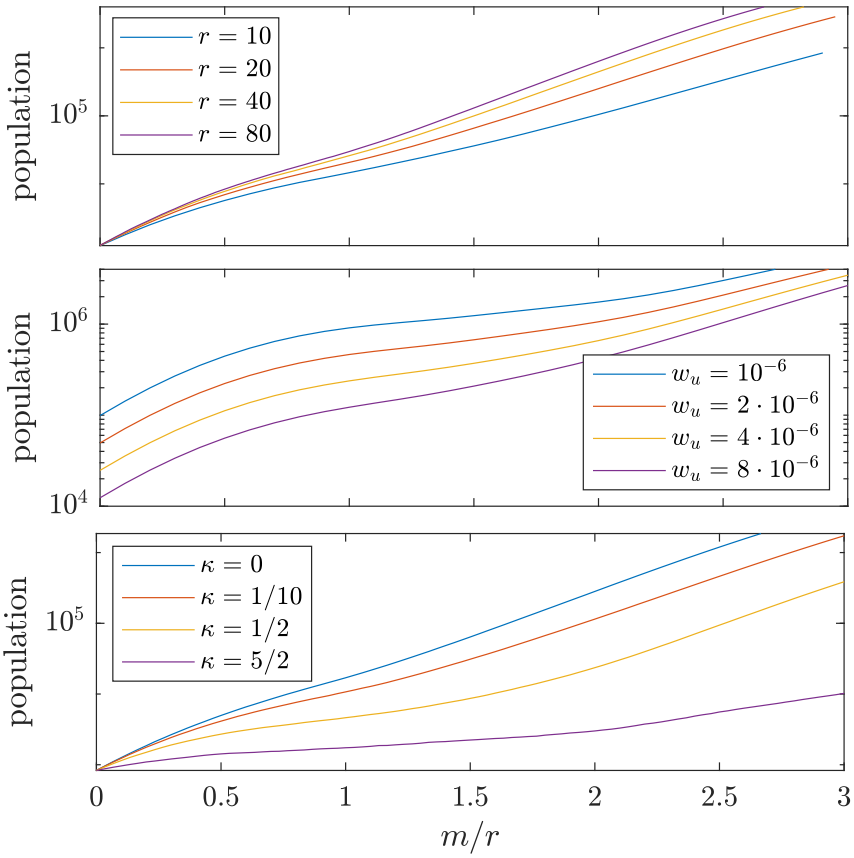

Figure 5.4: Population dynamics for the quantum Ising chain with $J = 1$,$h^z = 0.6$, and $h^x = 0.3$ when varying the numerical parameters of the simulation r (upper panel), w_u (middle panel) and κ (lower panel). Unless stated otherwise, the values are $r = 30$, $w_u = 10^{-5}$, and $\kappa = 0$.

triplets from the simulation. Intuitively, a smaller unit of weight induces a larger population and vice versa. Similar to the steady-state method, the importance sampling was introduced to reduce the statistical variance of the final result by restricting the exploration of the Hilbert space to only regions that participate to the statistical averages. The choice of the importance sampling parameter κ, the spring constant, has a direct impact on the population. In fact, the main effect of the importance sampling is to reduce the population of triplets with a large dynamical norm, leading to a lower total population as illustrated by the lower panel.

Nevertheless, if the spring constant is chosen too large, we observe a gap between our estimation of the observable and its exact value, originating from the ergodicity breaking that was explained in details in Sec. 4.3.3. Figure 5.5 illustrates this gap for the mean magnetization $C_s^{\sigma^z_{L/2}}$ in the $L = 8$ XXZ Heisenberg chain for $J^z = 1.5$, $J^{xy} = 1$ and $s = 1/10$. The error bars were calculated over 30 independent simulations with $r = 30$, $w_u = 10^{-4}$, $u_{\mathrm{dw}} = 1.125\ w_u$ enabled at $m/r = 6$.

5.3.3 Deadweight approximation

To find a way to access large-times dynamical properties, we need to restrain the growth of the population and eliminate the instabilities. This task is carried out by the deadweight approximation that helps stabilize the simulations. The idea behind

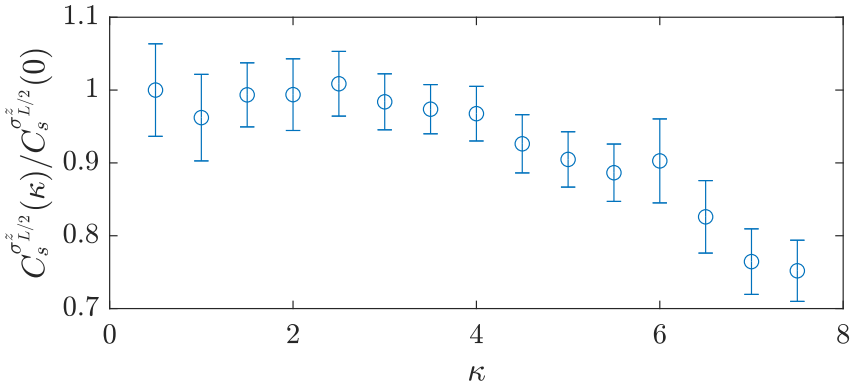

FIGURE 5.5: Estimation of the magnetization $C_s^{\sigma^z_{L/2}}$ as a function of the spring constant κ for the XXZ Heisenberg chain with $J^z = 1.5$, $J^{xy} = 1$, and $s = 1/10$.

the deadweight approximation is to forbid all triplets with a weight smaller than u_{dw} in absolute value to spawn, while still allowing them to evolve freely. This way, the statistically unimportant triplets either stay inactive until they reach the critical value or die if no jumps reinforce their weight. This approximation introduces a systematic error that increases with a larger threshold u_{dw}. The following procedure is introduced to minimize these deviations but still allow the population to be under control; the threshold is set to $u_{\mathrm{dw}} = 0$ at the beginning of the simulation, and when the desired population is reached, the discrimination of unimportant triplet is switched on with a nonzero value $u_{\mathrm{dw}} \neq 0$. Thus, the systematic error is optimized to the computational capabilities because the systematic errors start to accumulate only when the population reaches its maximum value. If the latter population is large enough, we expect that the approximate contribution to the magical formula is only a marginal portion of the final result.

To analyze this systematic error, as well as the role of the population control parameter u_{dw}, we consider the $L = 12$ XXZ Heisenberg chain for $J^{xy} = 1$, $J^z = 0.9$ and $s_{\min} = 1/20$ with $r = 30$, $\kappa = 2$ and $w_u = 10^{-3}$. Figure 5.6 illustrates the population dynamics and the convergence to the mean magnetization at the center of the chain, $C_s^{\sigma^z_{L/2}} = \mathrm{tr}(\sigma^z_{L/2}\tilde{\rho}_s)$. The vertical lines in the upper panel represent the iteration at which the approximation was enabled. The solid vertical line corresponds to $m/r = 8$ and is associated to the solid lines, whereas the dot-dashed vertical line situated at $m/r = 4$ is associated to the dot-dashed purple curve. Obviously, the deadweight approximation slows down the population growth by removing unimportant triplets. The rate of the population growth after enabling the approximation depends on the strength of the threshold u_{dw}, that is the stronger the threshold the slower the increase. If u_{dw} is too large, the population can possibly decrease and the triplets would eventually all be killed. This scenario has to be avoided because the contributions that are estimated with a small number of triplets are more likely to have non-negligible systematic errors. The lower panel illustrates the convergence to the mean magnetization defined by Eq. (5.13) for various thresholds u_{dw}. The estimation of magnetization at iteration m is computed with the density matrix $\sum_{l=1}^{m} \tilde{\rho}_{m,s}$, where $\tilde{\rho}_{m,s}$ was defined in Eq. (5.22) and the solution $\tilde{\rho}_s$ is recovered for $m \to \infty$. The exact solution is represented by the dashed black line, whereas the errors from the stochastic simulations are depicted by the shaded areas. The errors were calculated over 30 independent simulations and contain both the statistical errors and the systematic ones. We do not observe any deviation from the exact result that

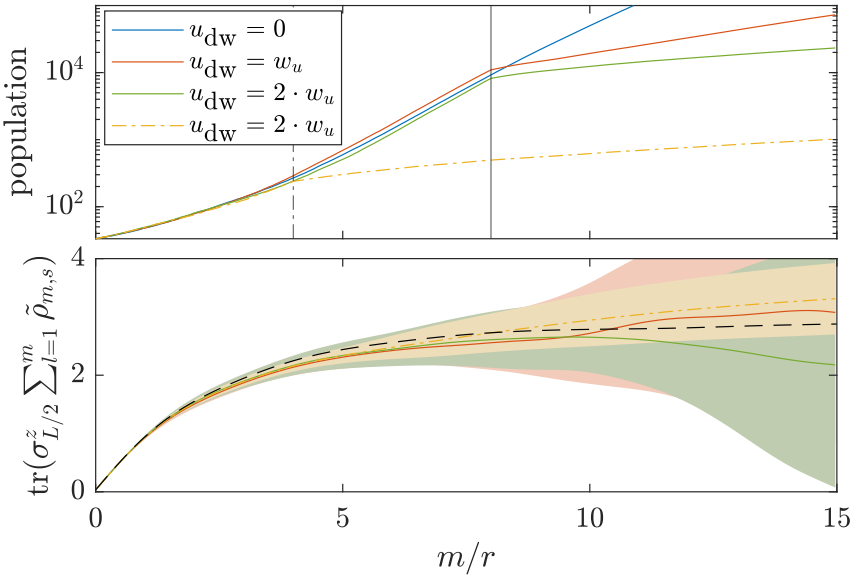

Figure 5.6: Upper panel: Population dynamics for the XXZ Heisenberg model with $s_{\mathrm{min}} = 1/20$ and various values of the deadweight u_{dw}. The approximation was enabled at $m/r = 8$ for the solid lines and at $m/r = 4$ for the purple line. Lower panel: Corresponding convergence to the mean magnetization $C_s^{\sigma^z_{L/2}}$ at the center of the chain. The exact result is depicted in the black dashed line. The systematic error introduces by the deadweight approximation is not visible.

cannot be explained by the statistical errors. The systematic errors introduced by the deadweight approximation are therefore negligible.

To understand the interplay between the importance sampling and the deadweight approximation, we introduce Fig. 5.7, illustrating a u_{dw} analysis of the $L = 10$ XXZ Heisenberg model for various κ with $J^z = 0.9$, $J^{xy} = 1$, $s_{\mathrm{min}} = 1/10$, and $r = 30$. The deadweight approximation was enabled at $m/r = 4$. The sign problem and the related divergences limited our choice of the minimum deadweight u_{dw}. The dependence between the spring constant and the deadweight has to be tuned in order to obtain optimal convergent simulations. Generally, improving the efficiency of the simulations is a trade-off between the parameters κ and u_{dw}. If the spring constant is large, the dead weight has to be chosen small, and vice versa. As an example, if the observable is sampled by triplets away from the diagonal, it might be more efficient to select a smaller spring constant κ and a larger deadweight u_{dw} to increase the number of triplets with a high dynamic norm and hence reduce the variance. In optimizing the parameters, one should start from large values and decrease them until the final result becomes constant within the statistical error. If the systematic errors become non-negligible, one can still perform an analysis of the u_{dw} dependence and extrapolate the result for vanishing u_{dw}.

5.4 Inverse Laplace transformation

So far, all the quantities have been computed in the Laplace domain and the magical formula has provided results in the s domain. Because the Laplace transform mixes all the time scales, it would be preferable to extract the dynamical properties of our quantum systems directly in the time domain. For that, we have two choices, the first is to develop a similar algorithm in the time domain, i.e. an algorithm that

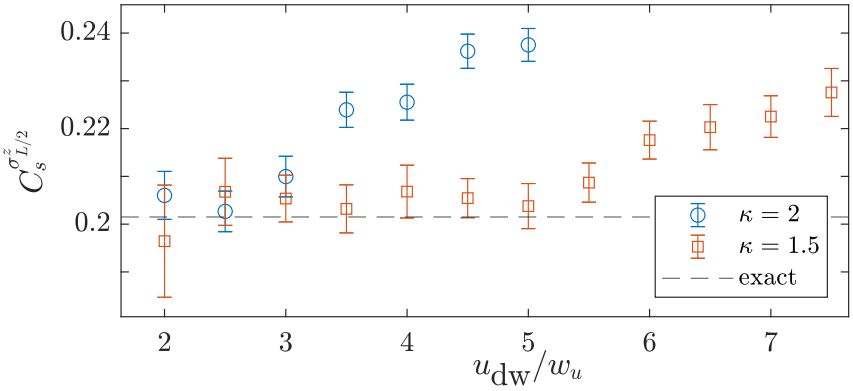

FIGURE 5.7: Estimations of the magnetization $C_s^{\sigma^z_{L/2}}$ for various dead weights u_{dw} and spring constants κ. The model is the $L = 10$ XXZ Heisenberg chain, with $J^z = 0.9$, $J^{xy} = 1$, $s_{\mathrm{min}} = 1/10$, and $r = 30$. The errors were calculated over 100 independent simulations.

reproduces the superoperator in Eq. (2.31). The second is to transform the result in the Laplace domain back into the time domain using a numerical inverse Laplace transform. As we already saw in Sec. 2.2.3, the first solution is problematic, due to the convolutions in the expression of the evolution superoperator and the inefficiency in the weak coupling regime. The second solution is preferable and implies numerical approximations of the inverse Laplace transform. These inverse methods are usually stable only for short times and need a closed form of the function to invert. The reason for these instabilities originates from the definition of the Laplace transform that damps the signal exponentially for large times (see definition of the Laplace transform (2.33)). Thus, the inverse Laplace transform has to increase the signal exponentially, which converts small random noise into major instabilities [117, 118]. Surprisingly, the Zakian method to invert the Laplace transform is less sensitive to these instabilities and provides accurate results for medium times.

In this section, we first introduce three numerical methods to invert a signal in the s domain. We then define a procedure to apply these methods to the actual data obtained from a simulation with the magical formula and test these methods with concrete data. Finally, we briefly discuss how the same dynamical properties can be extracted directly in the Laplace domain and conclude that the inverse Laplace transform should be used as a tool to get an intuition about the dynamics of the system.

5.4.1 NUMERICAL METHODS

As we just mentioned, the inverse Laplace transform is very sensitive to small fluctuations in the signal because these increase exponentially in the inverse procedure. It is preferable to apply the inverse Laplace transform to systems characterized by damped oscillations or out-of-equilibrium steady states where the signal oscillates with a typical frequency $\omega > s_{\mathrm{min}}$. In the worst case, we can expect the instabilities to become relevant only after the first oscillation. Conversely, time signals that increase in amplitude with time are completely out of reach by the inverse methods because of the instabilities aforementioned.

The general strategy to inverse Laplace transform a collection of points in the s domain is to obtain an analytic expression of a fit, to extrapolate over the whole s range, and finally to use the expression for this function as an input for the numerical

inverse methods. In the literature, multiple numerical methods can be found to invert the Laplace transform. There exists a few that can be used for a large variety of functions but they are usually computationally expensive and are defined in the complex domain, which involves extrapolation of the data in the complex plane. Here, we show that the Zakian method is best suited for the type of functions we want to invert by comparing it to the Gaver-Stehfest method and the fast Fourier transform (see [119, 120] for reviews on inverse numerical methods). The Zakian method is described in details in App. B.1. It is fast to implement and has a single parameter n to adjust. This parameter denotes a truncation in the infinite series used to approximate the time function. For our simulations, we used $n = 5$.

Figure 5.8 illustrates the result of a numerical inverse Laplace transform using Zakian, Gaver-Stehfest, and fast Fourier transform methods on various signals. The first signal $f_1(t) = 0.8 + 0.2\cos(t)\cos(t/4)$ approximates a typical scenario with two oscillations of similar frequencies. The second signal $f_2(t) = (0.8 + 0.2\cos(t))e^{-t/4}$ reproduces a damped oscillation and the last signal $f_3(t)$ comes from simulation data from the mean magnetization $C_s^{\sigma^z_{L/2}}$ of a $L = 8$ quantum Ising chain with $J = 1$, $h^z = 0.6$, $h^x = 0.2$ and $s_{\min} = 1/10$. The corresponding function in the time domain $f_3(t) = \langle\sigma^z_{L/2}\rangle_t$ was simulated by an exact diagonalization. As shown in Fig. 5.8, the

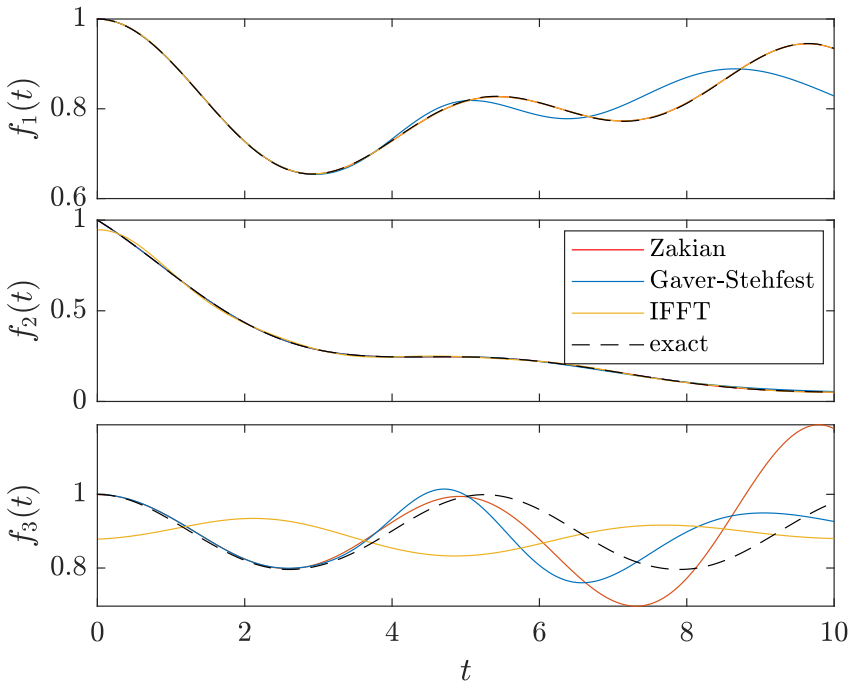

FIGURE 5.8: Numerical inverse Laplace transforms of the functions $\tilde{f}_1(s)$ (upper panel), $\tilde{f}_2(s)$ (middle panel), and $\tilde{f}_3(s)$ (lower panel) using various methods. The functions $f_1(t) = 0.8 + 0.2\cos(t)\cos(t/4)$ and $f_2(t) = (0.8 + 0.2\cos(t))e^{-t/4}$ where inverted from the analytical form in the Laplace domain. The signal $f_3(t) = \langle\sigma^z_{L/2}\rangle_t$ is the mean magnetization at the center of the chain and was computed with exact diagonalization for a quantum Ising chain.

Zakian method provides the best fit in all of the three test situations. Even for the real data situation, which consists of a very slowly decaying cosine, the instabilities occur only for $t \sim 5$. The first oscillation can be measured with precision and relevant dynamical properties can be extracted.

5.4.2 DATA FITTING

In addition to the dependence on the method used, inverting a signal in the s domain is highly sensitive to the fit and the extrapolation. Because the whole s range is needed, this extrapolation has to be performed with caution. Noting that in the Laplace domain, the signal usually takes the form $\tilde{f}(s) = p_{n_f}(s)/p'_{n_f}(s)$, where $p_{n_f}(s) = \alpha_0 + \alpha_1 s + \cdots + \alpha_{n_f} s^{n_f}$ is a polynomial of degree n_f, we define the following procedure to obtain a fit consistent with the signal in the time domain. First, we assume the following form for the fit

$$\text{fit} \sim s\frac{p_{n_f-1}(s)}{p'_{n_f}(s)}. \tag{5.32}$$

Prior to any fitting, we note that a first parameter can be fixed because the limit $s \to \infty$ is usually known. Additionally, we can safely assume that the function is smooth and has no poles, which implies that $\alpha'_i > 0$ for any $i = 1, \ldots, n_f$. The procedure starts by fitting the signal with $n_f = 2$, for which the parameters α_i and α'_i are optimized. The optimal parameters are then used as initial guesses for a fitting with $n_f = 3$. If the initial parameters were chosen carefully, the iterative scheme should make the optimal parameters converge to a constant value. The iteration is stopped when the parameters start to diverge. The upper panel of Fig. 5.9 shows a signal in the Laplace domain together with the fits from the above procedure. The lower panel displays the inverse Laplace transform with the Zakian method associated with the same fits. The signal in the Laplace domain (grey crosses) was obtained

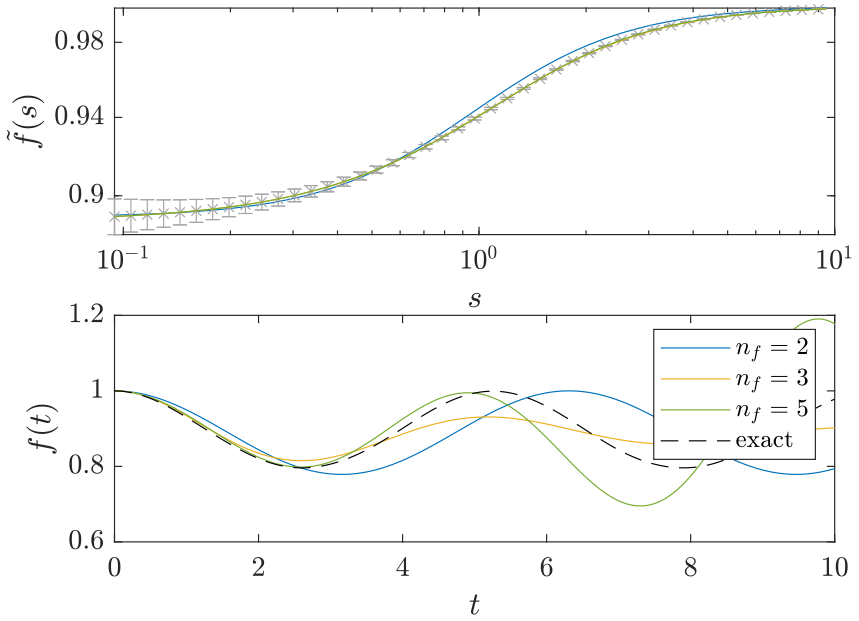

FIGURE 5.9: Upper panel: Fits of the mean magnetization $\tilde{f}(s) \equiv C_s^{\sigma^z_{L/2}}$ quantum Ising chain. The fits have the form $sp_{n_f-1}(s)/p_{n_f}$. The grey crosses are data from a stochastic simulation. Lower panel: inverse Laplace transform corresponding to the fit in the upper panel. The exact result was computed from an exact diagonalization.

from simulations of the mean magnetization $C_s^{\sigma^z_{L/2}}$ for a $L = 8$ quantum Ising chain with $J = 1$, $h^z = 0.6$, $h^x = 0.2$ and $s_{\min} = 1/10$. The error bars were calculated over 30 independent simulations and the numerical parameters were $r = 30$, $\kappa = 2$,

$w_u = 10^{-6}$ and $u_{\mathrm{dw}} = w_u$ was enabled at $m/r = 12$. We notice that the results depend strongly on the fit, which means that the signal in the time domain can be trusted up $t \sim 5$ at best, after which instabilities become important.

As a final remark, we want the reader to be aware of the careful interpretations that can be done with results in the time domain obtained via an inverse Laplace transform. Even though the main dynamical properties can be extracted, the final result is strongly dependent on a lot of intermediate steps whose validity can only be checked if the exact solution is known. To obtain accurate results of dynamical properties such as frequencies or damping coefficients, it is preferable to compute them directly in the Laplace domain. Appendix B.2 shows examples of how to extract these properties from a signal in the Laplace domain. We insist that the Laplace dynamics has to be considered as an equivalent way to compute the evolution of quantum systems without loss of information. An educated reader certainly recognizes the dynamical properties in a Laplace signal and knows how to extract them. Therefore, we recommend using the inverse Laplace transform only as a guide to get an intuition about the behavior of the quantities of interest.

5.5 Concrete calculations and examples

The insights of the previous sections allowed us to introduce an approximation that resulted in convergent simulations for long times and to define a procedure for the inversion of the Laplace transform. We can now focus on concrete problems whose system size is too large to be solved by brute force. The observables we study evolve according to the Hamiltonian Eqs. (5.6) and (5.14) that describe the XXZ Heisenberg and the quantum Ising chains of length L, respectively. For the XXZ Heisenberg model, we concentrate on highlighting the ability of the algorithm to measure a phase transition in the propagation of excitations across the chain. For the quantum Ising chain, we tune the parameters so that confinement of spins with opposite signs can be observed by measuring dynamical quantities associated to this confined state. Unless stated otherwise, we consider lattices of size $L = 40$, which is too large to be stored in a computer. This maximum lattice size is constrained by the use of small computational clusters to produce the results. The maximum number of triplets in the simulations was about 10^6, which is only a small fraction of the typical size of the corresponding density matrix. As an example, these matrices have $1.9 \cdot 10^{22}$ entries for the XXZ model and $1.2 \cdot 10^{24}$ for the Ising model. We are able to simulate larger systems in the Ising model mainly because the physics of confinement is local, in the sense that the dynamics is a statistical mixture of a few similar states.

With our first concrete example, we illustrate the transition from ballistic to suppressed propagation of spin excitations within the XXZ Heisenberg chain Eq. (5.6) for different values of J^z. We prepare the initial density matrix in the domain wall state (5.10), a highly excited state, where $J^{xy} = 0$, and instantaneously quench the Hamiltonian to $J^{xy} = 1$. To follow the dynamics of the spin excitations, we consider the magnetization profile

$$C_s^{\sigma_\mu^z} = \mathrm{tr}(\sigma_\mu^z \tilde{\rho}_s), \tag{5.33}$$

with μ the lattice site. Figure 5.10 illustrates the evolution of the absolute value of the magnetization profile for $J^{xy} = 1$, $s_{\mathrm{min}} = 1/10$, in both the ballistic $J^z = 0.6$ (upper panel) and strongly interacting regime $J^z = 1.5$ (lower panel). The observables were averaged over 100 independent simulations with $r = 100$, $\kappa = 4$, $w_u = 10^{-3}$, and where $u_{\mathrm{dw}} = 1.5\ w_u$ was enabled at $m/r = 12$. The final population for each

independent simulation was about 10^5 triplets. For $J^z < J^{xy}$ the spin excitations

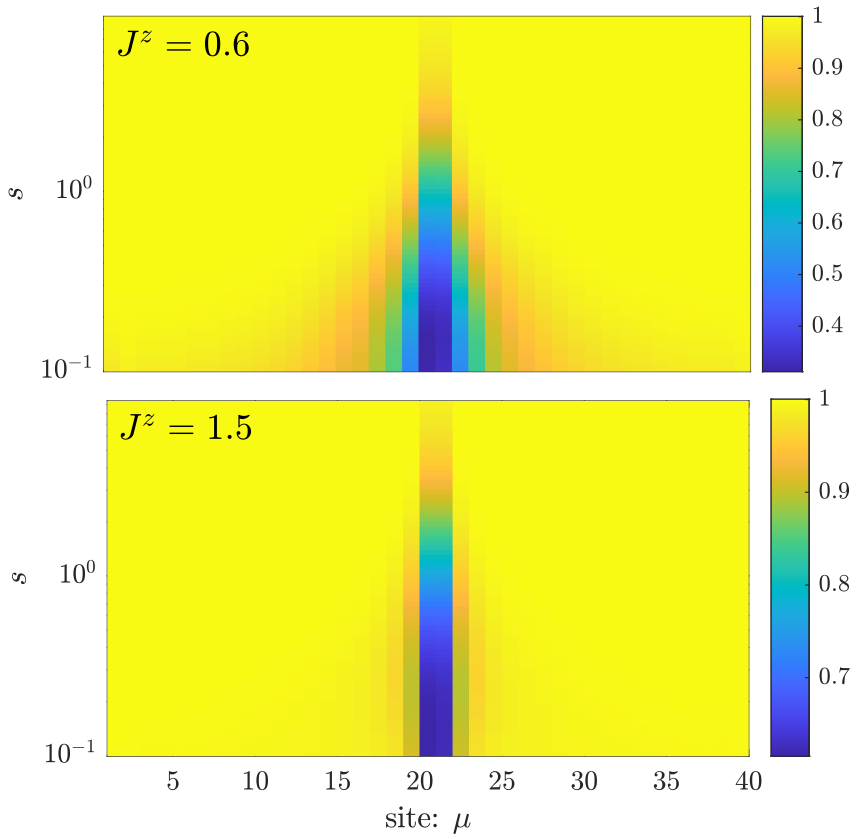

FIGURE 5.10: Dynamics of the absolute value of the magnetization profile $|C_s^{\sigma_\mu^z}|$ in the Laplace domain for the XXZ Heisenberg chain with $J^{xy} = 1$. Ballistic transport is visible in the upper panel whereas transport is almost completely suppressed in the lower panel.

travel ballistically across the chain, independently of its length. On the contrary, for $J^z > J^{xy}$, propagation is suppressed by the strong σ_z coupling which prevents the spins to flip signs. To measure this sharp transition, we consider the Loschmidt echo, defined in the time domain as $|\langle\psi_0|e^{-iHt}|\psi_0\rangle|^2$. The echo measures the sensitivity of a quantum evolution to perturbations by quantifying the return probability of the initial state during the evolution. In the Laplace domain, it takes the form

$$L(s) = s\mathrm{tr}(\rho_0 \mathcal{R}_s \rho_0) \equiv \mathrm{tr}(\rho_0 \tilde{\rho}_s), \tag{5.34}$$

where $|\rho_0\rangle\langle\rho_0|$ is the initial state. Figure 5.11 depicts the evolution of $L(s)$ for the $L = 40$ XXZ Heisenberg chain with $J^{xy} = 1$ and various J^z from the initial state (5.10). The error bars were computed over 30 independent simulations with $r = 30$, $\kappa = 1$, $w_u = 10^{-3}$, and where $u_{\mathrm{dw}} = 1.2\ w_u$ was enabled at $m/r = 12$. The final triplet population was about $2 \cdot 10^6$ and the exact solution was obtained by solving analytically for $J^z = 0$.

The suppression of transport around $J^z = J^{xy}$ can be observed by the nonvanishing probability of return in the limit $s \to 0$. It supports the observation made in Fig. 5.10 and reproduces the results obtained for smaller systems via exact diagonalization in [121].

Next, we study the confinement of a pair of opposite spins in the quantum Ising chain. The confinement mechanism can be intuitively understood by remembering

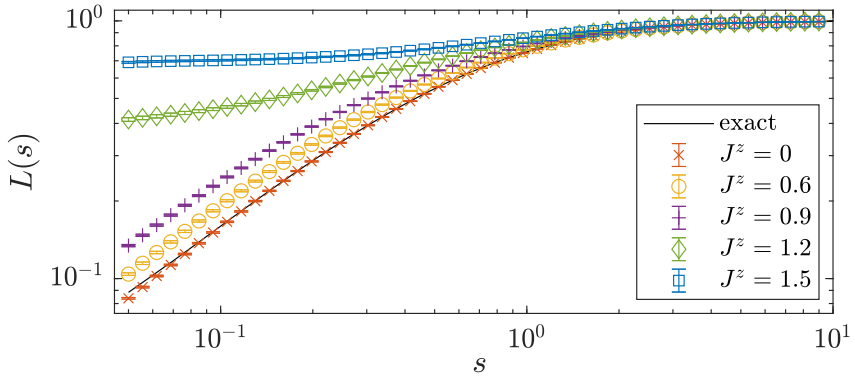

FIGURE 5.11: Dynamics of the Loschmidt echo $L(s)$ in the Laplace domain for the $L = 40$ XXZ Heisenberg chain with $s_{\min} = 1/20$, $J^{xy} = 1$, and various strengths J^z.

that for a vanishing longitudinal field h^z the ground state is degenerate due to a spin flip symmetry and takes the form of domain walls of various sizes. If the longitudinal field is set to $h^z \neq 0$, the ground state degeneracy breaks due to the energy gap created between the spin domains. The spin domains along the field h^z increase in energy and hence the field acts as an attracting potential between the walls delimiting a spin domain. This confinement can be observed with our algorithm by preparing the initial state in Eq. (5.10) with no longitudinal field and instantaneously quenching the Hamiltonian to $h^z \neq 0$. The initial state $|\text{ini}\rangle$ is characterized by a spin kink exactly in the middle of the chain. Figure 5.12 illustrates the evolution of the energy density profile $C_s^{H_\mu} = \text{tr}(H_\mu \tilde{\rho}_s)$, in the Laplace domain with

$$H_\mu = -J\sigma_\mu^z \sigma_{\mu+1}^z - \frac{h^x}{2}(\sigma_\mu^x + \sigma_{\mu+1}^x) - \frac{h^z}{2}(\sigma_\mu^z + \sigma_{\mu+1}^z), \tag{5.35}$$

with μ the lattice site for an $L = 40$ chain with $J = 1$, $h^x = 0.2$, $h^z = 1.2$, $s_{\min} = 1/20$, and starting from the initial state Eq. (5.10). The results were averaged over 30 independent simulations, with $r = 30$, $\kappa = 3$, $w_u = 4 \cdot 10^{-6}$, and $u_{\text{dw}} = 1.5\ w_u$ enabled at $m/r = 6$. The absence of energy exchange and spin excitation propagation

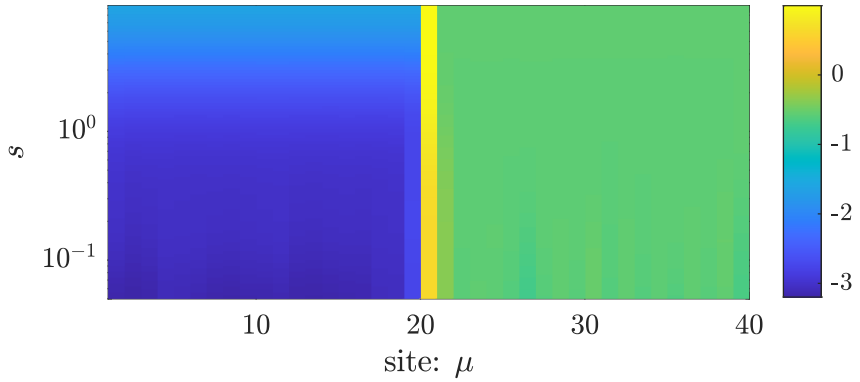

FIGURE 5.12: Dynamics of the energy density profile $C_s^{H_\mu}$ in the Laplace domain for the $L = 40$ quantum Ising chain with $J = 1$, $h^x = 0.2$, and $h^z = 1.2$ starting from the initial state (5.10).

between the two domains can be explained by considering the mid-kink as a quasi-particle. The motion of the kink is triggered by the quench of the longitudinal field

h^z, which gives a kinetic energy gain of order h^z allowing the kink to move within the potential. However, due to energy conservation, the kink has to bounce back, hence creating oscillations centered around the central bond connecting $L/2$ and $L/2+1$. This leads to a confinement of the central spin pair of opposite signs. The oscillations can be measured by considering the evolution of the magnetization of the left spin of the mid-kink's pair, $C_s^{\sigma^z_{L/2}}$. These are illustrated in the upper panel of Fig. 5.13 in the Laplace domain for a $L = 20$ chain with $J = 1$, $h^x = 0.2$, $s_{\min} = 1/10$, and several confining potentials, whereas the lower panel depicts the logarithmic derivative of the above signal. The error bars were calculated over 30 independent simulations with $r = 30$, $w_u = 4 \cdot 10^{-5}$. The deadweight approximation was enabled at $m/r = 6$ with $u_{\rm dw} = 1.6\ w_u$, $1.5\ w_u$, $1.8\ w_u$ for $h^z = 1.2$, 0.6, 0.3, respectively. The choice of specific thresholds $u_{\rm dw}$ is due to the optimization procedure. Note that as described

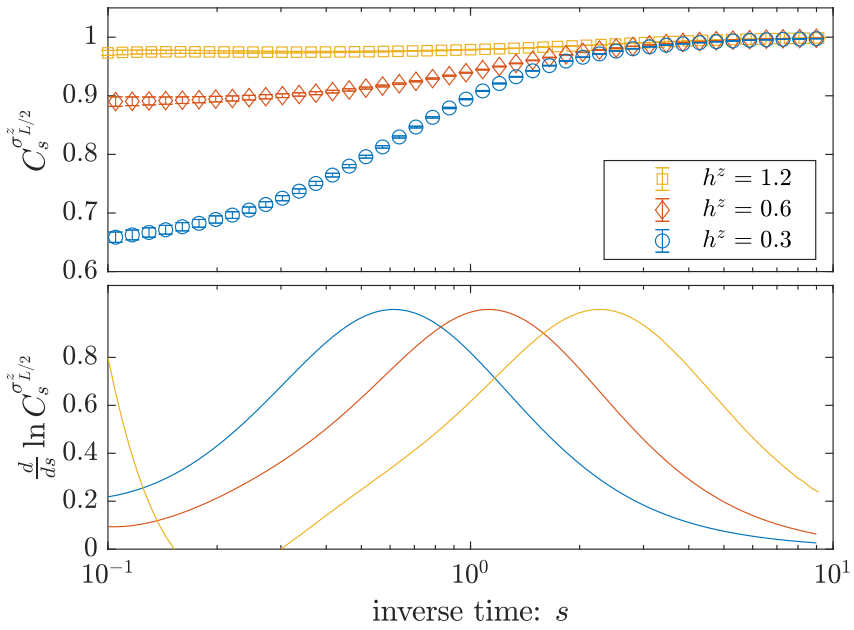

FIGURE 5.13: Upper panel: Dynamics of the magnetization of the spin on the left of the central pair $C_s^{\sigma^z_{L/2}}$ in the Laplace domain for the $L = 20$ quantum Ising chain with $J = 1$, $h^x = 0.2$, and various h^z strengths. Lower panel: Logarithmic derivative of the magnetization $C_s^{\sigma^z_{L/2}}$.

in App. B.2, the oscillations take the form of Lorezian curves in the Laplace domain and the frequency of the confining oscillations can be extracted as the inflection point on these curves. The derivatives were calculated using a cubic spline fitting, and the oscillations frequency is represented by the location of the peak. Additionally, in the upper figure, we can extract the oscillation amplitudes from the distance between the values $C_{s=0}^{\sigma^z_{L/2}}$ and $C_{s=\infty}^{\sigma^z_{L/2}}$. We observe that these amplitudes and frequencies scale as $\sim h^x/h^z$ and $\sim h^z$, respectively, which is in agreement with the quasi-particle interpretation of the kink dynamics and with the findings reported in [122].

We compute these oscillations in the time domain using the Zakian method and the fitting procedure described in Sec. 5.4. Figure 5.14 displays the time evolution of the mean magnetization $\langle \sigma^z_{L/2} \rangle_t$ obtained with the Zakian method and a fit of order 5 in each case. These results further support the interpretation made in the Laplace domain, namely that the frequency of the oscillations depends linearly on the

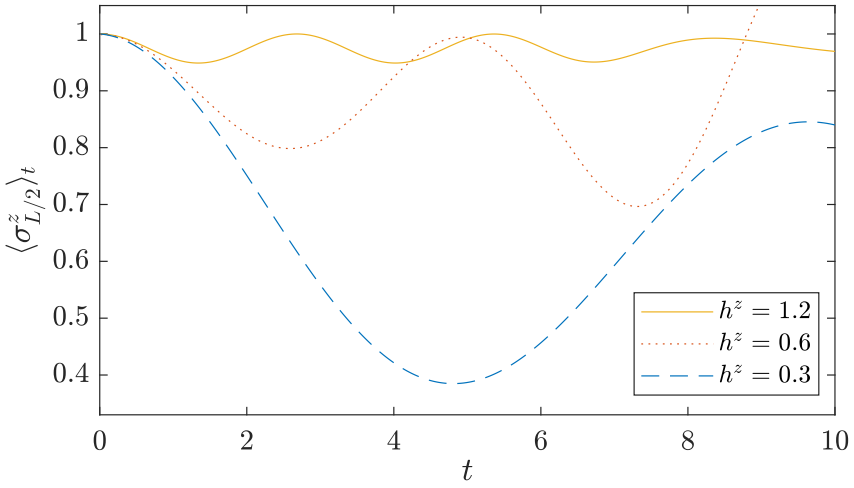

FIGURE 5.14: Time evolution of the magnetization $\langle\sigma^z_{L/2}\rangle_t$ calculated from an inverse Laplace transform from the data of Fig. 5.13 using the Zakian method.

longitudinal field h^z and the amplitude is inversely proportional to the field amplitude itself. As illustrated in Fig. 5.12, the oscillations are localized around the central bond. The instabilities and the damping that are visible around $t \sim 8$ are due to the interplay between the precision of the fit and the inverse numerical methods. Note that the inverse Laplace transform was used as a confirmation that our interpretation of the data in the s range was correct but not directly as a tool to extract the dynamical properties. With this example we want to show that it is possible to use the s domain to compute the dynamical quantities of interest, emphasizing the non-necessity of the time signal and the power of the Laplace transform.

Regardless of the dimensionality of the system, the main limitations of our approach are the size of the Hilbert space and the magnitude of the coupling between the free and interactive parts. The first limit can be compensated by higher computational resources, while the second is inherent to the form of the evolution superoperators and poses a severe restriction on strongly correlated systems. To confirm the first claim, we briefly show how our method can simulate quantum dynamics in higher dimensions by studying the magnetization dynamics of a two-dimensional $L \times L$ square Ising model where the Hamiltonian is given by (5.17). To study the reversible dynamics, we quench the system from the ground state of the Hamiltonian without transverse field $h^x = 0$ to nonvanishing field values within the same phase. The initial state reads

$$\rho_0 = |\uparrow \ldots \uparrow\rangle\langle\uparrow \ldots \uparrow|. \tag{5.36}$$

Because the many-body phase remains unchanged, we expect the quench to create oscillations of small amplitude that will diffuse in the lattice, leading to damping. Figure 5.15 illustrates the time evolution of X defined in Eq. (5.18) for a 5×5 Ising model with $J = 1$ and different field quenches. The data were simulated in the Laplace domain for $s = 1/2$, $r = 30$ and $w_u = 10^{-4}$. For the fields $h^x = 0.25$ and $h^x = 0.5$, the biases were $\kappa = 0.2$, $u_{\mathrm{dw}} = 1.2\ w_u$ and $\kappa = 0.5$, $u_{\mathrm{dw}} = 1.6\ w_u$, respectively. The deadweight approximation was activated at $m/r = 4$. The procedure described in Sec. 5.4 was applied to transform the signal in the time domain. These results are in very good agreement with those reported in [116]. The number of triplets was about $2 \cdot 10^5$ while the density matrix has about $1.1 \cdot 10^{15}$ elements. This figure shows a two-dimensional example where the simulations were performed in the Laplace domain

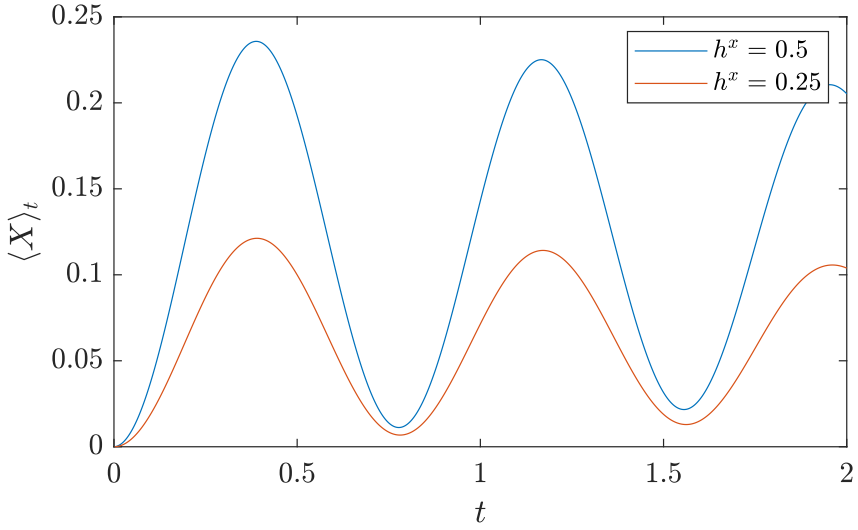

FIGURE 5.15: Time evolution of the total transverse magnetization X for the square Ising model 5×5 with $J = 1$ and various strengths h^x from the state Eq. (5.36).

and inverted with the Zakian method.

6 Summary and outlook

Dissipative quantum field theory is an alternate description of fundamental particle physics with great perspectives in both its theoretical formulation with insights into a more fundamental description of gravity [123, 124] and its numerical applications [53, 88]. Some of these numerical applications were considered in this work to compute unknown ground states of many-body Hamiltonians, and calculate properties of multi-dimensional reversible quantum systems on long time scales. We addressed the major common numerical issues encountered in similar methods and also laid the algorithmic foundations of future quantum chromodynamics simulations. To facilitate discussion of future perspectives, a concise summary of the previous chapters is presented here. This summary is an effort to condense in a self-consistent way the material presented in this dissertation by arguing with our fundamental ideas. It is followed by a discussion on the short- and long-term perspectives of triplet unraveling with applications to both low- and high-energy physics.

The fundamental particles were described in terms of a Hamiltonian H whose dynamics is dictated by the linear quantum master equation

$$\frac{d}{dt}\Delta\rho_t = \mathcal{L}\Delta\rho_t \equiv -i[H, \Delta\rho_t] + \sum_{\boldsymbol{k}\in K^d} \gamma_k \left(2a_{\boldsymbol{k}}\Delta\rho_t a_{\boldsymbol{k}}^\dagger - \{a_{\boldsymbol{k}}^\dagger a_{\boldsymbol{k}}, \Delta\rho_t\}\right), \tag{6.1}$$

describing a ϕ^4 theory for $\Delta\rho_t = \rho_t - \rho_{\text{eq}}$, with ρ_t the density matrix of the system and γ_k dissipative coefficients. We expressed the evolution superoperator in the Laplace domain to avoid convolutions and to improve the efficiency of the method in the weak coupling regime. Some short mathematical developments led to the fundamental form of the evolution superoperator in the Laplace domain, the magical formula,

$$\mathcal{R}_s = \sum_{m=0}^{\infty} r^m \left[\mathcal{R}_{s+r}^{\text{free}}\left(1 + \frac{\mathcal{L}^{\text{int}}}{r}\right)\right]^m \mathcal{R}_{s+r}^{\text{free}}, \tag{6.2}$$

with $r > 0$ a rate. The Hamiltonian was separated into a free part corresponding to the kinetic energy and a collision part accounting for the interactions between fundamental particles. The superoperators were defined as $\mathcal{L} = \mathcal{L}^{\text{free}} + \mathcal{L}^{\text{int}}$, $\mathcal{L}^{\text{int}}\rho = -i[H^{\text{int}}, \rho]$, and $\mathcal{R}_s = \frac{1}{s-\mathcal{L}}$. It was argued that due to the use of the Fock basis, the free part is exactly solvable and the collision part generates transitions between Fock states at rate r. We noted that together, they form a natural setting for piecewise deterministic processes. Stochastic unraveling provided an ideal framework to develop such piecewise deterministic processes and served as an inspiration for stochastic simulations. However, a major difference with the usual unraveling is that the dissipation is contained in the free part and is treated exactly whereas the

interactions are incorporated into the random jumps. We defined the quantities of interest as the correlation functions of the following type for general operators A, B,

$$s\ \mathrm{tr}(B\mathcal{R}_s(A\rho_{\mathrm{eq}})) = s\ \mathrm{tr}(B\rho_{\mathrm{eq}})\mathrm{tr}(A\rho_{\mathrm{eq}}) + \mathrm{tr}(B\mathcal{R}_s\Delta\tilde{\rho}_s), \tag{6.3}$$

where $\Delta\tilde{\rho}_s = s(A - \mathrm{tr}(A\rho_{\mathrm{eq}}))\rho_{\mathrm{eq}}$ is the Laplace counterpart of $\Delta\rho_t$.

The alternate splitting allowed us to develop a triplet unraveling, inspired by the two-process unraveling in Chap. 3. We based our unraveling on the fundamental idea to reproduce the application of the magical formula by considering the evolution of triplets $(c_m, |\Phi_m\rangle, |\Psi_m\rangle)$, where c_m is complex and $|\Phi_m\rangle$, $|\Psi_m\rangle$ are piecewise deterministic processes. Unlike usual unraveling where the processes evolve in time, here, the evolution is performed with respect to a formal iteration order $m = 0, 1, \ldots$ that corresponds to the m'th term in the sum of the magical formula. We introduced a propagator $T_{s,r} = r\mathcal{R}^{\mathrm{free}}_{s+r}\left(1 + \frac{\mathcal{L}^{\mathrm{coll}}}{r}\right)$, whose fundamental role is to evolve the triplets from m to $m+1$. We argued that a given s has to be associated with the truncation $M_{\mathrm{trunc}} \geq r/s$ to approximate the magical formula with

$$\mathcal{R}_s \approx \sum_{m=0}^{M_{\mathrm{trunc}}} [T_{r,s}]^m\, \mathcal{R}^{\mathrm{free}}_{s+r}. \tag{6.4}$$

From this approximation, we constructed the stochastic processes that eventually led to an estimation of the density matrix $\tilde{\rho}_s$. The evolution of the triplets was defined to alternate between continuous evolution according to the free contribution $r\mathcal{R}^{\mathrm{free}}_s$ and random jumps associated with $(1 + \mathcal{L}^{\mathrm{coll}}/r)$. We constructed those processes such that for a very large number of iterations, the application of the magical formula is reproduced and the density matrix is estimated by

$$\tilde{\rho}_s = s \sum_{m=0}^{\infty} \mathbb{E}\left[c_m |\Phi_m\rangle\langle\Psi_m|\right]. \tag{6.5}$$

When we considered reversible scenarios, a useful consequence of the alternate splitting between the continuous evolution and the random jumps is the generalization to the study of many-body Hamiltonian with the equivalent notation

$$H = H^{\mathrm{free}} + H^{\mathrm{int}}, \tag{6.6}$$

where the term free no longer refers to the kinetic contribution but to the exactly solvable part of the Hamiltonian with eigenbasis $\{|e_i\rangle\}_i$. This generalization allowed us to develop a stochastic unraveling based on a fixed-point iteration scheme associated to the expression

$$r\mathcal{R}^{\mathrm{free}}_r \left(1 + \frac{\mathcal{L}^{\mathrm{int}}}{r}\right) \rho_m = \rho_{m+1}. \tag{6.7}$$

To reproduce the ground state of H, we considered the evolution of the triplets $(c_m, |\Phi_m\rangle, |\Psi_m\rangle)$, where c_m is real and $|\Phi_m\rangle$, $|\Psi_m\rangle$ are piecewise deterministic processes. The density matrix is recovered as the statistical average

$$\rho_m = \mathbb{E}\left[c_m |\Phi_m\rangle\langle\Psi_m|\right], \tag{6.8}$$

where for $m \to \infty$, the ground state ρ_∞ is recovered with $\rho_m = \rho_{m+1} \approx \rho_\infty$.

The development of this fixed-point unraveling motivated the implementation of a numerical iterative algorithm to compute the unknown ground state of general Hamiltonians in many-body physics. We considered an ensemble of triplets

$\{(c_m^{(n)}, i_m^{(n)}, j_m^{(n)})\}_n$, $c^{(n)} \in \mathbb{R}$ that would undergo continuous free evolution interspersed with quantum jumps. We used the lighter notation $i \equiv |e_i\rangle$ for the vectors of the Hilbert space with $\{|e_i\rangle\}_i$ the eigenbasis of the free Hamiltonian. Due to the choice of the basis, it was discussed that the continuous evolution consists in simple weight updates mimicking the superoperator $r\mathcal{R}_r^{\text{free}}$ and leaving the vectors i, j unchanged. To have a controlled exploration of the Hilbert space, we proposed the random jumps associated with the superoperator $(1 + \mathcal{L}^{\text{int}}/r)$ to be selected stochastically, where a single jump between vectors of the eigenbasis is allowed.

With that algorithm, the density matrix at iteration m has been estimated with

$$\rho_m \approx \frac{\sum_n c_m^{(n)} |i_m^{(n)}\rangle\langle j_m^{(n)}|}{\sum_n c_m^{(n)} \delta_{i_m^{(n)}, j_m^{(n)}}}, \tag{6.9}$$

and ground-state properties via the usual quantum averages,

$$\langle A \rangle \approx \text{tr}(A\rho_{m^*}), \tag{6.10}$$

for a general operator A, where m^* is large enough such that the ensemble has reached the ground state.

This formulation allowed us to use of a powerful and intuitive importance sampling method by defining two weights associated with a single triplet: the ensemble weight w and the physical weight c. The ensemble weight reflects the statistical importance of the triplet for a given observable whereas the physical weights are used to perform the estimations as Eq. (6.10). The two weights are related by the relation $c = bw$ with $b > 0$. To concentrate the quantum jumps in the region that contributes the most to the averages, we defined the bias between the ensemble weight and the physical weight as

$$b = e^{\kappa n_{ij}^2}, \tag{6.11}$$

where κ is the analog to a classical spring constant and n_{ij} is the dynamic norm, i.e. the minimal number of transitions allowed by the Hamiltonian to go from i to j. To further control the number of triplets, we introduced an energy shift that is constantly updated during simulations. This reduced the growth of the size of the ensemble and stabilized the number of triplets to the desired level. The equivalent techniques found in the literature are all bounded by a maximal time step, however in our case, the freedom in the initial condition allows us to choose lower rates r (corresponding to larger time steps) which decreases the computational time required for a given statistical error. If the initial state is chosen closer to the ground state, the rate can be decreased, implying a quicker convergence and lower statistical errors. This feature makes our method very competitive due to its massive use of importance sampling and the absence of a clear upper bound on the evolution-step $1/r$. Additionally, it provides an efficient method to calculate initial conditions for field theoretical simulation exposed in Chap. 2.

We then developed an algorithm for reversible dynamics based on the unraveling presented in Chap. 3. The absence of dissipation allowed us to consider simplified models that however still reflected the major difficulties that will be encountered in more realistic and advanced simulations. This algorithm considers an ensemble of independent trajectories $\{(w_m^{(n)}, i_m^{(n)}, j_m^{(n)})\}_n$, where $w_m^{(n)}$ is the ensemble weight and $i_m^{(n)} \equiv |i_m^{(n)}\rangle$ are the eigenstates of the free Hamiltonian. The continuous deterministic part reproduces the superoperator $r\mathcal{R}_{s+r}^{\text{free}}$ and the random jumps $(1 + \mathcal{L}^{\text{int}}/r)$. Both contributions were implemented the same way as in the fixed-point iteration scheme.

We applied iteratively the main loop mimicking the application of the propagator on this ensemble of triplets. At iteration m, it allowed us to estimate the m^{th} summand in the magical formula with

$$\tilde{\rho}_{m,s} = s\mathbb{E}[c_m|\Phi_m\rangle\langle\Psi_m|] \approx s\sum_n b\ w_m^{(n)}|i_m^{(n)}\rangle\langle j_m^{(n)}| \tag{6.12}$$

and for a large number of iteration M_{trunc}, correlation functions in Laplace domain were obtained as

$$C_s^{AB} \approx \sum_{m=1}^{M_{\text{trunc}}} s\sum_n b\ w_m^{(n)}(AB)_{i_m^{(n)}j_m^{(n)}}, \tag{6.13}$$

with $(AB)_{i_m^{(n)}j_m^{(n)}} = \langle i_m^{(n)}|AB|j_m^{(n)}\rangle$. In addition to the same importance sampling, we introduced the deadweight approximation that allowed triplets to produce jumps only if their weight is above a critical value, the deadweight. To ensure an ergodic exploration of the Hilbert space through jumps, we proposed the rule that the inactive triplets however still evolve freely. It has been illustrated that the interplay between the importance sampling and the deadweight approximation is essential to overcome the dynamical sign problem. The latter manifests itself as divergences occurring at $t \sim 1$, however, the importance sampling and the deadweight approximations enabled us to study the long-time behavior of multi-dimensional reversible quantum systems. We emphasized that these investigations are usually out of reach due to the absence of an efficient formulation of tensor networks in more than one dimension and due to the sign problem inherent in almost every other stochastic method. Finally, we developed a simple procedure to invert the results in the Laplace domain to the time domain, which allowed us to extract dynamical properties such as frequencies of oscillations or damping parameters. Furthermore, it was shown that most of these dynamical properties could be obtained directly from the Laplace domain by educating ourselves to read a signal directly in the Laplace domain.

Given the success of the simulations for multi-dimensional reversible quantum dynamics, short-term perspectives include a more thorough analysis of the method's performances. As already pointed out in [53], the main restrictions are the strength of the interaction and the size of the Hilbert space. The algorithm is particularly efficient when $|H^{\text{free}}| > |H^{\text{int}}|$, where $|H|$ measure the typical strength of the Hamiltonian H. Hence, the choice of the free basis allows us to explore various regimes. The most pressing question concerns the quantum quenches and the crossing of a phase transition. The idea is to start from the ground state of a free Hamiltonian and quench it by enabling the interaction. Depending on the strength of the interaction, the new nonequilibrium steady state might cross a critical point. It is not clear how the localized excitations of the initial state propagate through the phase transition. On a numerical side, it would be interesting to test the ability of the importance sampling to sustain its efficiency through the delocalization of the phase transition. Besides the interaction strength, a major limitation is the size of the Hilbert space, which becomes important for multi-dimensional systems. We are however confident that properties of multi-dimensional systems can be computed on computational clusters without major difficulties.

For the first application to fundamental particles, we should consider the Schwinger model [125–127] to test the dissipation mechanism and understand its role in the simulations. The Schwinger model is a $(1+1)$-dimensional model of quantum electrodynamics (see App. C.3) displaying confinement effects. It could serve as a first encounter to renormalization [128] via the dissipative mechanism and as a test for

the efficiency of the method to describe confinement. Renormalization of the massless and massive models is discussed in [129, 130]. It is claimed in [129] that only the zero-point energy of the model does need to be renormalized, which is further supported by the perturbative approach of [131]. Therefore, we expect that the only possible divergent result within our approach is the computation of the ground state. Since there is an energy gap between the ground state and the first excited state which is composed of an electron-positron pair, we should be able to compute this gap and extract the mass of the pseudo-scalar pairs. We propose some concrete steps that could be followed. (i) Reproduce the ground state from the fixed point iteration scheme (see [132, 133] for the massless and massive cases). (ii) The energy of the first excited state can be computed also by using the fixed-point equation and App. A.3. The mass gap is simply obtained by subtracting the ground state energy. This approach avoids using the real-time dynamics and allows us to get some first results to compare to [132–134]. (iii) Alternatively, the chiral condensate $\langle\bar{\psi}\psi\rangle$ was used as a benchmark in early lattice computations [134–137].

Long-term perspectives include both studies of QED in lower dimensions and various effects in quantum chromodynamics. A benefit of the $(1+1)$QED theory is that electron-positron are confined. In particular, the mechanism of string breaking in $(1+1)$QED should give insights into the confinements of the quarks. It is usually referred to as a test concerning beyond-equilibrium results [114]. Independently, the theoretical foundations of a Hamiltonian approach to nonabelian gauge theories have recently been proposed in [37]. An application to $(2+1)$QCD could provide dynamical results for the quark-gluon plasma [41, 138]. Of course, the simulation of color confinement would be a major breakthrough for the future development of triplet unraveling for dissipative quantum field theory. We are confident that the issues addressed in this dissertation provide the necessary basis to perform such simulations while the structure of the method leaves room for massive algorithmic improvements. We hope that this document serves as an inspiration for exciting future developments.

A Generalities

A.1 Sign problem: divergent signal

A divergent signal often refers indirectly to the sign problem and the instabilities it involves. As an illustrative example, we consider the partition function $Z = \mathrm{tr}(e^{-\beta H})$ of a Hamiltonian H at the inverse temperature $\beta = 1/T$. This partition function is almost impossible to calculate exactly for large systems nonetheless, it can be estimated with the help of a classical Boltzmann weight summation $Z = \sum_c w_c$, where the sum $\sum_c$ runs over all possible configurations c. However, in quantum Monte Carlo simulations of fermionic systems, the Boltzmann weights w_c are not necessarily positive due to the inability to reproduce the quantum features. Because negative Boltzmann weights cannot be treated as probability, we interpret the absolute value of the weight $|w_c|$ as a probability of sampling. The expectation value of an observable O can be computed as follows

$$\begin{aligned} \langle O \rangle &\equiv \frac{\mathrm{tr}(Oe^{-\beta H})}{\mathrm{tr}(e^{-\beta H})} \\ &= \frac{\sum_c w_c O_c}{\sum_c w_c} = \frac{\sum_c \mathrm{sign}(w_c) O_c |w_c| / \sum_c |w_c|}{\sum_c \mathrm{sign}(w_c) |w_c| / \sum_c |w_c|} = \frac{\langle O \rangle_{|w|}}{\langle \mathrm{sign} \rangle_{|w|}}, \end{aligned} \tag{A.1}$$

where $O_c = \langle c|O|c\rangle$. Unfortunately, the contributions from the configurations with negative and positive signs nearly cancel with each other, such that the denominator $\langle \mathrm{sign} \rangle_{|w|}$ is exponentially small with increasing system size. In order to compensate for the exponential increase in statistical error when evaluating the observable $\langle O \rangle$, the required number of independent samples increases exponentially with the size of the system and the inverse temperature β.

A.2 Derivation of the magical formula

We derive in details the evolution superoperator in time $\mathcal{E}_t$ and in the Laplace domain $\mathcal{R}_s$. From the formal solution in time $\mathcal{E}_t = e^{\mathcal{L}t}$, we want to derive the tractable equations (2.31) and (2.36), respectively. The starting point is inspired from [50] and considers

$$\mathcal{E}_t = \mathcal{E}_t^{\mathrm{free}} e^{-rt} - \left[\mathcal{E}_{t-t'} \mathcal{E}_{t'}^{\mathrm{free}} e^{-rt'} \right]_0^t, \tag{A.2}$$

where we introduced an arbitrary rate $r > 0$. Using the relation

$$\frac{d}{dt} \mathcal{E}_t = \mathcal{L} \mathcal{E}_t, \tag{A.3}$$

and the commutation relation $[\mathcal{L}, \mathcal{E}_t] = 0$, we can right the above equations an integral over t'

$$\begin{aligned}\mathcal{E}_t &= \mathcal{E}_t^{\text{free}} e^{-rt} - \int_0^t dt' \frac{d}{dt'} \left(\mathcal{E}_{t-t'} \mathcal{E}_{t'}^{\text{free}} e^{-rt'} \right), \\ &= \mathcal{E}_t^{\text{free}} e^{-rt} - \int_0^t dt' \mathcal{E}_{t-t'} \left(-\mathcal{L} + \mathcal{L}^{\text{free}} - r \right) \mathcal{E}_{t'}^{\text{free}} e^{-rt'}, \\ &= \mathcal{E}_t^{\text{free}} e^{-rt} + \int_0^t dt' \mathcal{E}_{t-t'} \left(1 + \frac{\mathcal{L}^{\text{coll}}}{r} \right) \mathcal{E}_{t'}^{\text{free}} r e^{-rt'}, \end{aligned} \tag{A.4}$$

where we distributed the derivative in the first line. The last line reproduces the expression (2.31). To transform the nested expression as a product of superoperators, we consider the Laplace transform

$$\begin{aligned}\mathcal{R}_s &= \int_0^\infty dt e^{-st} \mathcal{E}_t, \\ &= \frac{1}{s - \mathcal{L}}. \end{aligned} \tag{A.5}$$

By taking the Laplace transform of Eq. (A.4) and using the appropriate substitution, we obtain

$$\begin{aligned}\mathcal{R}_s &= \mathcal{R}_{s+r}^{\text{free}} + \int_0^\infty dt' \int_0^\infty dt e^{-st} \mathcal{E}_t (r + \mathcal{L}^{\text{coll}}) \mathcal{E}_{t'}^{\text{free}} e^{-(s+r)t'}, \\ &= \mathcal{R}_{s+r}^{\text{free}} + \mathcal{R}_s (r + \mathcal{L}^{\text{coll}}) \mathcal{R}_{s+r}^{\text{free}}, \end{aligned} \tag{A.6}$$

We recast this expression as

$$\begin{aligned}\mathcal{R}_s &= \mathcal{R}_{s+r}^{\text{free}} \left[1 - (r + \mathcal{L}^{\text{coll}}) \mathcal{R}_{s+r}^{\text{free}} \right]^{-1}, \\ &= \mathcal{R}_{s+r}^{\text{free}} \sum_{m=0}^{\infty} \left[(r + \mathcal{L}^{\text{coll}}) \mathcal{R}_{s+r}^{\text{free}} \right]^m, \\ &= \sum_{m=0}^{\infty} \left[r \mathcal{R}_{s+r}^{\text{free}} (1 + \frac{\mathcal{L}^{\text{coll}}}{r}) \right]^m \mathcal{R}_{s+r}^{\text{free}}, \end{aligned} \tag{A.7}$$

where we used the Neumann series for a general operator T

$$(1 - T)^{-1} = \sum_{m=0}^{\infty} T^m. \tag{A.8}$$

A.3 COMPUTATION OF EXCITED STATES

We describe here a simple method to simultaneously extract the excited states $|E_i\rangle$, $i = 1, 2, \ldots$ from a general Hamiltonian H_0 for which the ground state $|E_0\rangle$ is known. This method has been used with full configuration quantum Monte Carlo in [139], and we follow the same procedure. To get the first excited state we propose to compute the eigenstate of the Hamiltonian $H_1 = P_0(H + E_0)P_0$ with the smallest eigenvalue, where the projector $P_0 = 1 - |E_0\rangle\langle E_0|$ and the ground state $|E_0\rangle$ are known prior to the simulations. The addition of the ground state energy in the definition of H_1 is to ensure that the first excited state has the smallest eigenvalue even if E_1 is positive

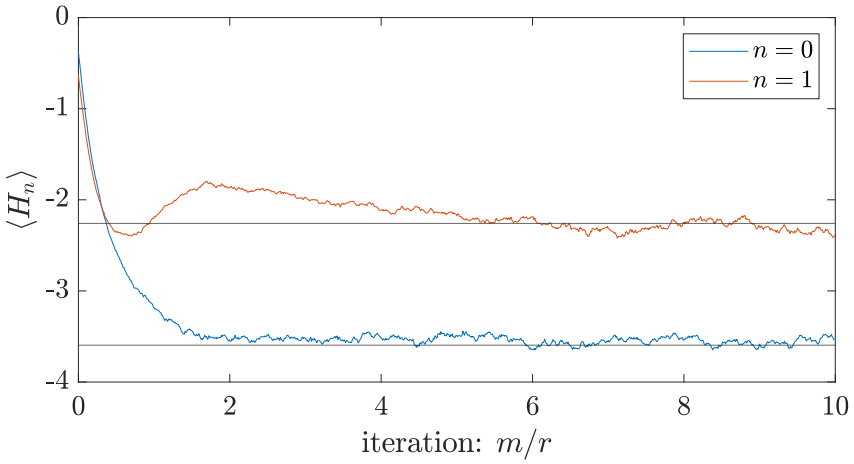

Figure A.1: Energy convergence for the ground state and the first excited state of a random 6×6 Hamiltonian using the fixed-point iterative scheme developed in Chap. 4. The solid black lines represent the exact corresponding eigenvalues.

and E_0 negative. After simplification the new Hamiltonian H_1 reads

$$H_1 = H_0 + E_0 \left(1 - 2|E_0\rangle\langle E_0|\right). \tag{A.9}$$

We can apply the projector P_n iteratively to obtain

$$H_n = H_{n-1} + E_{n-1}(1 - 2|E_{n-1}\rangle\langle E_{n-1}|), \tag{A.10}$$

where $|E_n\rangle$ is the ground state of the Hamiltonian H_n. The fixed-point iterative method described in Chap. 4 can then be used to compute the excited states. As long as the ground state of H_n is non-degenerate, it is possible to recover the eigenstates $|E_n\rangle$ as it is shown for a random 6×6 Hamiltonian in Figure A.1

B Laplace transform

B.1 The Zakian method

The Zakian method is a numerical method to perform an approximation of the inverse Laplace transform. This method is fast to implement and does not require heavy computational resources. The Laplace transform of a function $f(t)$ in the time domain is defined by

$$\tilde{f}(s) = \int_0^\infty e^{-st} f(t) dt. \tag{B.1}$$

Conversely, the formal inverse Laplace transform reads

$$f(t) = \frac{1}{2\pi i} \lim_{T\to\infty} \int_{c-iT}^{c+iT} \tilde{f}(s) e^{st} ds, \tag{B.2}$$

with $\mathrm{Re}(s) = c > c_0$ and where $\tilde{f}(s)$ has some singularities on the line $\mathrm{Re}(s) = c_0$. The Zakian method approximates the time domain function with

$$f(t) = \frac{2}{t} \sum_{i=1}^{n} \mathrm{Re}\left[K_i \tilde{f}\left(\frac{\alpha_i}{t}\right)\right], \tag{B.3}$$

where the constants α_i, K_i for $n = 5$ are given on Tab. B.1

Table B.1: Five constants α_i and K_i for the Zakian method.

i	α_i	K_i
1	$12.837677 + i1.666063$	$-36902.08 + i196990.1$
2	$12.226132 + i5.012719$	$+61277.03 - i95408.63$
3	$10.934303 + i8.409673$	$-28916.56 + i18169.19$
4	$8.7764347 + i11.92185$	$+4655.361 - i1.901529$
5	$5.2254533 + i15.72953$	$-118.7414 - i141.3037$

B.2 Dynamical properties in the Laplace domain

Generally, the motivation to introduce the Laplace transform stems from its ability to access large times properties by mitigating the small-to-medium-time effects. Naturally, the limit $s \to 0$ provides knowledge about the equilibrium properties of the system, which is extremely useful in open quantum systems driven towards such an equilibrium state. A signal in the Laplace domain over a certain range of s value can

however still provide estimations of dynamical properties before equilibrium. We want to show that it is not absolutely necessary to perform an inverse Laplace transform to obtain dynamical properties, such as frequencies or damping coefficients.

We consider a simplified version of typical signals encountered in realistic systems. These systems usually provide the following idealized signals in time

$$f_1(t) = a + b\cos(\omega_1 t), \tag{B.4}$$
$$f_2(t) = a + b\cos(\omega_1 t)\cos(\omega_2 t), \tag{B.5}$$
$$f_3(t) = a + b\cos(\omega_1 t)e^{-t/\tau}, \tag{B.6}$$

where $a,\ b$ are real constants, ω_1, ω_2 are frequencies, and $1/\tau$ is a damping parameter. The associated signals in the Laplace domain are multiplied by s to match the definition of the density matrix (2.38). Hence, we obtain the following signal in the Laplace domain plotted in the upper panel of Fig. B.1

$$s\tilde{f}_1(s) = \frac{s^2(a+b) + a\omega_1^2}{s^2 + \omega_1^2}, \tag{B.7}$$
$$s\tilde{f}_2(s) = \frac{s^4(a+b) + s^2(2a+b)(\omega_1^2+\omega_2^2) + a(\omega_1^2-\omega_2^2)^2}{s^4 + s^2 2(\omega_1^2+\omega_2^2) + (\omega_1^2-\omega_2^2)^2}, \tag{B.8}$$
$$s\tilde{f}_3(s) = \frac{s^2\tau^2(a+b) + s\tau(2a+b) + a(1+\tau^2\omega_1^2)}{s^2\tau^2 + 2s\tau + 1 + \tau^2\omega_1^2}. \tag{B.9}$$

The limits $s \to 0$ provide the averaged equilibrium value

$$\lim_{s\to 0} s\tilde{f}_i(s) = a, \tag{B.10}$$

$i = 1,\ 2,\ 3$ and the initial state is given by the case $s \to \infty$,

$$\lim_{s\to\infty} s\tilde{f}_i(s) = a + b. \tag{B.11}$$

Because it is difficult to differentiate between the curves in the Laplace domain, we have to consider the derivatives of the above quantities. The limits $s \to 0$ and $s \to \infty$ are particularly interesting. They scale as follows

$$\frac{d}{ds}\left(s\tilde{f}_1(s)\right) = \begin{cases} \frac{2b}{\omega_1^2}s & (s \ll 1), \\ \frac{2b\omega_1^2}{s^3} & (s \gg 1), \end{cases} \tag{B.12}$$
$$\frac{d}{ds}\left(s\tilde{f}_2(s)\right) = \begin{cases} \frac{2b(\omega_1^2+\omega_2^2)}{(\omega_1-\omega_2)^2(\omega_1+\omega_2)^2}s & (s \ll 1), \\ \frac{2b(\omega_1^2+\omega_2^2)}{s^3} & (s \gg 1), \end{cases} \tag{B.13}$$
$$\frac{d}{ds}\left(s\tilde{f}_3(s)\right) = \begin{cases} \frac{b\tau}{1+\tau^2\omega_1^2} & (s \ll 1), \\ \frac{b}{\tau s^2} & (s \gg 1), \end{cases} \tag{B.14}$$

with a remarkable maximum of the derivative for the first function at

$$s_1^* = \frac{\omega_1}{\sqrt{3}}. \tag{B.15}$$

Because each independent frequency contributes to an independent Lorenzian curve, the number of peaks in the derivatives in the Laplace domain counts the number of independent frequencies. This feature is illustrated in the lower panel of Fig. B.1. The $s \to 0$ limit of the derivative gives information about the damping since the latter

derivative converges to a constant for exponentially damped oscillations. In the same spirit, the s dependence in the limit $s \to \infty$ indicate if a damping occurs ($\propto s^{-2}$) or if the dynamics if purely reversible ($\propto s^{-3}$). The derivatives are hence sufficient to recover the dynamical parameters ω_1, ω_2, and τ and to differentiate between the various behaviors. Of course, it is an idealization of some more realistic signals, but these examples give a general idea of how to interpret a signal in the Laplace domain, and how it provides dynamical insights. It serves as proof that no information is lost in Laplace transform but rather displayed in another form.

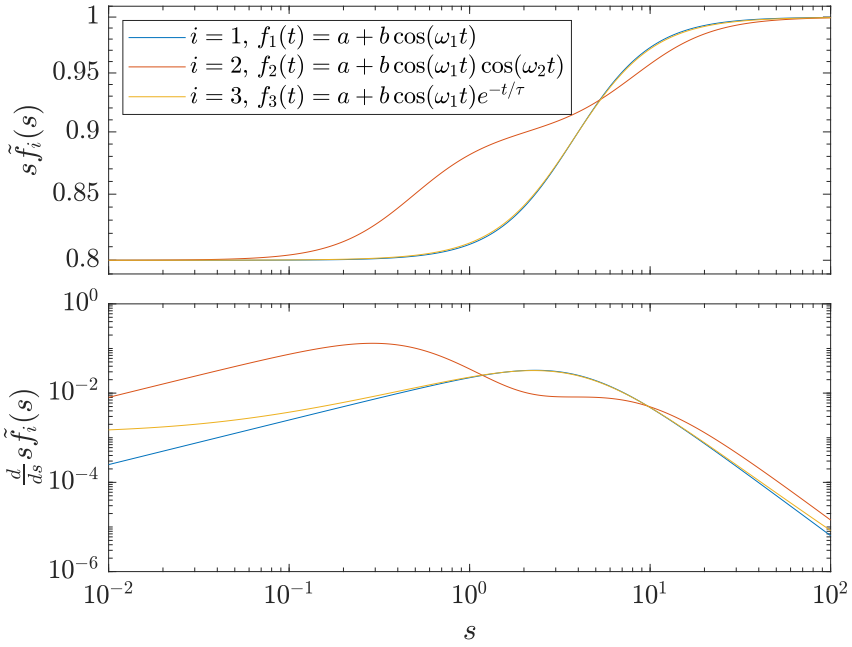

FIGURE B.1: Evolution in the Laplace domain of the functions $s\tilde{f}_1(s)$, $s\tilde{f}_2(s)$, $s\tilde{f}_3(s)$ and their respective first derivatives for the parameters $a = 0.8$, $b = 0.2$, $\omega_1 = 4$, $\omega_2 = 4.5$, and $\tau = 10$.

C Dissipative quantum field theory

C.1 Quartic interaction theory

A quartic interaction theory, or ϕ^4 theory, is a quantum field theory for self-interacting scalar fields with coupling constant λ commonly used as a toy model [18]. This archetype of fundamental particle theory is described in a Hamiltonian framework in d spatial dimensions with

$$H = H^{\text{free}} + \underbrace{\frac{\lambda}{24}\int_V \varphi_{\boldsymbol{x}}^4 d^d\boldsymbol{x}}_{H^{\text{coll}}}, \tag{C.1}$$

where H^{free} is the kinetic term and V is the volume of a d-dimensional hypercube that is eventually taken to $V \to \infty$. Using the momentum representation defined in (2.19) and the relativistic energy-momentum relation for a particle with mass m $\omega_k = \sqrt{m^2 + k^2}$, we can write the fields in the spatial domain as

$$\varphi_{\boldsymbol{x}} = \frac{1}{\sqrt{V}} \sum_{\boldsymbol{k}\in K^d} \frac{1}{\sqrt{2\omega_k}} \left(a_{\boldsymbol{k}}^\dagger + a_{-\boldsymbol{k}}\right) e^{-i\boldsymbol{k}\cdot\boldsymbol{x}}, \tag{C.2}$$

where the unusual $\frac{1}{\sqrt{2\omega_k}}$ factor is crucial for Lorentz invariance. With this representation of the field $\varphi_{\boldsymbol{x}}$, we can rewrite the collision Hamiltonian as

$$\begin{aligned} H^{\text{coll}} =& \frac{\lambda}{96}\frac{1}{V} \sum_{\boldsymbol{k}_1,\boldsymbol{k}_2,\boldsymbol{k}_3,\boldsymbol{k}_4\in K^d} \frac{\delta_{\boldsymbol{k}_1+\boldsymbol{k}_2+\boldsymbol{k}_3+\boldsymbol{k}_4,\boldsymbol{0}}}{\sqrt{\omega_{k_1}\omega_{k_2}\omega_{k_3}\omega_{k_4}}} \\ & \Big(a_{-\boldsymbol{k}_1}a_{-\boldsymbol{k}_2}a_{-\boldsymbol{k}_3}a_{-\boldsymbol{k}_4} + 4a_{\boldsymbol{k}_1}^\dagger a_{-\boldsymbol{k}_2}a_{-\boldsymbol{k}_3}a_{-\boldsymbol{k}_4} + 6a_{\boldsymbol{k}_1}^\dagger a_{\boldsymbol{k}_2}^\dagger a_{-\boldsymbol{k}_3}a_{-\boldsymbol{k}_4} \\ & + 4a_{\boldsymbol{k}_1}^\dagger a_{\boldsymbol{k}_2}^\dagger a_{\boldsymbol{k}_3}^\dagger a_{-\boldsymbol{k}_4} + a_{\boldsymbol{k}_1}^\dagger a_{\boldsymbol{k}_2}^\dagger a_{\boldsymbol{k}_3}^\dagger a_{\boldsymbol{k}_4}^\dagger\Big) \\ & + \frac{\lambda'}{4}\sum_{\boldsymbol{k}\in K^d}\frac{1}{\omega_k}\left(a_{\boldsymbol{k}}a_{-\boldsymbol{k}} + 2a_{\boldsymbol{k}}^\dagger a_{\boldsymbol{k}} + a_{\boldsymbol{k}}^\dagger a_{-\boldsymbol{k}}^\dagger\right) + \lambda'' V, \end{aligned} \tag{C.3}$$

where we have used normal ordering. The quantities λ' and λ'' have been redefined and we treat them as additional free interaction parameters to avoid divergences.

C.2 CONTINUOUS TREATMENT OF THE FREE DISSIPATION

We show an example of how to treat the free dissipation continuously in the case of a ϕ^4 theory. In general, we consider the evolution of Fock states having the form,

$$\begin{aligned}&|n_{\boldsymbol{k}_1},\dots,n_{\boldsymbol{k}_m}\rangle\langle n_{\boldsymbol{k}'_1},\dots,n_{\boldsymbol{k}'_{m'}}|\\&\quad=(a^\dagger_{\boldsymbol{k}_1})^{n_{\boldsymbol{k}_1}}\dots(a^\dagger_{\boldsymbol{k}_m})^{n_{\boldsymbol{k}_m}}|0\rangle\langle 0|(a_{\boldsymbol{k}'_1})^{n_{\boldsymbol{k}'_1}}\cdots(a_{\boldsymbol{k}'_{m'}})^{n_{\boldsymbol{k}'_{m'}}}.\end{aligned}\tag{C.4}$$

Hence, our goal is to find a closed form for the quantity

$$\mathcal{R}^{\text{free}}_{s+r}|n_{\boldsymbol{k}_1},\dots,n_{\boldsymbol{k}_m}\rangle\langle n_{\boldsymbol{k}'_1},\dots,n_{\boldsymbol{k}'_{m'}}|.\tag{C.5}$$

Taking a closer look at (2.28), we notice that the first dissipative terms produce a jump on both sides of the dyadic. To avoid superposition of states, we want to construct an expansion in γ_k which is justified by the limit of vanishing dissipation, and we neglect the terms linear in γ_k. With the formal solution

$$\mathcal{R}^{\text{free}}_s=\frac{1}{s-\mathcal{L}^{\text{free}}_0-\mathcal{L}^{\text{free}}_-},\tag{C.6}$$

where we used the notation

$$\begin{aligned}\mathcal{L}^{\text{free}}_0|\phi\rangle\langle\psi| &= -i[H^{\text{free}},|\phi\rangle\langle\psi|]-\sum_{\boldsymbol{k}\in K^d}\gamma_k\{a^\dagger_{\boldsymbol{k}}a_{\boldsymbol{k}},|\phi\rangle\langle\psi|\},\\ \mathcal{L}^{\text{free}}_-|\phi\rangle\langle\psi| &= \sum_{\boldsymbol{k}\in K^d}2\gamma_k a_{\boldsymbol{k}}|\phi\rangle\langle\psi|a^\dagger_{\boldsymbol{k}},\end{aligned}\tag{C.7}$$

we can write the following useful expansion

$$\mathcal{R}^{\text{free}}_s=\frac{1}{s-\mathcal{L}^{\text{free}}_0}+\frac{1}{s-\mathcal{L}^{\text{free}}_0}\mathcal{L}^{\text{free}}_-\frac{1}{s-\mathcal{L}^{\text{free}}_0}+\dots,\tag{C.8}$$

where the dots denote the terms with a higher power of $\mathcal{L}^{\text{free}}_-$. The latter notation stands for the fact that the Fock states will lose a particle on each side at every application of the superoperator, hence the $-$ sign. This splitting is motivated by the fact that we want to find a closed form for the application of the free evolution operator and to avoid unnecessary exploration of the Hilbert space. Because the operator $\mathcal{L}^{\text{free}}_-$ produces jumps along the diagonal, it creates a potentially dangerous additional exploration mechanism that should be avoided. Concerning the expansion (C.8), we expect the contributions from orders one and higher to be negligible since they are proportional to the friction parameter γ_k. Therefore, we can write the solution of (C.5) as

$$\begin{aligned}&\mathcal{R}^{\text{free}}_{s+r}|n_{\boldsymbol{k}_1},\dots,n_{\boldsymbol{k}_m}\rangle\langle n_{\boldsymbol{k}'_1},\dots,n_{\boldsymbol{k}'_{m'}}|\\&\quad=(s-\mathcal{L}^{\text{free}}_0)^{-1}|n_{\boldsymbol{k}_1},\dots,n_{\boldsymbol{k}_m}\rangle\langle n_{\boldsymbol{k}'_1},\dots,n_{\boldsymbol{k}'_{m'}}|+\mathcal{O}(\gamma_k),\\&\quad=\frac{|n_{\boldsymbol{k}_1},\dots,n_{\boldsymbol{k}_m}\rangle\langle n_{\boldsymbol{k}'_1},\dots,n_{\boldsymbol{k}'_{m'}}|}{s+r+i(\tilde\omega_{k_1}+\dots+\tilde\omega_{k_m}-\tilde\omega^*_{k'_1}-\dots-\tilde\omega^*_{k'_{m'}})},\end{aligned}\tag{C.9}$$

with $\tilde\omega_k=\omega_k-i\gamma_k$. This continuous treatment allows us to construct an unraveling for the linear quantum master equation (2.25). The unraveling aims at reproducing the solution of this equation by evolving an ensemble of coupled Fock states of the

form of (C.4), where the free evolution is solved according to the above procedure and the collisions correspond to transitions between Fock states. For instance, if the collision on the ket side removes two particles $a_{\boldsymbol{k}_l}$ and $a_{\boldsymbol{k}_{l'}}$

$$\begin{aligned}|n_{\boldsymbol{k}_1},\dots,n_{\boldsymbol{k}_l},\dots,n_{\boldsymbol{k}_{l'}},\dots,n_{\boldsymbol{k}_m}\rangle\langle n_{\boldsymbol{k}'_1},\dots,n_{\boldsymbol{k}'_{m'}}|\\ \mapsto c|n_{\boldsymbol{k}_1},\dots,n_{\boldsymbol{k}_l}-1,\dots,n_{\boldsymbol{k}_{l'}}-1,\dots,n_{\boldsymbol{k}_m}\rangle\langle n_{\boldsymbol{k}'_1},\dots,n_{\boldsymbol{k}'_{m'}}|,\end{aligned} \tag{C.10}$$

with $c\in\mathbb{C}$.

C.3 The Schwinger model

The Schwinger model is a $(1+1)$-dimensional model of quantum electrodynamics. In its original version [126] the fermions are massless. This simplification renders the model exactly solvable and the photons acquire a mass $m_\gamma = e_0/\sqrt{\pi}$ to preserve gauge invariance. The main consequence is that the spectrum of the Hamiltonian is composed of only free pseudo-scalar mesons of mass m_γ. The interpretation is that these mesons are composed of electron-positron pairs that are bound together via a confinement mechanism. Classically, it can be explained by the Coulomb potential between charged particles. In d spatial dimension it scales as r^{2-d}. Thus, in the Schwinger model, the force between the fermions is constant no matter how far they are separated. A natural generalization is to add a mass to the fermions, however, it renders the model no longer exactly solvable. The confinement mechanism survives and the mass of the electron-positron pairs changes (see [131] for a perturbation approach).

In one spatial dimension, fermions do not possess spin and photons have only two possible polarizations α, longitudinal or transversal. We introduce the creation and annihilation operators for photons a_q^α, $a_q^{\alpha\dagger}$, the electrons b_p, $b_p^\dagger$ and the positrons d_p, $d_p^\dagger$ together with the (anti-) commutation rules

$$[a_q^\alpha, a_{q'}^{\alpha'\dagger}] = \delta_{q,q'}\delta^{\alpha\alpha'},\quad \{b_p, b_{p'}^\dagger\} = \delta_{p,p'},\quad \{d_p, d_{p'}^\dagger\} = \delta_{p,p'}. \tag{C.11}$$

The general Hamiltonian for $(1+1)$ QED is given by

$$\begin{aligned}H =& H^{\mathrm{e/p}} + \underbrace{\sum_{q\in K_\times^1} |q| a_q^{\alpha\dagger} a_q^\alpha}_{H^{\mathrm{EM}}} + \underbrace{\sum_q \left(B_q^\dagger B_q + D_q^\dagger D_q\right)}_{H^{\mathrm{ghost}}}\\ &+ \underbrace{\sum_{q\in K_\times^1} :\left[J_q^0 A_{-q}^0 - J_q^1 A_{-q}^1\right]: + e'' V}_{H^{\mathrm{coll}}},\end{aligned} \tag{C.12}$$

where $H^{\mathrm{e/p}}$ is the Hamiltonian of the free fermions whose exact form depends on the mass of the fermions and H^{EM} is the free contribution of the electromagnetic field. The ghost term ensures a BRST invariance of the Hamiltonian [140]. The particles associated with the operators B_q and D_q do not interact with the fermions and the

bosons, hence the name ghost. The charged currents are given by

$$J_q^0 = -\frac{e_0}{\sqrt{L}} \sum_{p,p' \in K_\times^1} \Theta_{pp'} \Big[\delta_{p-p',q} \left(b_p^\dagger b_{p'} - d_{-p'}^\dagger d_{-p} \right) + \mathrm{sgn}(p) \delta_{p+p',q} \left(b_p^\dagger d_{p'}^\dagger - d_{-p} b_{-p'} \right) \Big], \tag{C.13}$$

$$J_q^1 = -\frac{e_0}{\sqrt{L}} \sum_{p,p' \in K_\times^1} \Theta_{pp'} \Big[\mathrm{sgn}(p) \delta_{p-p',q} \left(b_p^\dagger b_{p'} + d_{-p'}^\dagger d_{-p} \right) + \delta_{p+p',q} \left(b_p^\dagger d_{p'}^\dagger + d_{-p} b_{-p'} \right) \Big], \tag{C.14}$$

with $L = 2\pi/\Delta k$, where Δk is the lattice spacing in momentum space. The continuum limit is retrieved for $\Delta k \to 0$. The function Θ_k is the discretized Heaviside function, it vanishes if $k < 0$ and is equal to 1 if $k > 0$. The photonic gauge fields can be written in components as

$$A_{q0} = -A_q^0 = \frac{1}{\sqrt{2|q|}} (a_q^{0\dagger} - a_{-q}^0), \quad A_{q1} = A_q^1 = \frac{\mathrm{sgn}(q)}{\sqrt{2|q|}} (a_q^{1\dagger} - a_{-q}^1). \tag{C.15}$$

In the massless model, the full Hamiltonian is given by

$$H = \underbrace{\sum_{p \in K_\times^1} |p| \left(b_p^\dagger b_p + d_p^\dagger d_p \right)}_{H^{\mathrm{e/p}}} + \frac{1}{2} \sum_{q \in K_\times^1} m_\gamma^2 A_q^1 A_{-q}^1 + H^{\mathrm{EM}} + H^{\mathrm{BRST}} + H^{\mathrm{int}}, \tag{C.16}$$

where $m_\gamma = e_0/\sqrt{\pi}$ is added in order to ensure a BRST invariant theory. Conversely, in the massive case, the generalized Hamiltonian reads

$$H = \underbrace{\sum_{p \in K^1} E_p \left(b_p^\dagger b_p + d_p^\dagger d_p \right)}_{H_m^{\mathrm{e/p}}} + H^{\mathrm{EM}} + H^{\mathrm{BRST}} + H^{\mathrm{int}}, \tag{C.17}$$

where $E_p = \sqrt{p^2 + m_f^2}$, with m_f the mass of the fermion. With this small change, the model is no longer exactly solvable. Independently of the photon mass, we split the Hamiltonian according to the following free and collision terms

$$H^{\mathrm{free}} = H^{\mathrm{e/p}} + H^{\mathrm{EM}} + \frac{1}{2} m_\gamma^2 \sum_{q \in K_\times^1} \frac{1}{|q|} a_q^{1\dagger} a_q^1, \tag{C.18}$$

$$\begin{aligned} H^{\mathrm{int}} = & -\frac{e_0}{\sqrt{L}} \sum_{q,p,p' \in K_\times^1} \frac{\Theta_{pp'}}{\sqrt{2|q|}} \Big[\left(\delta_{p-p',q} \left(b_p^\dagger b_{p'} - d_{-p'}^\dagger d_{-p} \right) \right. \\ & \left. - \mathrm{sgn}(p) \delta_{p+p',q} \left(b_p^\dagger d_{p'}^\dagger - d_{-p} b_{-p'} \right) \right) \left(a_q^0 - a_{-q}^{0\,\dagger} \right) \\ & + \mathrm{sgn}(q) \left(\mathrm{sgn}(p) \delta_{p-p',q} \left(b_p^\dagger b_{p'} + d_{-p'}^\dagger d_{-p} \right) \right. \\ & \left. + \delta_{p+p',q} \left(b_p^\dagger d_{p'}^\dagger + d_{-p} b_{-p'} \right) \right) \left(a_q^1 - a_{-q}^{1\,\dagger} \right) \Big] \\ & - \frac{1}{4} m_\gamma^2 \sum_{q \in K^1} \frac{1}{|q|} \left(a_q^{1\dagger} a_{-q}^{1\,\dagger} + a_q^1 a_{-q}^1 \right), \end{aligned} \tag{C.19}$$

where the last line corresponds to the pure massive photon sector. Note that we dropped the BRST ghosts because, in practice, they do not participate in the interactions.

Bibliography

1. Foulkes, W. M. C., Mitas, L., Needs, R. J. & Rajagopal, G. Quantum Monte Carlo simulations of solids. *Reviews of Modern Physics* **73,** 33 (2001).
2. Carlson, J. *et al.* Quantum Monte Carlo methods for nuclear physics. *Reviews of Modern Physics* **87,** 1067 (2015).
3. Guther, K., Dobrautz, W., Gunnarsson, O. & Alavi, A. Time Propagation and Spectroscopy of Fermionic Systems Using a Stochastic Technique. *Physical Review Letters* **121,** 056401 (2018).
4. Werner, P., Oka, T. & Millis, A. J. Diagrammatic Monte Carlo simulation of nonequilibrium systems. *Physical Review B* **79,** 035320 (2009).
5. Muroya, S., Nakamura, A., Nonaka, C. & Takaishi, T. Lattice QCD at finite density: an introductory review. *Progress of Theoretical Physics* **110,** 615 (2003).
6. Beane, S., Detmold, W., Orginos, K. & Savage, M. Nuclear physics from lattice QCD. *Progress in Particle and Nuclear Physics* **66,** 1 (2011).
7. Fodor, Z. & Hoelbling, C. Light hadron masses from lattice QCD. *Reviews of Modern Physics* **84,** 449 (2012).
8. Heisenberg, W. Mehrkörperproblem und Resonanz in der Quantenmechanik. *Zeitschrift für Physik* **38,** 411 (1926).
9. Hubbard, J. Electron correlations in narrow energy bands. *Proceedings of the Royal Society A* **276,** 238 (1963).
10. Kretchmer, J. S. & Chan, G. K.-L. A real-time extension of density matrix embedding theory for non-equilibrium electron dynamics. *The Journal of Chemical Physics* **148,** 054108 (2018).
11. Lang, G. H., Johnson, C. W., Koonin, S. E. & Ormand, W. E. Monte Carlo evaluation of path integrals for the nuclear shell model. *Physical Review C* **48,** 1518 (1993).
12. White, S. R. *et al.* Numerical study of the two-dimensional Hubbard model. *Physical Review B* **40,** 506 (1989).
13. Schiró, M. & Fabrizio, M. Real-time diagrammatic Monte Carlo for nonequilibrium quantum transport. *Physical Review B* **79,** 153302 (2009).
14. Goth, F. & Assaad, F. F. Time and spatially resolved quench of the fermionic Hubbard model showing restricted equilibration. *Physical Review B* **85,** 085129 (2012).
15. Cohen, G., Gull, E., Reichman, D. R. & Millis, A. J. Taming the Dynamical Sign Problem in Real-Time Evolution of Quantum Many-Body Problems. *Physical Review Letters* **115,** 266802 (2015).

16. Mühlbacher, L. & Rabani, E. Real-Time Path Integral Approach to Nonequilibrium Many-Body Quantum Systems. *Physical Review Letters* **100,** 176403 (2008).

17. Wang, P., Cohen, G. & Xu, S. Numerical operator method for the real-time dynamics of strongly correlated quantum impurity systems far from equilibrium. *Physical Review B* **91,** 155148 (2015).

18. Peskin, M. E. & Schroeder, D. V. *An Introduction to Quantum Field Theory* (Addison-Wesley, Reading, USA, 1995).

19. Gross, D. J. & Wilczek, F. Ultraviolet Behavior of Non-Abelian Gauge Theories. *Phys. Rev. Lett.* **30,** 1343 (26 1973).

20. Politzer, H. D. Reliable Perturbative Results for Strong Interactions? *Phys. Rev. Lett.* **30,** 1346 (26 1973).

21. Wilson, K. G. Confinement of quarks. *Physical Review D* **10,** 2445 (1974).

22. Babich, R. *et al. Scaling Lattice QCD beyond 100 GPUs* in *Proceedings of 2011 International Conference for High Performance Computing, Networking, Storage and Analysis* (Association for Computing Machinery, New York, USA, 2011).

23. Boyle, P. A. The BlueGene/Q supercomputer. *Proceedings of Science* **Lattice 2012,** 020 (2012).

24. Vranas, P. QCD and the BlueGene. *Journal of Physics* **78,** 012080 (2007).

25. Amagasa, T. *et al.* Sharing lattice QCD data over a widely distributed file system. *Journal of Physics* **664,** 042058 (2015).

26. Frommer, A., Lippert, T., Medeke, B. & Schilling, K. *Numerical Challenges in Lattice Quantum Chromodynamics* (Springer Berlin, Heidelberg, Germany, 2000).

27. Wittig, H. *Particle Physics Reference Library: Volume 1: Theory and Experiments* (Springer International Publishing, Cham, Switzerland, 2020).

28. Korcyl, G. & Korcyl, P. Towards Lattice Quantum Chromodynamics on FPGA devices. *Computer Physics Communications* **249,** 107029 (2020).

29. Li, Z.-X. & Yao, H. Sign-problem-free fermionic quantum Monte Carlo: Developments and applications. *Annual Review of Condensed Matter Physics* **10,** 337 (2019).

30. Hangleiter, D., Roth, I., Nagaj, D. & Eisert, J. Easing the Monte Carlo sign problem. *Science Advances* **6,** eabb8341 (2020).

31. Chandrasekharan, S. Fermion bag approach to fermion sign problems. *The European Physical Journal A* **49,** 90 (2013).

32. Bloch, J., Bruckmann, F. & Wettig, T. Subset method for one-dimensional QCD. *Journal of High Energy Physics* **2013,** 140 (2013).

33. Berger, C. E. *et al.* Complex Langevin and other approaches to the sign problem in quantum many-body physics. *Physics Reports* **892,** 1 (2021).

34. Alexandru, A., Başar, G., Bedaque, P. F. & Warrington, N. C. Complex paths around the sign problem. *Reviews of Modern Physics* **94,** 015006 (2022).

35. Blunt, N. S., Rogers, T. W., Spencer, J. S. & Foulkes, W. M. C. Density-matrix quantum Monte Carlo method. *Physical Review B* **89,** 245124 (2014).

36. Öttinger, H. C. *A Philosophical Approach to Quantum Field Theory* (Cambridge University Press, Cambridge, England, 2018).
37. Öttinger, H. C. BRST quantization of Yang-Mills theory: A purely Hamiltonian approach on Fock space. *Physical Review D* **97,** 074006 (2018).
38. Oldofredi, A. & Öttinger, H. C. The dissipative approach to quantum field theory: conceptual foundations and ontological implications. *European Journal for Philosophy of Science* **11,** 18 (2021).
39. Taj, D. & Öttinger, H. C. Natural approach to quantum dissipation. *Physical Review A* **92,** 062128 (2015).
40. Ratti, C. Lattice QCD and heavy ion collisions: a review of recent progress. *Reports on Progress in Physics* **81,** 084301 (2018).
41. Guenther, J. N. Overview of the QCD phase diagram. *The European Physical Journal A* **57,** 136 (2021).
42. Breuer, H.-P. & Petruccione, F. *The Theory of Open Quantum Systems* (Oxford University Press, Oxford, England, 2007).
43. Rivas, A. & Huelga, S. F. *Open quantum systems* (Springer Berlin, Heidelberg, Germany, 2012).
44. Loh, E. Y. *et al.* Sign problem in the numerical simulation of many-electron systems. *Physical Review B* **41,** 9301 (1990).
45. Austin, B. M., Zubarev, D. Y. & Lester, W. A. Quantum Monte Carlo and Related Approaches. *Chemical Reviews* **112,** 263 (2012).
46. Booth, G. H., Grüneis, A., Kresse, G. & Alavi, A. Towards an exact description of electronic wavefunctions in real solids. *Nature* **493,** 365 (2012).
47. Troyer, M. & Wiese, U.-J. Computational Complexity and Fundamental Limitations to Fermionic Quantum Monte Carlo Simulations. *Physical Review Letters* **94,** 170201 (2005).
48. De Vega, I. & Alonso, D. Dynamics of non-Markovian open quantum systems. *Reviews of Modern Physics* **89,** 015001 (2017).
49. Öttinger, H. C. *Beyond equilibrium thermodynamics* (John Wiley & Sons, Hoboken, USA, 2005).
50. Schmidt, K. E., Niyaz, P., Vaught, A. & Lee, M. A. Green's function Monte Carlo method with exact imaginary-time propagation. *Physical Review E* **71,** 016707 (2005).
51. Breuer, H.-P. Genuine quantum trajectories for non-Markovian processes. *Physical Review A* **70,** 012106 (2004).
52. Breuer, H.-P., Kappler, B. & Petruccione, F. Stochastic wave-function method for non-Markovian quantum master equations. *Physical Review A* **59,** 1633 (1999).
53. Chessex, R., Borrelli, M. & Öttinger, H. C. Dynamical triplet unraveling: A quantum Monte Carlo algorithm for reversible dynamics. *Physical Review A* **106,** 022222 (2022).
54. Malone, F. D. *et al.* Accurate Exchange-Correlation Energies for the Warm Dense Electron Gas. *Physical Review Letters* **117,** 115701 (2016).
55. Malone, F. D. *et al.* Interaction picture density matrix quantum Monte Carlo. *The Journal of Chemical Physics* **143,** 044116 (2015).

56. Booth, G. H., Thom, A. J. W. & Alavi, A. Fermion Monte Carlo without fixed nodes: A game of life, death, and annihilation in Slater determinant space. *The Journal of Chemical Physics* **131,** 054106 (2009).

57. Cleland, D., Booth, G. H. & Alavi, A. Communications: Survival of the fittest: Accelerating convergence in full configuration-interaction quantum Monte Carlo. *The Journal of Chemical Physics* **132,** 041103 (2010).

58. Spencer, J. S., Blunt, N. S. & Foulkes, W. M. The sign problem and population dynamics in the full configuration interaction quantum Monte Carlo method. *The Journal of Chemical Physics* **136,** 054110 (2012).

59. Becca, F. & Sorella, S. *Quantum Monte Carlo Approaches for Correlated Systems* (Cambridge University Press, Cambridge, England, 2017).

60. Metropolis, N., Rosenbluth, A. W., Rosenbluth, M. N., Teller, A. H. & Teller, E. Equation of State Calculations by Fast Computing Machines. *The Journal of Chemical Physics* **21,** 1087 (1953).

61. Assaraf, R. & Caffarel, M. Zero-Variance Principle for Monte Carlo Algorithms. *Physical Review Letters* **94,** 170201 (2005).

62. Umrigar, C. J. Observations on variational and projector Monte Carlo methods. *The Journal of Chemical Physics* **143,** 164105 (2015).

63. Umrigar, C. J., Nightingale, M. P. & Runge, K. J. A diffusion Monte Carlo algorithm with very small time-step errors. *The Journal of Chemical Physics* **99,** 2865 (1993).

64. Metropolis, N. & Ulam, S. The Monte Carlo Method. *Journal of the American Statistical Association* **44,** 335 (1949).

65. Kalos, M. H. Monte Carlo Calculations of the Ground State of Three- and Four-Body Nuclei. *Physical Review* **128,** 1791 (1962).

66. Reynolds, P. J., Tobochnik, J. & Gould, H. Diffusion Quantum Monte Carlo. *Computers in Physics* **4,** 662 (1990).

67. Lee, M. A. & Schmidt, K. E. Green's Function Monte Carlo. *Computers in Physics* **6,** 192 (1992).

68. Reynolds, P. J., Ceperley, D. M., Alder, B. J. & Lester, W. A. Fixed-node quantum Monte Carlo for molecules. *The Journal of Chemical Physics* **77,** 5593 (1982).

69. Zen, A., Brandenburg, J. G., Michaelides, A. & Alfè, D. A new scheme for fixed node diffusion quantum Monte Carlo with pseudopotentials: Improving reproducibility and reducing the trial-wave-function bias. *The Journal of Chemical Physics* **151,** 134105 (2019).

70. Krauth, W. Quantum Monte Carlo Calculations for a Large Number of Bosons in a Harmonic Trap. *Physical Review Letters* **77,** 3695 (1996).

71. Wessel, S., Alet, F., Troyer, M. & Batrouni, G. G. Quantum Monte Carlo simulations of confined bosonic atoms in optical lattices. *Physical Review A* **70,** 053615 (2004).

72. Purwanto, W. & Zhang, S. Quantum Monte Carlo method for the ground state of many-boson systems. *Physical Review E* **70,** 056702 (2004).

73. Sandvik, A. W. Computational Studies of Quantum Spin Systems. *AIP Conference Proceedings* **1297,** 135 (2010).

74. Anderson, J. B. A random-walk simulation of the Schroedinger equation: H+3. *The Journal of Chemical Physics* **63,** 1499 (1975).
75. Sugiyama, G. & Koonin, S. Auxiliary field Monte-Carlo for quantum many-body ground states. *Annals of Physics* **168,** 1 (1986).
76. Al-Saidi, W. A., Zhang, S. & Krakauer, H. Auxiliary-field quantum Monte Carlo calculations of molecular systems with a Gaussian basis. *The Journal of Chemical Physics* **124,** 224101 (2006).
77. Feynman, R. P. Atomic Theory of the λ Transition in Helium. *Phys. Rev.* **91,** 1291 (1953).
78. Ceperley, D. M. Path integrals in the theory of condensed helium. *Reviews of Modern Physics* **67,** 279 (1995).
79. Yan, Y. & Blume, D. Path integral Monte Carlo ground state approach: formalism, implementation, and applications. *Journal of Physics B* **50,** 223001 (2017).
80. Lonardoni, D., Lovato, A., Gandolfi, S. & Pederiva, F. Hyperon Puzzle: Hints from Quantum Monte Carlo Calculations. *Phys. Rev. Lett.* **114,** 092301 (2015).
81. Nagy, A. & Savona, V. Driven-dissipative quantum Monte Carlo method for open quantum systems. *Physical Review A* **97,** 052129 (2018).
82. Korenblit, I. Y. & Shender, E. Ferromagnetism of disordered systems. *Soviet Physics Uspekhi* **21,** 832 (1978).
83. Sandvik, A. W. Evidence for Deconfined Quantum Criticality in a Two-Dimensional Heisenberg Model with Four-Spin Interactions. *Phys. Rev. Lett.* **98,** 227202 (2007).
84. Sachdev, S. Quantum magnetism and criticality. *Nature Physics* **4,** 173 (2008).
85. Emery, V. & Reiter, G. Mechanism for high-temperature superconductivity. *Physical Review B* **38,** 4547 (1988).
86. Arovas, D. P., Berg, E., Kivelson, S. A. & Raghu, S. The Hubbard Model. *Annual Review of Condensed Matter Physics* **13,** 238 (2022).
87. Pacheco, P. *An introduction to parallel programming* (Elsevier, 2011).
88. Chessex, R., Borrelli, M. & Öttinger, H. C. Fixed-point quantum Monte Carlo method: A combination of density-matrix quantum Monte Carlo method and stochastic unravellings. *Physical Review A* **105,** 062803 (2022).
89. Fano, G., Ortolani, F. & Parola, A. Hole-hole effective interaction in the two-dimensional Hubbard model. *Physical Review B* **42,** 6877 (1990).
90. Eisert, J., Friesdorf, M. & Gogolin, C. Quantum many-body systems out of equilibrium. *Nature Physics* **11,** 124 (2015).
91. Kormos, M., Collura, M., Takács, G. & Calabrese, P. Real-time confinement following a quantum quench to a non-integrable model. *Nature Physics* **13,** 246 (2017).
92. Bertini, B. *et al.* Finite-temperature transport in one-dimensional quantum lattice models. *Reviews of Modern Physics* **93,** 025003 (2021).
93. Hild, S. *et al.* Far-from-Equilibrium Spin Transport in Heisenberg Quantum Magnets. *Physical Review Letters* **113,** 147205 (2014).
94. Trotzky, S. *et al.* Probing the relaxation towards equilibrium in an isolated strongly correlated one-dimensional Bose gas. *Nature Physics* **8,** 325 (2012).

95. Bernier, J.-S., Poletti, D., Barmettler, P., Roux, G. & Kollath, C. Slow quench dynamics of Mott-insulating regions in a trapped Bose gas. *Physical Review A* **85,** 033641 (2012).

96. Schneider, U. *et al.* Fermionic transport and out-of-equilibrium dynamics in a homogeneous Hubbard model with ultracold atoms. *Nature Physics* **8,** 213 (2012).

97. Bloch, I., Dalibard, J. & Nascimbène, S. Quantum simulations with ultracold quantum gases. *Nature Physics* **8,** 267–276 (2012).

98. Gobert, D., Kollath, C., Schollwöck, U. & Schütz, G. Real-time dynamics in spin-$\frac{1}{2}$ chains with adaptive time-dependent density matrix renormalization group. *Physical Review E* **71,** 036102 (2005).

99. Sirker, J., Pereira, R. G. & Affleck, I. Diffusion and Ballistic Transport in One-Dimensional Quantum Systems. *Physical Review Letters* **103,** 216602 (2009).

100. Al-Hassanieh, K. A., Feiguin, A. E., Riera, J. A., Büsser, C. A. & Dagotto, E. Adaptive time-dependent density-matrix renormalization-group technique for calculating the conductance of strongly correlated nanostructures. *Physical Review B* **73,** 195304 (2006).

101. Aoki, H. *et al.* Nonequilibrium dynamical mean-field theory and its applications. *Reviews of Modern Physics* **86,** 779 (2014).

102. Nest, M., Klamroth, T. & Saalfrank, P. The multiconfiguration time-dependent Hartree–Fock method for quantum chemical calculations. *The Journal of Chemical Physics* **122,** 124102 (2005).

103. Jones, R. O. Density functional theory: Its origins, rise to prominence, and future. *Reviews of Modern Physics* **87,** 897 (2015).

104. Lacroix, D. & Ayik, S. Stochastic quantum dynamics beyond mean field. *The European Physical Journal A* **50,** 95 (2014).

105. Dong, Q. *et al.* Quantum Monte Carlo solution of the dynamical mean field equations in real time. *Physical Review B* **96,** 155126 (2017).

106. Mizuno, Y., Tsutsui, K., Tohyama, T. & Maekawa, S. Nonlinear optical response and spin-charge separation in one-dimensional Mott insulators. *Physical Review B* **62,** R4769 (2000).

107. Eckstein, M., Kollar, M. & Werner, P. Thermalization after an Interaction Quench in the Hubbard Model. *Phys. Rev. Lett.* **103,** 056403 (2009).

108. Eckstein, M. & Kollar, M. Nonthermal Steady States after an Interaction Quench in the Falicov-Kimball Model. *Physical Review Letters* **100,** 120404 (2008).

109. Eckstein, M. & Kollar, M. Near-adiabatic parameter changes in correlated systems: influence of the ramp protocol on the excitation energy. *New Journal of Physics* **12,** 055012 (2010).

110. McLachlan, A. D. & Ball, M. A. Time-dependent Hartree-Fock theory for molecules. *Reviews of Modern Physics* **36,** 844 (1964).

111. Gull, E., Reichman, D. R. & Millis, A. J. Numerically exact long-time behavior of nonequilibrium quantum impurity models. *Physical Review B* **84,** 085134 (2011).

112. Gliozzia, F. & Provero, P. The confining string and its breaking in QCD. *Nuclear Physics B* **556,** 76 (1999).

113. Verdel, R., Liu, F., Whitsitt, S., Gorshkov, A. V. & Heyl, M. Real-time dynamics of string breaking in quantum spin chains. *Physical Review B* **102,** 014308 (2020).

114. Hebenstreit, F., Berges, J. & Gelfand, D. Real-Time Dynamics of String Breaking. *Phys. Rev. Lett.* **111,** 201601 (2013).

115. Lüscher, M. & Weisz, P. Quark confinement and the bosonic string. *Journal of High Energy Physics* **2002,** 049 (2002).

116. Richter, J., Heitmann, T. & Steinigeweg, R. Quantum quench dynamics in the transverse-field Ising model: A numerical expansion in linked rectangular clusters. *SciPost Physics* **9,** 31 (2020).

117. Craig, I., Thompson, A. & Thompson, W. J. Practical numerical algorithms why Laplace transforms are difficult to invert numerically. *Computers in Physics* **8,** 648 (1994).

118. Epstein, C. L. & Schotland, J. The Bad Truth about Laplace's Transform. *SIAM Review* **50,** 504 (2008).

119. Davies, B. & Martin, B. Numerical inversion of the Laplace transform: a survey and comparison of methods. *Journal of Computational Physics* **33,** 1 (1979).

120. Hassanzadeh, H. & Pooladi-Darvish, M. Comparison of different numerical Laplace inversion methods for engineering applications. *Applied Mathematics and Computation* **189,** 1966 (2007).

121. Viti, J., Stéphan, J.-M., Dubail, J. & Haque, M. Inhomogeneous quenches in a free fermionic chain: Exact results. *EPL (Europhysics Letters)* **115,** 40011 (2016).

122. Mazza, P. P., Perfetto, G., Lerose, A., Collura, M. & Gambassi, A. Suppression of transport in nondisordered quantum spin chains due to confined excitations. *Physical Review B* **99,** 180302 (2019).

123. Öttinger, H. C. Composite higher derivative theory of gravity. *Physical Review Research* **2,** 013190 (2020).

124. Öttinger, H. C. A dynamically constrained Yang-Mills theory with Lorentz symmetry group as an alternative theory of gravity. arXiv: 2110.02527 (2021).

125. Abdalla, E., Abdalla, M. C. B. & Rothe, K. D. *Non-perturbative methods in 2 dimensional quantum field theory* (World Scientific, Singapore, 1991).

126. Schwinger, J. Gauge Invariance and Mass. II. *Physical Review* **128,** 2425 (1962).

127. Casher, A., Kogut, J. & Susskind, L. Vacuum polarization and the absence of free quarks. *Physical Review D* **10,** 732 (1974).

128. Wilson, K. G. & Kogut, J. B. The Renormalization Group and the Epsilon Expansion. *Physics Reports* **12,** 75 (1974).

129. Coleman, S. More About the Massive Schwinger Model. *Annals of Physics* **101,** 239 (1976).

130. Coleman, S., Jackiw, R. & Susskind, L. Charge Shielding and Quark Confinement in the Massive Schwinger Model. *Annals of Physics* **93,** 267 (1975).

131. Adam, C. Massive Schwinger Model within Mass Perturbation Theory. *Annals of Physics* **259,** 1 (1997).

132. Crewther, D. & Hamer, C. Eigenvalues for the massive Schwinger model from a finite-lattice Hamiltonian approach. *Nuclear Physics B* **170,** 353 (1980).

133. Bañuls, M. C., Cichy, K., Cirac, J. I. & Jansen, K. The mass spectrum of the Schwinger model with matrix product states. *Journal of High Energy Physics* **2013,** 158 (2013).

134. Carson, S. & Kenway, R. Numerical simulations of two-dimensional QED. *Annals of Physics* **166,** 364 (1986).

135. Zapp, K. & Orús, R. Tensor network simulation of QED on infinite lattices: Learning from $(1 + 1)$ d, and prospects for $(2 + 1)$ d. *Physical Review D* **95,** 114508 (2017).

136. Bañuls, M. C., Cichy, K., Jansen, K. & Saito, H. Chiral condensate in the Schwinger model with matrix product operators. *Physical Review D* **93,** 094512 (2016).

137. Papaefstathiou, I., Robaina, D., Cirac, J. I. & Bañuls, M. C. Density of states of the lattice Schwinger model. *Physical Review D* **104,** 014514 (2021).

138. Dong, X. & Greco, V. Heavy quark production and properties of Quark–Gluon Plasma. *Progress in Particle and Nuclear Physics* **104,** 97 (2019).

139. Blunt, N., Smart, S., Booth, G. & Alavi, A. An excited-state approach within full configuration interaction quantum Monte Carlo. *The Journal of Chemical Physics* **143,** 134117 (2015).

140. Nemeschansky, D., Preitschopf, C. & Weinstein, M. A BRST primer. *Annals of Physics* **183,** 226 (1988).